Title
Electromagnetic Characterizations of Mesh Deployable Ka Band Reflector Antennas for Emerging CubeSats

Author
Manohar, Vignesh

Publication Date
2016

University of California
Los Angeles

Electromagnetic Characterizations of Mesh Deployable Ka Band Reflector Antennas for Emerging CubeSats

A thesis submitted in partial satisfaction
of the requirements for the degree
Master of Science in Electrical Engineering

by

Vignesh Manohar

2016

Abstract of the Thesis

Electromagnetic Characterizations of Mesh Deployable Ka Band Reflector Antennas for Emerging CubeSats

by

Vignesh Manohar
Master of Science in Electrical Engineering
University of California, Los Angeles, 2016
Professor Yahya Rahmat-Samii, Chair

CubeSats are a miniaturized class of satellites that are launched as secondary payloads, offering the possibility of carrying out advanced space missions at affordable costs. Mechanical constraints and limited power onboard have limited current antenna implementations to low-gain, low data rate, and near-omnidirectional patterns. Integrating high gain aperture antennas with CubeSats can offer innumerable possibilities for advanced space missions. However, packaging large apertures into the small CubeSat form factor presents a formidable challenge to the scientific community. This thesis investigates the potential of integrating a 1m offset mesh deployable reflector antenna system with a 2.5U (10cm×10cm×25cm) CubeSat chassis for Ka band remote sensing or communications. Packaging such a large aperture into the small 2.5U volume necessitates a completely customized reflector design for our application. A detailed study of deployable umbrella mesh reflectors, RF analysis of various reflector antenna configurations and feed design methodologies are included in this work. These particular studies not only demonstrate the feasibility of the next high-gain antenna; they mark a major milestone (a 1m antenna size) for CubeSats, which is among the largest to be utilized for Ka band.

The thesis of Vignesh Manohar is approved.

Tatsuo Itoh

Benjamin Williams

Yahya Rahmat-Samii, Committee Chair

University of California, Los Angeles

2016

I dedicate this thesis to my grandparents, who continue to guide me from above.

Table of Contents

LIST OF FIGURES

List of Tables

ACKNOWLEDGMENTS

First and foremost, I express my heartfelt gratitude to my advisor Prof. Yahya Rahmat-Samii for his relentless efforts in guiding me through these two years. His excitement, dedication and passion continues to inspire my research. The research presented in this thesis is the result of an ongoing collaboration with Jet Propulsion Laboratory (JPL) and National Aeronautics and Space Administration (NASA) and I am grateful for their support. I thank my committee members, Prof. Tatsuo Itoh and Prof. Benjamin Williams for taking the time and effort to review this thesis and provide valuable insights. None of my work would have been possible without the unconditional support of my labmates, who have become my family here at UCLA. The work presented here is a byproduct of the countless fruitful discussions I have had with my labmates. I especially thank Dr. Joshua M. Kovitz for his continuous help throughout my time in the lab. I am grateful to my parents for their eternal love and support. Lastly, I thank all my friends and the administrative staff at UCLA, who formed the support system needed for my work.

CHAPTER 1

Introduction

For many years, smaller was not an option for the satellite industry. The stringent RF requirements required for high-performance satellites to deliver the desired quality-of-service (QoS) demands very heavy payloads. The typical timeframe for such conventional, large satellites is greater than 5 years, from proposal to launch with a cost ranging from $100M – $2B (in US dollars). This is expected, considering that fixed and broadcast satellite services operate at power levels near 10 kW with high gain antennas and very precise satellite pointing. While conventional satellite systems cannot be completely replaced by smaller satellites, the vision and needs for future space concepts are beginning to evolve. As small satellites become commonplace, many grand missions can be envisioned at fractional costs, and space becomes more accessible to the public.

The advent of digital signal processing technologies, very large scale integrated circuits, microelectromechanical systems (MEMS), and low-power programmable systems has decreased the size of electronics and their power consumption. As onboard electronics scaled to smaller dimensions, it became practical to shrink the satellite size by orders of magnitude. As one might expect, a smaller volume and weight leads to direct cost reductions in the satellite launch. There is a tradeoff between size and multifunctional capabilities that a satellite can offer, but this could be offset by launching a constellation of small satellites. These small satellites are often abbreviated as *SmallSats*.

The term SmallSats encompasses many different subclasses of small satellites, the most notable being the *CubeSat*. The game-changing thought behind the concept of the CubeSat,

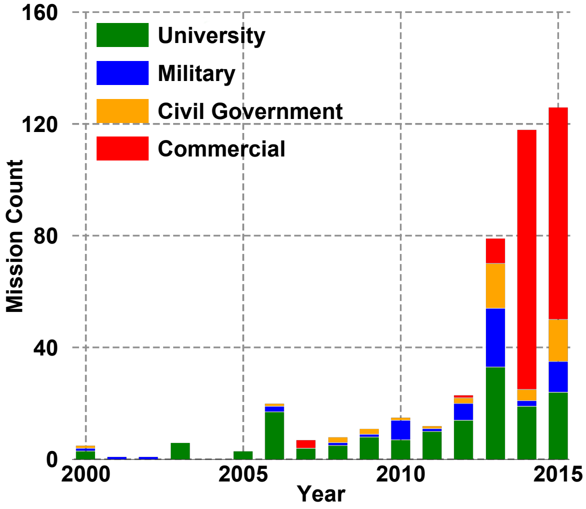

Figure 1.1: Chart showing the number of CubeSats missions (either already launched or with firm manifests) used for various applications as a function of year (adapted from [1]).

which is the focus of this thesis, was that designers could reduce the satellite volume to the size of a secondary payload on conventional launch vehicles. This reduces launch costs considerably, thus providing universities, small commercial companies, government organizations, and even hobbyists a reasonable access to space. Fig. 1.1 indicates that CubeSats have been gaining popularity considerably in the last 5 years. Even more interesting is that other sectors such as military, commercial, and government agencies are also excited about the possibilities with CubeSats, and recently these combined organizations have surpassed research and launches conducted at the university setting.

CubeSats' key contribution to promote widespread usage of miniaturized satellites is the establishment of a standard [2] to which developers can adhere. The standardization of size and weight also enabled the development of a universal launch system for CubeSats, called the Poly-Picosatellite Orbital Deployer (P-POD). This meant that researchers throughout the world could easily collaborate with each other to affordably participate in space missions through CubeSats. The P-POD launcher allows three 1U CubeSats to be launched simultaneously. This potentially led to development of a 3U standard for advanced applications. The dimensions of a 3U CubeSat is identical to that of 3 1U CubeSat placed on top of each

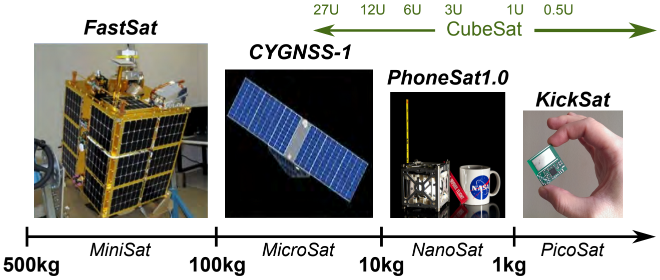

Figure 1.2: Illustration of the SmallSat family. Within this family, SmallSats can be classified by their mass as minisatellites, microsatellites, nanosatellites and picosatellites (adapted from [3]). CubeSats generally fall within the NanoSat and PicoSat classification.

other, resulting in a total volume of 3000 cm^3. Currently, standards such as 6U, 12U and 27U have begun to be explored. These potentially new satellite standards are also shown in Fig. 1.2, where we assume a mass of 1.33 kg per 1U volume. Representative examples of CubeSats that have been conceptualized is illustrated in Fig. 1.3.

1.1 Antennas for CubeSats: Current state of art

Antenna systems are a key part of any satellite system. The size and weight restrictions imposed by the CubeSat standard has instigated the scientific community to develop novel antenna designs to support CubeSats. Fig. 1.4 summarizes the major kinds of antenna systems that are currently under investigation for CubeSats. Currently, majority of the CubeSat missions are LEO based and operate in the UHF, VHF or S-band. At these frequencies, the most common choice for antennas are wire antennas and patch antennas.

Wire antennas involve dipoles, monopoles, Yagi Uda arrays and helical antennas. A considerable number of CubeSats that are currently in space use wire antennas for their simplicity. These antennas typically are placed on the external face of the CubeSat chasis and thus do not occupy any space inside the CubeSat. Wire antennas are especially common for HF, UHF and VHF applications. The omnidirectionality of dipoles make it a viable candidate for inter CubeSat communications. Reference [4] used an array of four dipoles at

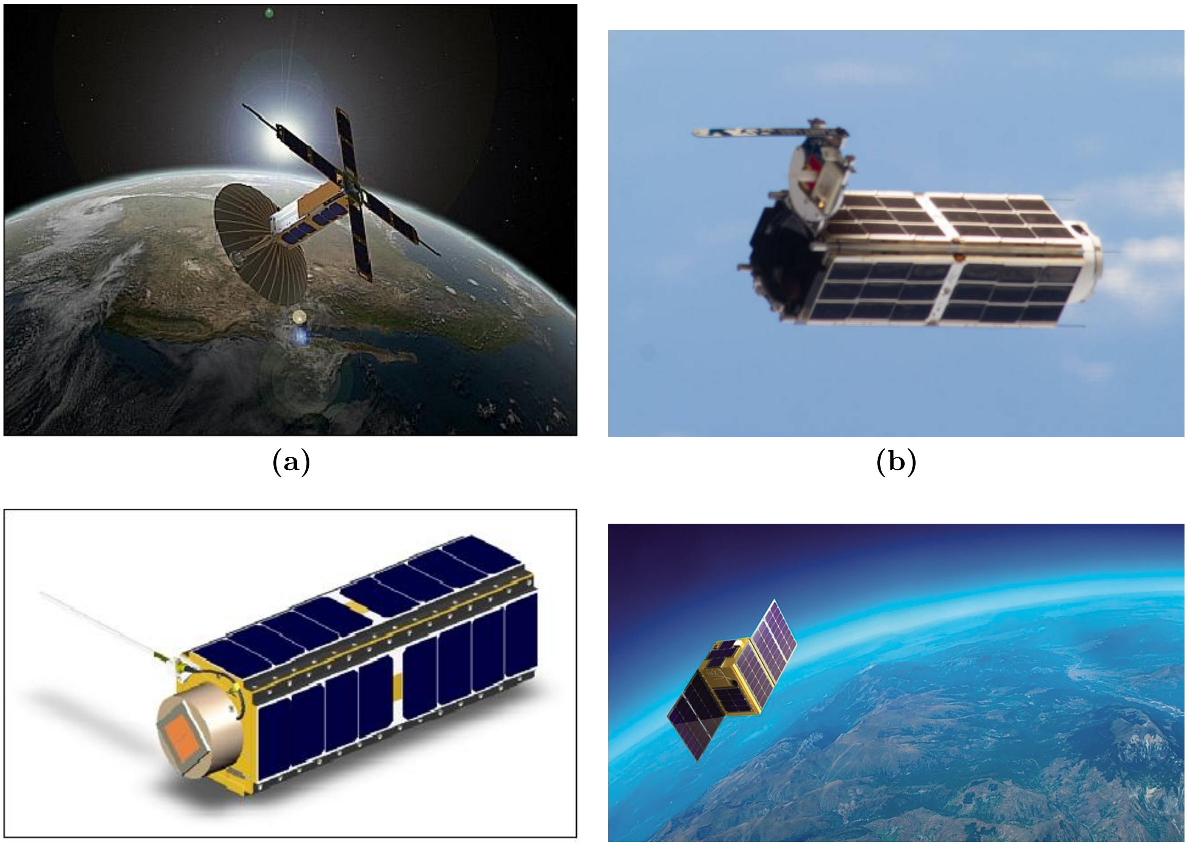

(a) (b)

(c) (d)

Figure 1.3: Representive examples of CubeSats that have either been launched or are under development. (a) AENEAS CubeSat (3U) developed by USC, (b) Dove CubeSat (3U) developed by PlanetLabs, (c) GeneSat CubeSat launched by NASA and (d) Hera CubeSat launched by Hera systems (California).

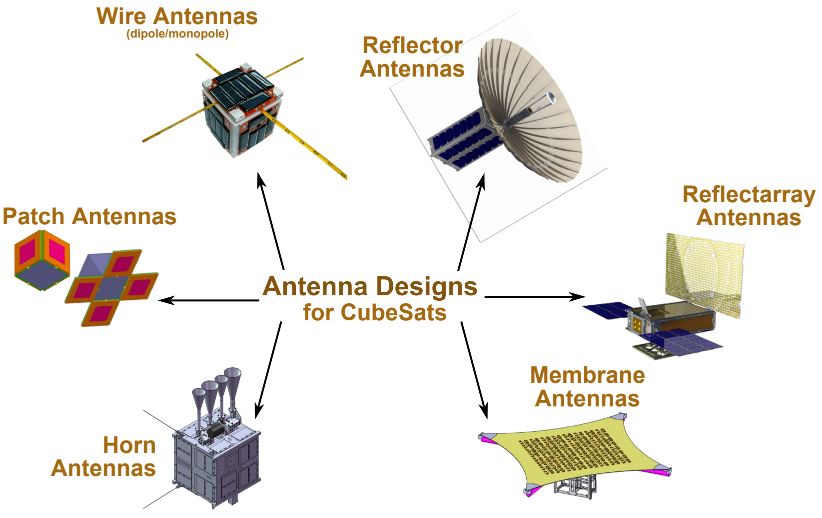

Figure 1.4: A graphical depiction of the many antenna types available to CubeSat designers.

VHF band for soil moisture sensing. Wire antennas have also been used for axis stabilization of CubeSat through the following works: (a) The 'HIT-SAT' CubeSat used dipole arrays for communication as well as spin stabilization by measuring fluctuation in received power in UHF/VHF band [5] and (b) the feasibility of the mechanical arrangement of dipoles itself being used for aerodynamic stabilization was explored in [6]. Dipoles and monopoles for communications are discussed in [7–9]. Reference [10] investigated the potential of using composite tape springs to fabricate dipoles and helical antennas for improved flexibility. A brief discussion on development of quadrifilar helix antenna is done in [11]. Studies comparing the performances of different kinds of wire antennas are done in [12–14].

Planar antennas like patch and slot antennas have gained special attention for CubeSats since it can easily be integrated into the CubeSat chasis, causing no additional space usage. An example of patch antennas seamlessly integrating with the CubeSat chasis can be seen in Fig. 1.7. A variety of patch antenna designs have been investigated at UHF, VHF and S-bands. Reference [16] surveys a variety of patch antenna designs for potential CubeSat

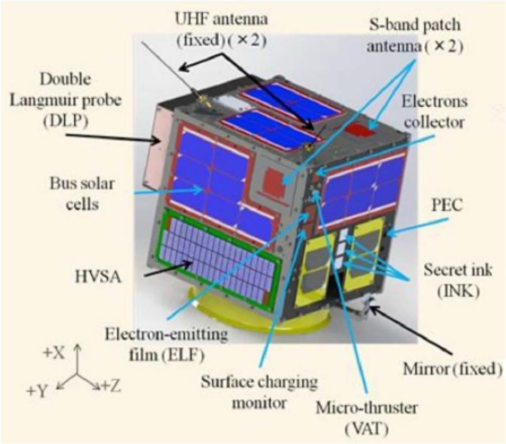

Figure 1.5: Dipole and patch antennas mounted on HORYU-1V CubeSat [15].

missions. Meshed and transparent patch antennas were investigated in [17]. An S-band patch antenna array for inter CubeSat communication was proposed in [18]. Planar Inverted F-Antenna (PIFA) arrays for CubeSats at S-band was proposed in [19] and [20]. Reference [21] discusses the development of a slot array that could be programmed to be multi-beam, omnidirectional or directive. Several other designs for patch and slot arrays for CubeSat can be found in [15, 22–44].

1.2 Reflector antennas for CubeSats: Past and future work

Reflector antenna design for advanced CubeSat applications have been gaining significant interest in the scientific community and will be the focus of this thesis. Reflector antennas offer the possibility of high gain and resolution, but with increased mechanical complexity. One of the first CubeSats to integrate a deployable reflector antenna system was the Aeneas mission [45]. Aeneas featured an S-band umbrella reflector antenna with 0.5m diameter designed for operation at 2.4 GHz. Reference [46] develops and comprehensively tests inflatable reflector antennas at S-band. A symmetric Cassegrain system was conceptualized in [47] for deep space exploration at Ka band. Ka band mesh surfaces for reflector antennas was revis-

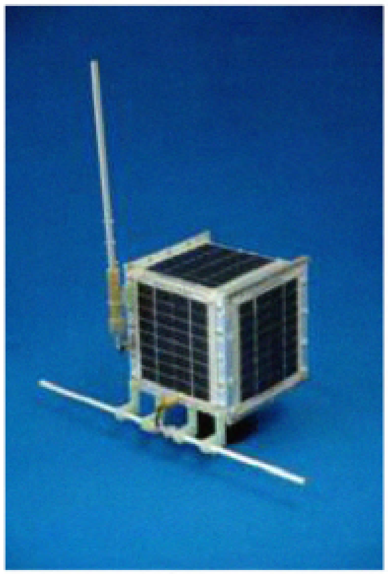

Figure 1.6: Dipole Antennas mounted on the HIT-SAT CubeSat [5].

ited in [48] for potential use in CubeSats. Solid deployable reflector antennas using graphite composite materials for Ku and Ka bands are discussed in [49]. A spinning offset reflector antenna system is being conceptualized in [50] for radiometry at 118.75 GHz. Reference [51] discusses the usage of doubly curved surfaces for improved scanning performance.

1.2.1 Focus of thesis

This thesis focuses on the characterization of a deployable reflector antenna system at Ka band for remote sensing using CubeSats. Recent investigations for remote sensing at Ka band [52] have suggested an aperture near 1 meter, and therefore a 1m aperture diameter was targeted for the next evolution of high-gain CubeSat reflector antennas. Packaging such a large aperture into a small 2.5U volume, coupled with mm-Wave frequency of operation necessitates an innovative approach to antenna engineering where the delicate balance between RF and mechanical aspects of the system must be closely studied. Though size and weight of the antenna system has always been an important consideration for satellite ap-

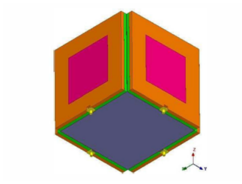

(a)

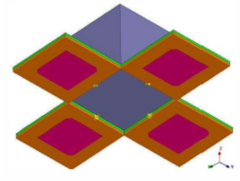

(b)

Figure 1.7: Integration of patch antenna with CubeSat chassis. (a) Folded and (b) deployed [31].

plications, the paradigm of miniaturized satellites take the mechanical constraints to a new level, since the size of these satellites are orders of magnitude less than their traditional counterpart. The challenges associated with this work is twofold: the mechanical constraints of the CubeSats lead to inevitable tradeoffs between RF and mechanical aspects of the system and the mm-Wave frequency operation pose significant challenges in simulation, fabrication and measurement of antennas. Achieving the desired RF performance at Ka band while satisfying packaging demands requires a combination of rigorous theoretical analysis, sophisticated CAD modeling and innovative measurement techniques. This work revisits mesh and umbrella reflector antenna with an intent to balance the tradeoffs between the mechanical and RF demands of the system. A combination of theoretical and full wave analysis is used to develop closed form expressions and equivalent models to aid performance estimation. A brief discussion on the initial feed design is presented and special attention is given to methods of increasing the overall efficiency of the reflector antenna system. Modeling of the interactions between the the reflector system and CubeSat chassis is an important aspect of system design. In this work, the capabilities of modern EM simulation tools to integrate with CAD softwares can are explored to simulate CAD models. As a representative example, a CAD reflector model is analyzed to provide insights into full wave CAD analysis.

Figure 1.8: S-band inflatable reflector antenna developed for 3U CubeSat [46]. The stowed volume of this antenna 0.2U.

1.3 Organization of work

A critical aspect of any system design is the analysis of potential sources of power loss to ensure that the design can meet the required specifications. With the wavelength being of the order of 1 cm at Ka band, slight deviations from ideal conditions can cause considerable amount of losses. Chapter 2 gives a detailed description of the various factors that contribute to losses in a reflector antenna system, and subsequent chapters discuss methodologies to evaluate some specific factors in detail. In particular, this thesis focuses on development of umbrella mesh reflector antennas for CubeSats at Ka band. Chapter 3 provides a detailed analysis of umbrella reflector antennas, followed by characterization of mesh surfaces for reflector antennas in chapter 4. Several reflector antenna configurations are studied in chapter 5 to evaluate their feasibility to be stowed into the CubeSat chasis. Based on the selection of a potential configuration, feed designs and reflector antenna simulations incorporating the designed feed will be highlighted in chapter 6. A brief analysis of a CAD reflector model will be presented in chapter 7. A flow chart representing various aspects of this thesis is shown in Fig. 1.10.

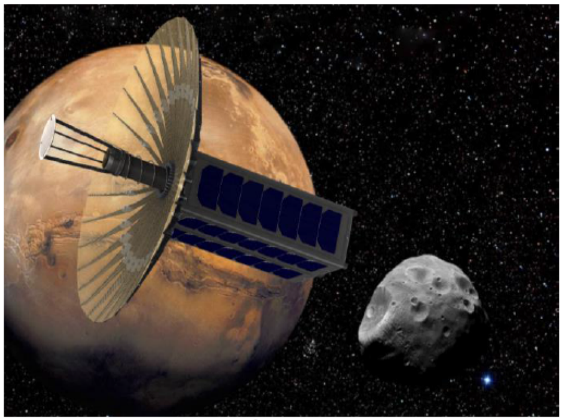

Figure 1.9: Cassegrain reflector antenna developed for 6U CubeSat for deep space missions [47].

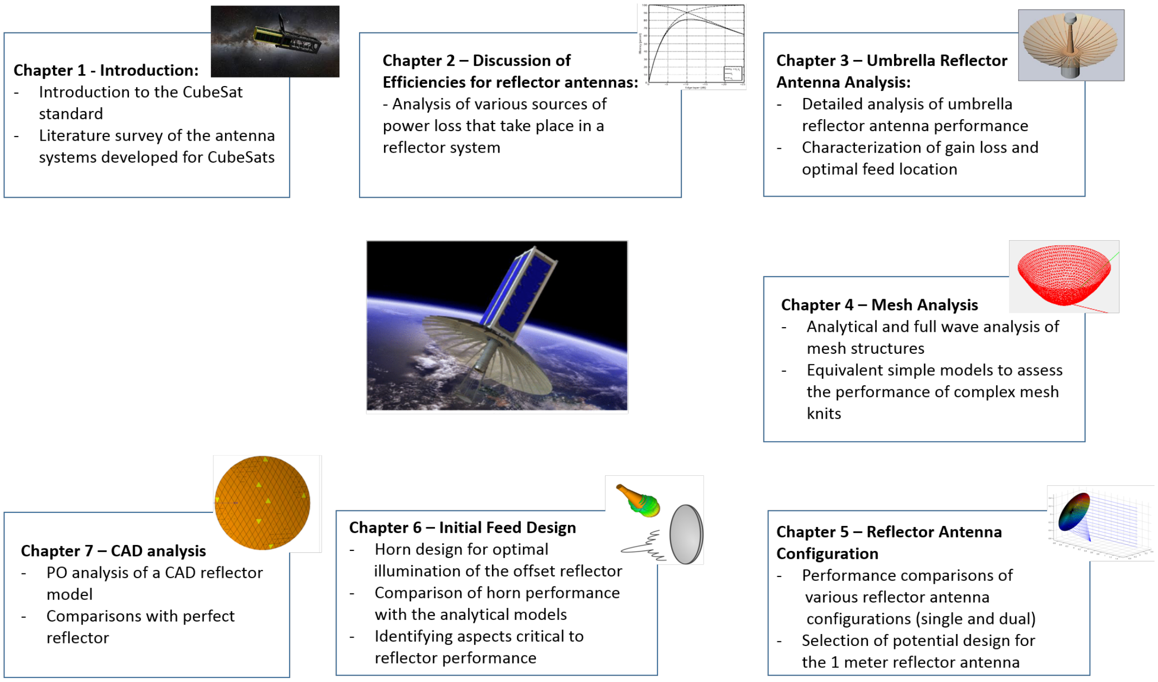

Figure 1.10: Flowchart illustrating the organization of the thesis.

CHAPTER 2

Efficiencies for a Reflector Antenna System

Loss characterization is one of the most important aspects of system design. Antennas play a pivotal role in remote sensing as well as establishing communication links between satellites and earth stations. The final aim for any transmitting antenna system is to provide an optimum Signal to Noise Ratio (SNR) at the receiver (for communication links) or ensure that the received signal after scattering from the target has a good SNR (for remote sensing). This directly translates to certain gain requirements that must be satisfied by the antenna system. Other factors that can be critical, especially for remote sensing, is the spatial resolution (beamwidths) and cross polarization.

One of the primary factors that tend to limit advanced space missions using CubeSats is its limited power handling capability. For Ka band applications, which is the focus of this work, the losses can be significant for slight deviations from ideal conditions. This necessitates revisiting the various loss factors to gain an in-depth understanding of the tradeoffs that must be accounted for while designing the reflector antenna system

2.1 A discussion on efficiencies

For an aperture antenna, the maximum directivity that can be achieved is given as:

$$D = 4\pi \frac{A_p}{\lambda^2} \tag{2.1}$$

Where A_p represents the physical area of the aperture and λ represents the wavelength.

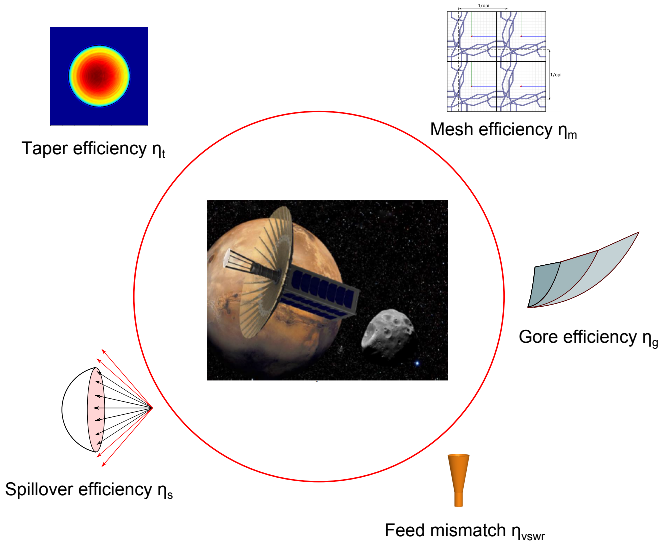

Figure 2.1: Efficiencies that are considered in detail in this work.

However, in practice, it is impossible to achieve this maximum directivity due to various losses that take place in the system. In order to accurately relate the radiated power to the input power, these loss factors must be multiplied to the theoretical maximum directivity to get an estimate of the gain of the antenna system. The gain of the aperture antenna can then be defined as:

$$G = \eta \left[4\pi \frac{A_p}{\lambda^2} \right] \tag{2.2}$$

where η represents the overall efficiency of the reflector antenna system and by itself is a product of many sub-efficiencies as represented in Table 2.1. It is important to thoroughly characterize each one of these efficiencies to get an optimum design. These efficiencies also play a major role in deciding the mechanical tolerance for reflector antenna design. At Ka band, with the wavelength being of the order of 1cm, even an RMS surface error or a positioning error of 0.1cm can lead to significant losses.

The efficiencies that play a dominant role in determining the performance of a mesh deployable reflector antenna system are outlined in Fig. 2.1 and will be the focus of this work. The subsequent section gives a brief description of these efficiencies.

Table 2.1: List of efficiencies that should be characterized while designing a reflector antenna system.

Symbol	**Definition**
e	Radiation efficiency due to ohmic loss, which is usually very small, except for lossy devices included as part of feed system. The typical value for e=0.99
η_t	Taper efficiency due to gain loss based on an aperture taper distribution
η_s	Spillover (or feed) efficiency due to that portion of the feed radiation which is not intercepted by the reflector
η_b	Backlobe efficiency of the feed pattern not included in η_s (to be used only if not included in η_s)
η_p	Depolarization efficiency due to the power generated in the polarization state orthogonal to that which is desired. It typically takes values greater than 0.98
η_{sq}	Squint efficiency due to the lateral displacement of the feed for the circularly polarized beam. If the beam shifts off axis by one half power beamwidth, $\eta_{sq} = 0.98$
η_{rms}	Surface RMS efficiency due to the mesh surface RMS distortion including pillowing effect
η_g	Gore efficiency due to gore flatness which is a function of the number of gores, F/D, etc.
η_{tr}	Surface truncation efficiency due to the boundary
η_m	Surface leakage due to mesh type surface. It is typically 0.98 for a mesh several grid lines per wavelength
η_{sc}	Scan efficiency due to the feed displacement from the optimal position
η_{vswr}	Feed mismatch efficiency which, for a VSWR of 1.2:1 is $\eta_{vswr} = 0.99$
η_{st}	Strut blockage efficiency due to presence of struts
η_{bl}	Aperture blockage efficiency due to the presence of the feed system or subreflector
η_{um}	Unmodeled efficiency due to the other unaccounted loss mechanisms. A typical value may be $\eta_{um} = 0.98$
η	Total efficiency of the system (computed as the product of all efficiencies)

2.2 Aperture efficiency: spillover and taper

Aperture efficiency is an efficiency which is inherent to the reflector antenna. Ideally, one would want the feed to illuminate the entire aperture of the antenna and have zero fields radiated in regions outside the aperture. However, such an abrupt transition can never be achieved in practice. The fields radiated by the feed will always have some power that ‘spills over’. The greater uniformity we desire in the aperture illumination, the greater will be the spillover from the feed. Immediately, a tradeoff can be seen: The gain will increase by illuminating the aperture uniformly, but will decrease due to the power that is lost due to the

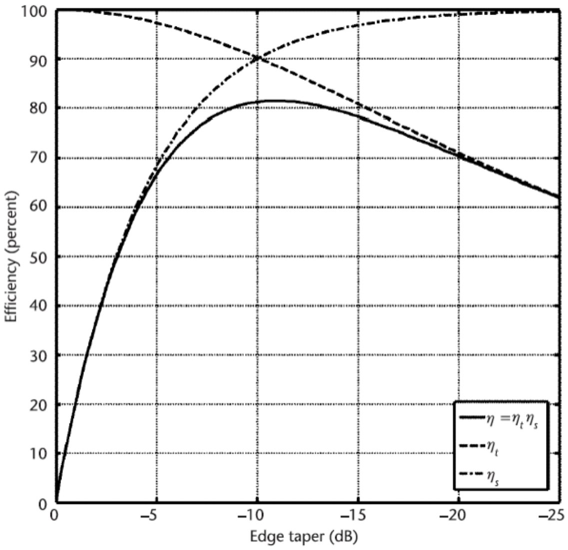

Figure 2.2: Aperture efficiency for a parabolic reflector antenna. Note the tradeoff between taper and spillover efficiency [53].

spillover. This trend can easily be observed in Fig. 2.2. It is seen that the optimal efficiency can be achieved if the amplitude distribution in the aperture of the reflector is given a taper of 10 dB, meaning that the strength of the field at the edge of the aperture is 10 dB below its value at the center. Referring to Table 2.1, the aperture efficiency can be expressed as:

$$\eta_a = \eta_s \eta_t \tag{2.3}$$

An amplitude taper of 10dB leads to an aperture efficiency of about 80%, which is the theoretical maximum aperture efficiency one can get from conventional parabolic reflector antennas.

The aperture efficiency is of particular importance when designing the horn feed for the reflector antenna. The horn must be optimized to provide the required taper and cause minimum spillover. A detailed discussion of horns and affects of the feed pattern on reflector performance will be done in chapter 6.

2.3 Efficiency for umbrella reflector antennas

Many deployable reflector antennas use a special type of reflector surface called 'umbrella reflector'. The surface of such a reflector antenna is formed by a discrete set of parabolic ribs, connected by flat surfaces called gores. The two major factors that contribute to the gain loss in an umbrella reflector antenna are:

1. The umbrella reflector surface deviates from the ideal paraboloid surface resulting in gain loss due to phase aberrations at the aperture. This is denoted in Table 2.1 by η_g, that represents loss due to the 'flatness' of the gore.

2. The aperture of the umbrella is a polygon, whose number of sides equals the number of ribs. This leads to its aperture area being lesser than that of the aperture area of an ideal paraboloid, causing loss in gain. This is represented in Table 2.1 by η_{tr}, that represents the truncation efficiency due to the boundary.

The total efficiency of umbrella reflectors can be expressed as:

$$\eta_{um} = \eta_g \eta_{tr} \tag{2.4}$$

2.4 Efficiency for mesh reflector antennas

In order to reduce weight, mesh reflector antennas are often used for space applications. When electromagnetic waves are incident on the mesh, only a fraction of it gets reflected back. A portion of it gets transmitted through the mesh openings. In general, there can also ohmic loss in the wires of the mesh. This is denoted in Table 2.1 by η_m. The characterization of mesh efficiency will be discussed in detail in chapter 4. Further, the mesh surfaces typically consists of interwoven wires and can cause RMS surface error. This is captured by the η_{rms} in Table 2.1.

2.5 Feed positioning and efficiency

The feed is an important aspect of the reflector antenna system. It must be designed appropriately to ensure proper illumination of the reflector surface. To utilize power effectively, it is important that the VSWR at the input of the feed system is minimum. The power lost due to impedance mismatch at the input of the reflector system is captured by η_{vswr} in Table 2.1. The position of the feed is a critical parameter for constant phase at the aperture. Any displacement of the feed from the focal point can lead to the beam squints, which is captured by η_{sq}.

2.6 Blockages

Blockage is an important consideration for symmetric configurations. In general, the feed and subreflector lies directly in the path of the rays that reflect off the main reflector surface. These cause phase aberrations in the aperture and reduce the gain of the reflector system. This is modeled by the term η_{bl} in Table 2.1. In reflector systems, struts are commonly used to hold the subreflector and the feed in place. These cause additional phase aberrations and must be accounted for. This efficiency is denoted as η_{st}.

CHAPTER 3

Characterization of Umbrella Reflector Antennas: Analysis of Gain Loss and Estimation of Optimal Feed Point

Most deployable reflector systems use a special class of reflector surface called ‘umbrella reflector’. A representative example where an umbrella type reflector surface was previously used for CubeSats is shown in Fig. 3.1. The umbrella reflector surface consists of a discrete number of parabolic ribs that are connected by surfaces called gores. Each gore surface is a section of a parabolic cylinder, bound between two parabolic ribs. In deployable reflector antenna systems, the gore surface can be formed by stretching a mesh between the two ribs. The gores cause the surface of reflector to deviate from a true paraboloid, resulting in ambiguity of optimal feed position. In the case of dual reflector systems, as shown in Fig. 3.1, the subreflector must be optimally positioned to account for the gores. The size and weight constraints imposed by CubeSat standards makes smaller number of gores attractive for CubeSat applications. Significant amount of work has been done in the past to characterize umbrella reflectors with larger amount of gores. This chapter revisits the determination of the optimum feed location and gain loss with an emphasis on a smaller number of gores. The underlying assumptions and analysis of previous approaches are reviewed. Furthermore, comparison with results from manually tuning using Physical Optics (PO)-based diffraction analysis is presented. These results pinpoint the cases in which the previous approximations are no longer valid, necessitating a manual tuning of the feed location for optimal gain. The

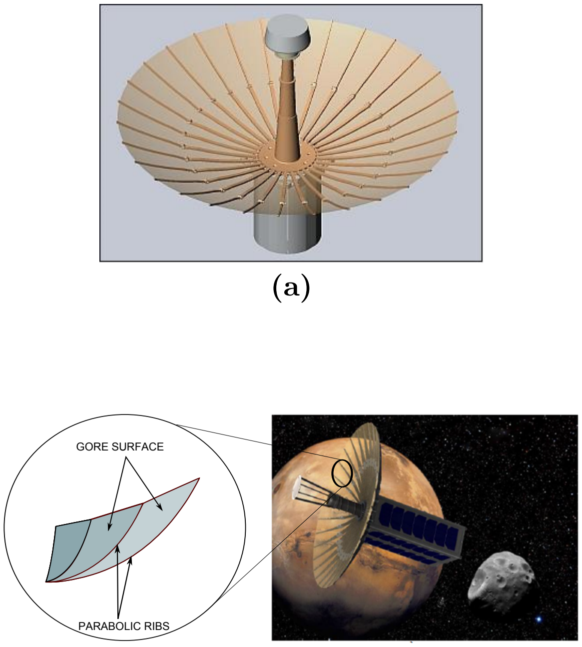

(a)

(b)

Figure 3.1: A representative example of umbrella reflector antenna that was used for previous CubeSat applications [45]. (a) The the umbrella reflector model. (b) Illustraion of the reflector being deployed in space.

effects of feed taper is also discussed, further extending previous works position.

3.1 Mathematical representation of the gore surface

Assuming that there are N_g gores, with the focal length of each rib being F_r, the gore surface can be defined through two parameters A and t as:

$$x = t[cos\phi_m + A(cos\phi_{m+1} - cos\phi_m)] \tag{3.1}$$

$$y = t[sin\phi_m + A(sin\phi_{m+1} - sin\phi_m)] \tag{3.2}$$

$$z = t^2/4F_r \tag{3.3}$$

where, $0 \leq A \leq 1$, $0 \leq t \leq D/2$, $\phi_m = 2\pi(m-1)/N_g$ and $m = 1, 2, .., N_g$. This parameterization is shown in Fig. 3.2a. The three dimensional representation of the reflector surface is illustrated in Fig. 3.2b.

These equations be converted into a single equation of the form of $z = f(x, y)$ as

$$z_g = \frac{\rho^2}{4F_g(\phi)} \tag{3.4}$$

where

$$F_g(\phi) = \frac{F_r cos^2(\pi/N_g)}{cos^2 \frac{\phi_m + \phi_{m+1} - 2\phi}{2}} \tag{3.5}$$

$$\rho^2 = x^2 + y^2 \tag{3.6}$$

$$\phi = \tan^{-1}(y/x) \tag{3.7}$$

It can be seen from (3.4) and (3.5) that the focal length of the umbrella reflector is now a function of ϕ. The variation of F_g with ϕ is plotted in Fig. 3.3. An interesting interpretation of (3.4) and (3.5) is that the umbrella reflector can be viewed as a family of parabolic curves, each having a focal length between $F_r \cos^2(\pi/N_g)$ and F_r. Note the periodic variation of F_g. This periodicity manifests itself in aperture distributions as cyclical phase variations. As the number of gores increase, the deviation of F_g from F_r begins to decrease. It is evident that there is no distinct focal point for the umbrella reflector and thus, the position of the feed is not obvious.

3.2 Finding the optimum feed location

In this section, we revisit the problem of finding the optimal feed position for umbrella reflectors with particular consideration for a low number of gores. Two approaches reported

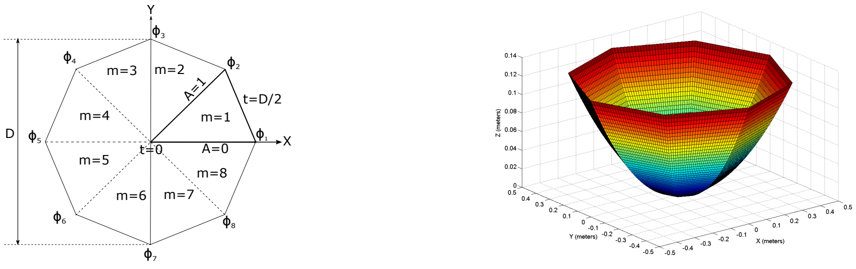

(a) **(b)**

Figure 3.2: Mathematical representation of umbrella reflector surface with $N_g = 8$. (a) Parameterization in XY plane. (b) Actual 3D representation of the reflector surface.

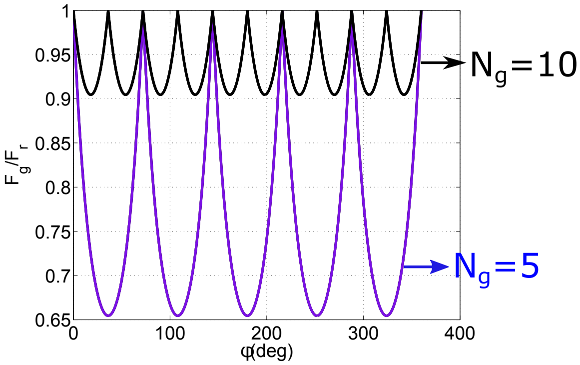

Figure 3.3: Variation of F_g as a function of ϕ for N_g=5 and 10. Note the periodic nature of F_g as a function of ϕ. This periodicity results in cyclical variations in the phase at the reflector aperture causing the ambiguity in the optimum feed point.

in the literature include: (a) a Physical Optics (PO) approach combined with the parallel ray approximation and (b) finding the best-fit equivalent paraboloid through an RMS minimization procedure. The results from these approaches are compared with manual tuning of the feed location using exact PO analysis, i.e diffraction analysis with no approximations. For 35.75GHz, considerable pattern degradation can occur with small mechanical feed positioning errors, making the determination of the accurate optimal feed point critical. This study provides an effective way to judge the usefulness of the closed form expressions for the optimal feed position. Additionally, we also consider the effects of feed taper on the optimal feed location. The RMS deviation of the gores from the ideal paraboloid is related to the

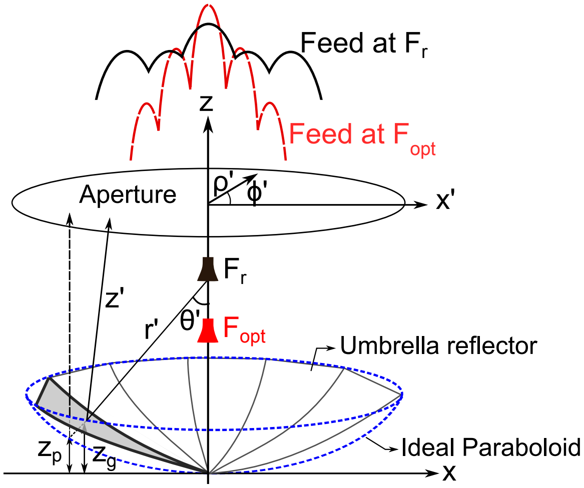

Figure 3.4: Finding the optimal feed position: The aim is to minimize the deviation in $r' + z'$. The dotted lines show the ray paths for an ideal parabolic reflector.

gain loss for various configurations.

3.2.1 Physical intuition behind the optimal feed location

The aperture field method of analysis can provide some intuitive hints to the methodology of choosing the feed position. We start by giving the general equation for taper efficiency in (3.8). The numerator essentially represents the power of the fields at boresight, which is proportional to the aperture electric field E_a, where it is assumed that all fields are oriented in X or Y direction. The denominator has two terms: The aperture area and the total power in the aperture. From the perspective of finding an optimal position, the total power in the aperture and aperture area can be assumed to be constant. Thus, we focus on the numerator of the efficiency equation.

$$\eta = \frac{1}{A_a} \frac{|\iint_s E_a ds|^2}{\iint_s |E_a|^2 ds} \tag{3.8}$$

Referring to Fig. 3.4, the aperture electric field can be described as

$$E_a = E_0(\rho', \phi') e^{jk(r'+z')} \tag{3.9}$$

The numerator of (3.8)) can thus be written as (3.10).

$$\left|\iint_s E_a ds\right|^2 = \left|\iint_s E_0(\rho\prime, \phi\prime) e^{jk(r\prime + z\prime)} ds\right|^2 \tag{3.10}$$

The aim is then, to maximize this expression. Now, for umbrella reflectors, moving the feed position will not significantly affect the amplitude distribution E_0. The critical term that needs attention in the phase term $k(r' + z')$. For parabolic reflectors, $r' + z'$ is a constant, with a tapered amplitude distribution E_0, resulting in maximum directivity along boresight. This is not the case for umbrella reflectors since the gore surface deviates from the paraboloid. The final aim, thus, is to minimize the deviation of this phase term on the aperture. This can be carried out using multiple approaches, as will be discussed subsequently.

3.2.2 Physical Optics approach

In [54], the parallel ray approximation is used to express the phase term in (3.10) as $\Delta f(1 + \cos\theta')$ where Δf denotes the deviation of gore focal length F_g from the feed location and θ' denotes the incident ray angle. Thus, the problem reduces to simply finding a feed point that minimizes Δf. Since the feed point is a constant point (independent of ϕ'), the optimal feed point just comes out to be the mean value of F_g and is thus given as:

$$\frac{F_{opt}}{F_r} = \frac{N_g}{\pi} \int_0^{\frac{\pi}{N_g}} \frac{\cos^2 \pi/N_g}{\cos^2 \psi} d\psi \tag{3.11}$$

where $\psi = 0$ represents the parabolic curve passing through the center of the gore and $\psi = \frac{\pi}{N_g}$ represents the rib. The integral in (3.11) can easily be evaluated as

$$\frac{F_{opt}}{F_r} = \frac{N_g}{2\pi} \sin \frac{2\pi}{N_g} \tag{3.12}$$

For large values of N_g, (3.12) can be expanded into its taylor series to yield

$$\frac{F_{opt}}{F_r} = 1 - \frac{2}{3}\left(\frac{\pi}{N_g}\right)^2 \tag{3.13}$$

3.2.3 Best fit approach

Another approach to find the optimal feeding point was highlighted in [55]. This approach involved finding a best-fit paraboloid to the umbrella reflector through an RMS error minimization process. Intuitively, the focus of this best fit paraboloid will be the point that minimizes the phase deviation at the aperture and would be the optimal feed position for the umbrella reflector system. The RMS error is defined as

$$\Delta z_{rms} = \sqrt{\frac{1}{A_g}\int_0^{\frac{D}{2}\cos\phi_\circ}\int_0^{y\tan\phi_\circ}(z_g - z_{eq})^2 dxdy} \tag{3.14}$$

where,

$$z_g = \frac{x^2 + y^2}{4F_g(\phi')} \tag{3.15}$$

$$z_{eq} = \frac{x^2 + y^2}{4F_{eq}} \tag{3.16}$$

where $\phi_\circ = \pi/N_g$ and $A_g = \frac{1}{4}(\frac{D}{2})^2 \sin 2\phi_\circ$. Note the correction in the integration limits for x and y in [55]. The optimal focal length is then found my minimizing the RMS error defined in (3.14). This can be done analytically, leading to the equations for optimal focal length and the corresponding minimum RMS error.

$$\frac{F_{opt}}{F_r} = \cos^2\phi_\circ \frac{1 + \frac{2}{3}\tan^2\phi_\circ + \frac{1}{5}\tan^4\phi_\circ}{1 + \frac{1}{3}\tan^2\phi_\circ} \tag{3.17}$$

$$\Delta z_{rms} = 0.010758\frac{D^2\cos^2\phi_\circ}{F_r}\frac{\tan^2\phi_\circ(1 + \tan^2\phi_\circ)}{\sqrt{(1 + \frac{2}{3}\tan^2\phi_\circ + \frac{1}{5}\tan^4\phi_\circ)}} \tag{3.18}$$

Refer to Appendix A for the derivation of (3.17) and (3.18). It is seen that for larger values of N_g, (3.17) can be approximated as (3.13). A comparison of the focal lengths got by (3.12), (3.13) and (3.17) is shown in Fig. 3.5. It is interesting to note that none of these formulations for the optimal feed point directly involves the frequency or the diameter of the reflector. For the RMS minimization procedure, the diameter of the reflector effects the RMS error but not the optimal focal length. It is worth noting that this approach is primarily geometry based. The inherent assumption in this approach is that the deviation of the umbrella reflector from the ideal paraboloid is small enough that minimizing the Δz between the gore and the paraboloid has the same effect as minimizing the phase deviation in the exit aperture. The authors in [55] report that this method was found suitable only when $\Delta z_{rms} < 0.08\lambda$. The elegance of this method lies in the fact that along with the optimal feed position, it predicts the RMS error between the umbrella reflector and the ideal paraboloid, allowing estimation of gain loss through Ruze's equation [56, 57], given as:

$$\Delta G(dB) = -685.811 \left(\frac{k \Delta z_{rms}}{\lambda} \right)^2 \tag{3.19}$$

where $k = (4F_r/D)\sqrt{\ln[1 + 1/(4F_r/D)^2]}$.

3.2.4 Manual tuning of feed position

In this approach, the feed is moved along the axis of the reflector and the reflector antenna performance is recorded for each feed location using an exact PO analysis, i.e. PO without any approximations, using the standard cosine-q feed model. The optimal feed location is the one that gives the minimum gain loss at boresight. This is an important investigation of the previous formulations, especially in the low gore regime, where the underlying assumptions may not be valid.

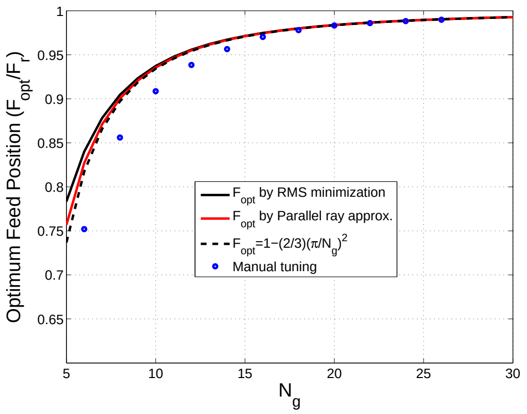

Figure 3.5: Comparison of the optimal feed positions got through (3.12), (3.17), (3.13) and manual tuning of feed position.

3.3 Results and discussions

A comparison between the optimal feed locations computed via the two approaches defined by (3.12), (3.17) and through manual tuning of the feed position is presented in Fig. 3.5. It can clearly be seen that none of the theoretical approaches result in the optimal feed location for $N_g < 15$ for an aperture of diameter 1m at 35.75GHz.

In order to assert the importance of accurate feed positioning, a particular case of $N_g = 10$ is taken up for analysis. Fig. 3.6 shows the gain loss computed through exact PO analysis as a function of feed position for $N_g = 10$. The gain loss is measured with respect to an ideal paraboloid illuminated with the same edge taper with feed at focus. Manual tuning predicts an optimal feed position of $0.4532m$ for $0dBtaper$ and $0.4540m$ for $-10dB$ taper. The optimal location predicted by (3.12), (3.17) and (3.13) results in the feed location being $0.4677m$, $0.4686m$ and $0.4671m$ respectively. Though $N_g = 10$ also reduces the physical aperture area, it only accounts for $0.4dB$ loss for the $0dB$ taper. For small feed displacements, the change in the spillover and the taper losses are not significant. Thus, the surface deviation due to gores is the primary reason for the gain loss. Note that the results of these analytical

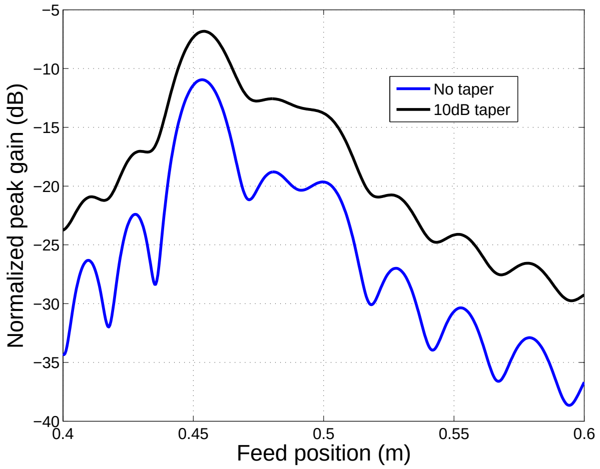

Figure 3.6: Variation of gain loss as a function of feed position for $N_g = 10$, $D = 1m$ and $F_r/D = 0.5$ at 35.75GHz as predicted by PO diffraction analysis.

formulations are independent of taper. This difference in the optimal feed positioning results in an additional loss of about 4.5dB with respect to keeping the feed at the position predicted by manual tuning. A significant observation here is also that the feed position does not heavily depend on taper as is predicted by both the theoretical approaches.

With $N_g = 10$ being studied in detail, a valid question that arises is the minimum value of N_g where the closed form expressions can be used. Fig. 3.7 shows a comparison between the optimal feed point predicted by (3.13) with the feed point preicted by manual tuning and their corresponding gain loss. It is clearly seen that the closed form expressions can be used when $N_g > 15$ ($\Delta z_{rms} = 0.11\lambda$). Thus, for $N_g < 15$ one must resort to manually tuning the feed position to get the optimal performance.

3.4 Extending the best-fit paraboloid approach: Effects of feed amplitude taper

To get the optimal aperture efficiency, the amplitude distribution at the aperture of the reflector antenna is tapered at the edges. The tapering reduces the effective aperture of the

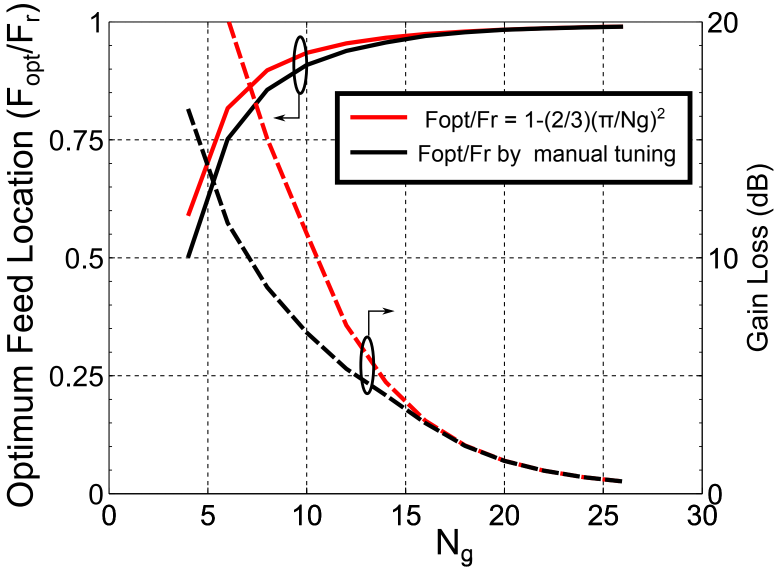

Figure 3.7: Comparison of optimal focal lengths predicted by (3.13) with manual tuning and the corresponding gain losses with reference to an ideal paraboloid.

antenna, but also minimizes the spillover. The PO with parallel ray approximation in [54] inherently accounts for the feed taper since the amplitude taper does not effect the aperture phase distribution. This implies that the optimal feed position computed by this method is independent of the feed taper. The best fit approach, however, must be modified since the taper causes the RMS error between the paraboloid and the umbrella reflector surface to get less significant as we move towards the rim of the reflector. Mathematically, this implies weighting the RMS error by a taper function. The simplest taper function for a circular aperture is given by (3.20), which represents a two parameter aperture distribution [53].

$$Q(\rho) = C + (1-C)\left[1 - \left(\frac{\rho'(x,y)}{R}\right)^2\right]^p \tag{3.20}$$

where,

$$Edge\,taper(ET) = 20\log_{10} C \tag{3.21}$$

$$\rho'(x,y) = \sqrt{(x'^2 + y'^2)} \tag{3.22}$$

and p controls the slope of the taper and R is the radius of the aperture. Typically, the value of p is set to 1.7 to correctly model the aperture distribution due to standard feed models. With this weighting function, the equation for the RMS error defined in (3.14) must be modified as:

$$\Delta z_{rms} = \sqrt{\frac{1}{A_g} \int_0^{\frac{D}{2}\cos\phi_\circ} \int_0^{y\tan\phi_\circ} (z_g - z_{eq})^2 Q(\rho') dx' dy'} \tag{3.23}$$

where $Q(x, y)$ is the weighting function given by (3.20). Before finding the RMS error, an important observation must be made about the aperture area: Due to the taper distribution, the area over which the RMS error is calculated reduces. The effective area can be computed by (3.24).

$$Aperture\ Area\ (A_g) = \int_0^{\frac{D}{2}\cos\phi_\circ} \int_0^{y\tan\phi_\circ} Q(\rho') dx' dy' \tag{3.24}$$

The detailed derivation of (3.23) and (3.24) is given in Appendix B. The value of the the equivalent focal length that minimizes the RMS is the optimal feeding position. It can be seen from Fig. 3.8 that for values of $N_g > 10$, the optimal feed position is almost independent of the taper. However, the taper significantly effects the minimum RMS error that is achieved; a uniform illumination (0dB taper) results in a larger RMS error than an amplitude taper of 10dB or 20dB. This is intuitive since the taper essentially leads to the rim of the reflector being weakly illuminated, which is the region of maximum surface deviation.

3.5 Aperture distribution and far field comparison

An important concern to address would be how much of gain do we recover by placing the feed at the optimal location. If there were an infinite number of ribs, the surface would be an ideal paraboloid of focal length F_r. Thus, we refer to F_r as being the reference focal length and the optimal feed location as the optimal focal length F_{opt}. Fig. 3.9a and 3.9b compare the far field patterns for the case where the feed is kept at the reference focus with the case

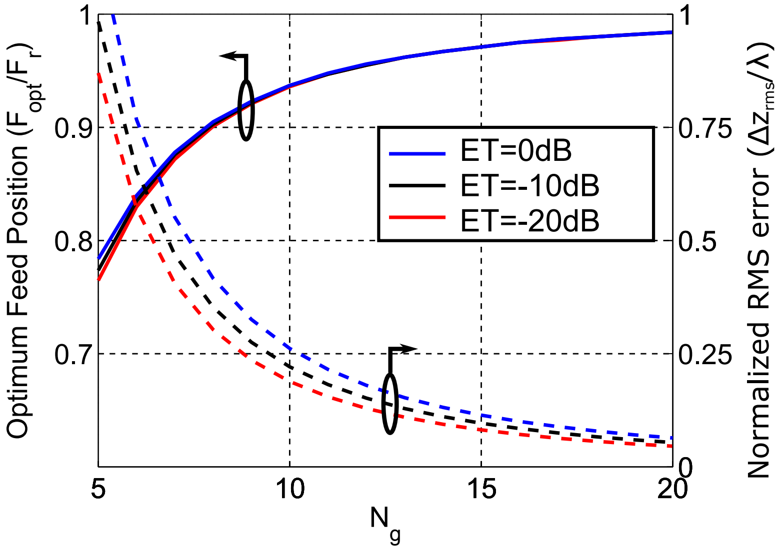

Figure 3.8: Variation of optimal feed position and RMS error for different values of N_g for various values of edge tapers based on (3.23).

where the feed is kept at the optimal focal point for various number of gores. The effects of mis-positioning the feed can very easily be seen: When the feed is kept at the reference focus, the patterns are much more broader with shallower nulls, leading to a sharp reduction in the gain. When the feed is kept at the optimal position, the nulls are much more filled in and the sidelobes are well formed. The boresight gain loss as a function of N_g is shown in Fig. 3.10.

3.5.1 Detailed study of an umbrella reflector with $N_g = 15$

The near field aperture distribution and the far fields for a representative case of a 15 rib umbrella reflector with aperture diameter 1m and $F_r/D = 0.5$. Fig. 3.11 shows the amplitude and phase distribution at the aperture of the antenna. It can be seen from Fig. 3.11a and Fig. 3.11b that the amplitude distribution is not significantly affected when the feed is moved from F_r to F_{opt}. This is intuitive since the absolute value displacement of the feed is small enough not to cause a significant difference in the amplitude. However, this displacement is significant when compared to the wavelength at 35.75 GHz. In this case

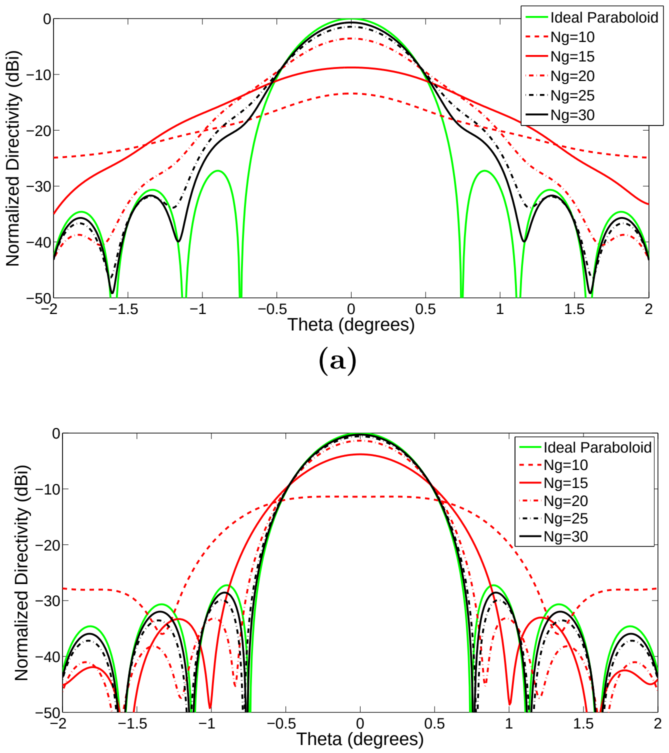

(a)

(b)

Figure 3.9: Comparison of far field patterns for various value of N_g when the (a) feed is kept at the reference position versus (b) when the feed is kept at the optimum focal length position.

of $N_g = 15$, an $F_{opt} = 0.971F_r = 48.55cm$. This implies a displacement of $1.45cm$, which translates to 1.73λ at 35.75 GHz. This can cause a significant change in the aperture phase distribution as seen in Fig. 3.11c and Fig. 3.11d. It can be observed that placing the feed at the reference position causes a significant amount of phase deviation in the aperture as compared to placing the feed at the optimal position. The phase deviation seen when the feed is at F_r manifests itself in the far field as a broader beam, causing the gain to decrease sharply, as illustrated in Fig. 3.12. Placing the feed at the optimum location recovers a significant amount of gain and the patterns begin to show better sidelobe features. For this case, it can be seen that placing the feed at the optimal position recovers 5dB of gain which is a substantial improvement.

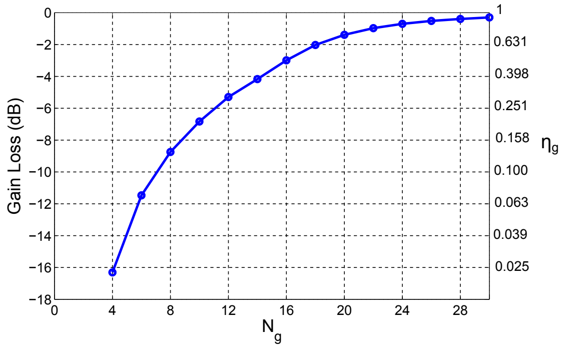

Figure 3.10: Variation of gain loss as a function of N_g when feed is kept at the optimum feed location got by manual tuning of the feed position.

3.5.2 Detailed far field discussion: grating lobes

As was noted in the previous discussion, the gores cause cyclical phase variations in the exit aperture. It is only intuitive to think that these cyclical variations would cause grating lobes in the far field [57, 58], which is a dominant reason for the reduction in boresight directivity. Equation (3.25) gives the approximate location of the grating lobes for N_g gores [59].

$$\sin\theta_g = \frac{N_g}{\pi D/\lambda} \tag{3.25}$$

As expected, for higher values of N_g, the location of grating lobe move further away from the main beam, to a point where the level is insignificant. For $N_g = 15$, $D = 1m$ at 35.75 GHz results in $\theta_g = 2.29°$. It is readily seen from Fig. 3.13 that grating lobes as high as -20dB occur close to 3°. These lobes can take significant energy from the main beam causing gain loss. Note that the position of the feed used for these plots is the F_{opt} given by (3.13), which is justified since it was shown that all formulations converge to the same value for $N_g = 15$.

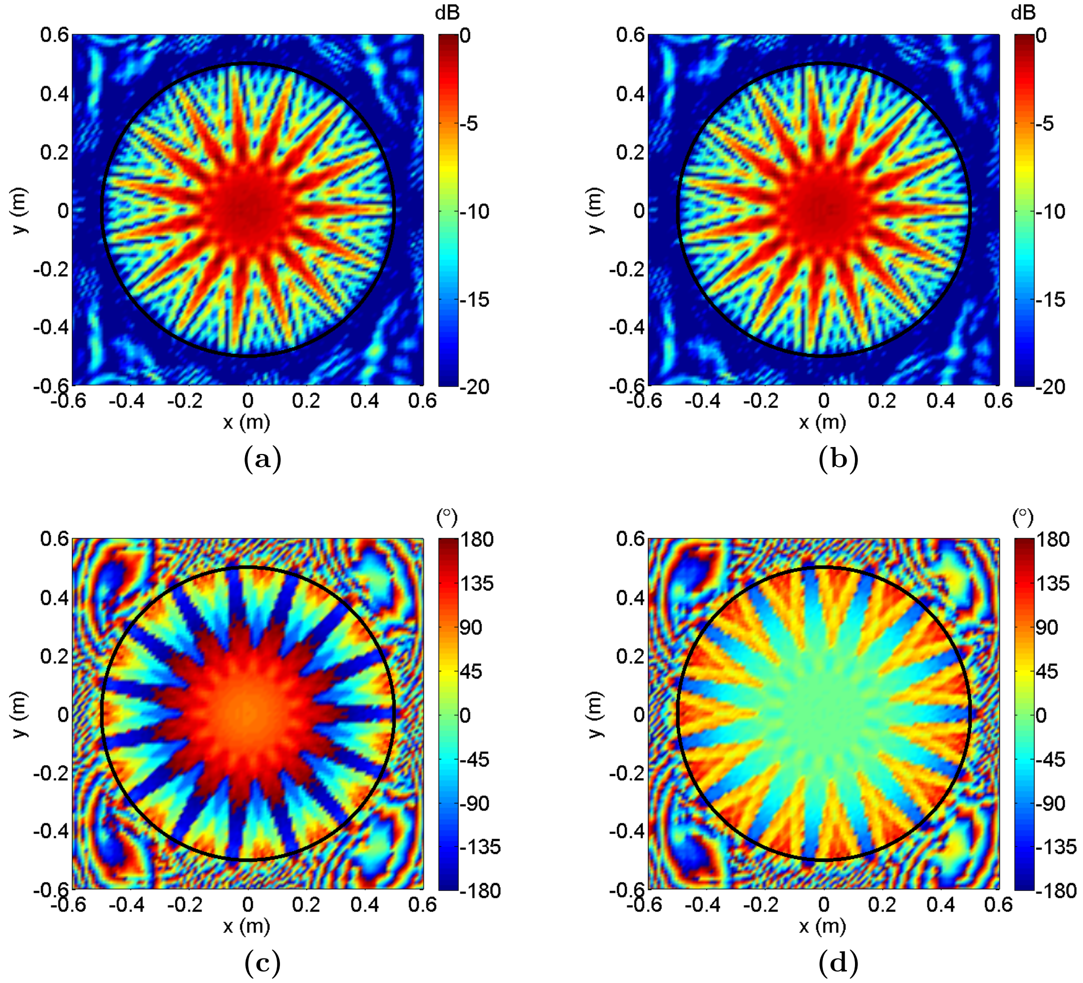

Figure 3.11: Aperture distributions of an umbrella reflector of $D = 1m$, $F_r/D = 0.5$ with $N_g = 15$ at 35.75GHz. (a) Amplitude distribution when feed is at the reference focus F_r. (b) Amplitude distribution when feed is at the optimal focus F_{opt}. (c) Phase distribution when the feed is at reference focus F_r. (d) Phase distribution when the feed is at reference focus F_{opt}. Note the uniformity of phase when the feed is kept at the optimum position.

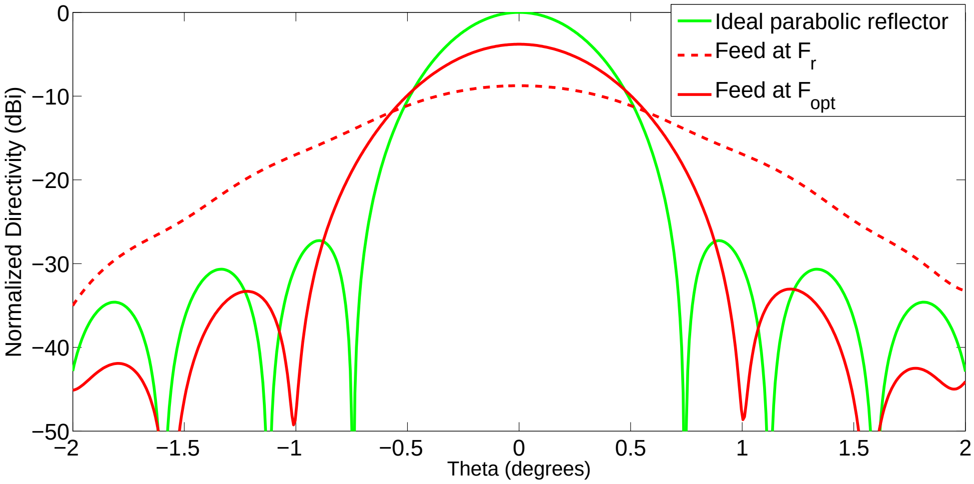

Figure 3.12: Comparisons between far field patterns for feed placed at F_r, F_{opt} and an ideal paraboloid for $N_g = 15$, $D = 1m$ and $F_r/D = 0.5$ at 35.75GHz.

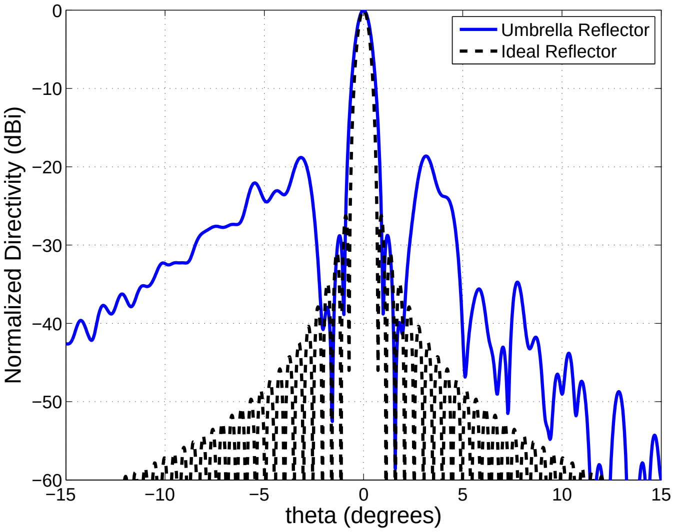

Figure 3.13: Grating lobes for $N_g = 15$. The estimated location from (3.25) yields $\theta = 2.29°$. The feed is located at F_{opt}.

CHAPTER 4

Mesh Characterization for Reflector Antenna Systems

Mesh reflector antennas are widely used for space applications where weight and deployability is a major concern. The surface of a mesh reflector consists of interwoven strands of conducting wires that are tensioned appropriately to maintain a parabolic profile. Though this reduces the weight, the openings in these surfaces cause some of the incident electromagnetic power to pass through the mesh surface, resulting in power loss. An immediate tradeoff can thus be seen: If the mesh is dense, the transmission loss through the openings reduces while adding weight and complexity to the system. Thus, a detailed analysis of mesh surfaces must be carried out in order to ensure a balance between optimal electromagnetic performance and mechanical complexity of the reflector antenna system. A common parameter used to characterize these mesh surfaces is the Number of Openings per Inch (OPI). In general, greater the OPI, the denser will be the mesh, resulting in smaller opening size of the mesh surface. As will be discussed in this chapter, the performance of the mesh surface depends on a variety of factors apart from just OPI. Parameters like the wire diameter, polarization of the incident wave, angle of incidence and the nature of contact at the junctions are critical to determine the loss due to the mesh surface.

4.1 Simple wire grid model

The simplest mesh surface to begin characterization of mesh surfaces is the simple wire grid model, which is illustrated in Fig. 4.1. This provides a very good starting point since it has already been analyzed in closed form by the Astrakhan's formulations. This formulation exposes many interesting electromagnetic properties of the wire grid mesh and can be very useful in developing a detailed understanding of the performance of mesh surfaces in general. The closed form expressions are also helpful for validating initial computer simulations before we use the computer tools to analyze advanced mesh features such as types of contact and characterize complex knit models.

4.1.1 Astrakhan's formulation

The Astrakhan's formulation derives the transmission coefficients of an infinite planar wire grid mesh through the method of average boundary conditions [60]. These formulations are valid if the inter-grid spacings of the mesh is less than $\lambda/5$. With reference to Fig. 4.1, the equations for a model with PEC wires that are soldered at the junctions are expressed in equations (4.1)-(4.11) [61]:

$$T_{TE-TE} = 1 - k_0 I_0^{-1}[cos\theta_i + k_0[\gamma_1 cos^2\phi_i + (\delta_2 - \delta_1)sin\phi_i cos\phi_i - \gamma_2 sin^2\phi_i]] \tag{4.1}$$

$$T_{TM-TE} = -k_0^2 cos\theta_i I_0^{-1}[\delta_1 sin^2\phi_i - (\gamma_1 + \gamma_2)sin\phi_i cos\phi_i + \delta_2 cos^2\phi_i] \tag{4.2}$$

$$T_{TE-TM} = k_0^2 cos\theta_i I_0^{-1}[\delta_1 cos^2\phi_i + (\gamma_1 + \gamma_2)sin\phi_i cos\phi_i + \delta_2 sin^2\phi_i] \tag{4.3}$$

$$T_{TM-TM} = 1 - k_0 cos\theta_i I_0^{-1}(1 - k_0 cos\theta_i[\gamma_2 cos^2\phi_i + (\delta_2 - \delta_1)sin\phi_i cos\phi_i - \gamma_1 sin^2\phi_i]) \tag{4.4}$$

$$\frac{I_0}{k_0} = cos\theta_i(1+k^2\delta_1\delta_2-k_0^2\gamma_1\gamma_2)+k_0 sin^2\theta_i[\gamma_2 cos^2\phi_i+(\delta_2-\delta_1)sin\phi_i cos\phi_i-\gamma_1 sin^2\phi_i]+k_0(\gamma_1-\gamma_2) \tag{4.5}$$

where

$$\alpha_1 = \frac{jb}{\pi} ln\frac{b}{2\pi r_0} \tag{4.6}$$

$$\alpha_2 = \frac{ja}{\pi} ln\frac{a}{2\pi r_0} \tag{4.7}$$

$$\gamma_1 = \alpha_1[1 - \frac{\frac{a}{b}}{1+\frac{a}{b}} sin^2\theta_i cos^2\phi_i] \tag{4.8}$$

$$\gamma_2 = -\alpha_2[1 - \frac{\frac{b}{a}}{1+\frac{b}{a}} sin^2\theta_i sin^2\phi_i] \tag{4.9}$$

$$\delta_1 = \alpha_1\frac{\frac{a}{b}}{1+\frac{a}{b}} sin^2\theta_i sin\phi_i cos\phi_i \tag{4.10}$$

$$\delta_2 = -\alpha_2\frac{\frac{b}{a}}{1+\frac{b}{a}} sin^2\theta_i sin\phi_i cos\phi_i \tag{4.11}$$

For a particular case where $a = b$, these equations simplify considerably with $\alpha_1 = \alpha_2$ and $\delta_1 = -\delta_2$. This leads to the following observations:

1. The transmission coefficients do not depend on ϕ_i, implying that the grid is isotropic in the azimuth plane.

2. $T_{TE-TM} = T_{TM-TE} = 0$. Thus, there is no cross polarization of the incident wave.

3. $T_{TE-TE} \rightarrow 0$ and $T_{TM-TM} \rightarrow 1$ as $\theta \rightarrow 90°$.

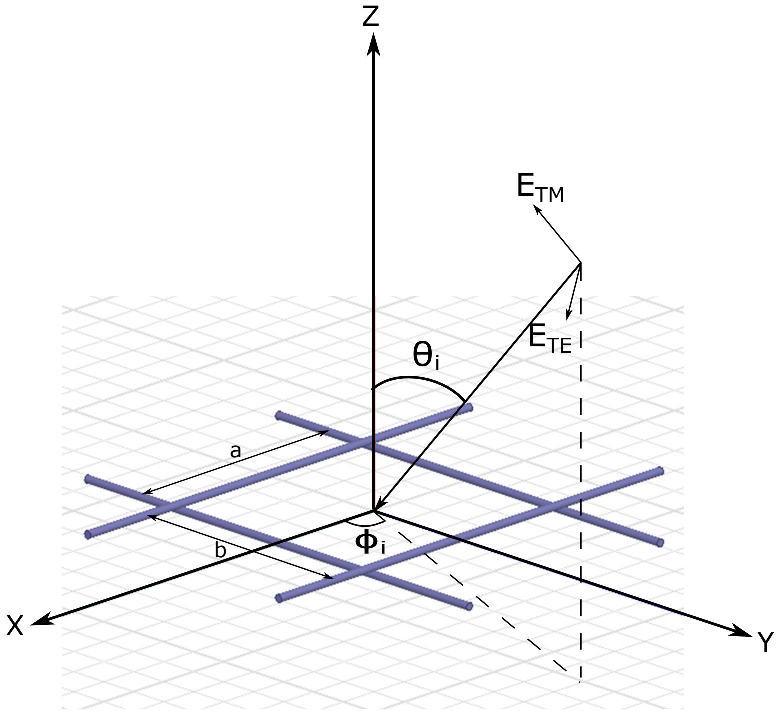

Figure 4.1: A periodic cell simulated in HFSS. The quantities a and b are measured from the center of one wire to the other. E_{TE} , E_{TM} denote the direction of electric field vector for TE and TM polarization respectively for a plane wave incident at an angle θ_i and ϕ_i.

4.1.2 Relating transmission coefficients to gain loss

The Astrakhan's formulation give the transmission coefficients of the simple wire grid model. However, we need some machinery to convert these transmission coefficients into gain loss that we expect to encounter when the surface is used as a reflector. Since the wires are assumed to be PEC, any power incident on it can either be transmitted through the mesh or reflected back. The fraction of the incident power that gets reflected back denotes the power lost due to the leakage from the mesh openings. Thus, the gain loss can be related to the transmission coefficients as:

$$\Delta G(dB) = 10log(1 - |T|^2) \tag{4.12}$$

The efficiency due to the mesh surface can then be expressed as:

$$\eta_m = 10^{(\Delta G(dB)/10)} \tag{4.13}$$

It should be noted that this approach is only to get a ballpark figure of the loss that one can expect from a mesh surface. A more rigorous approach was highlighted in [62]. This study involved estimating the currents on the surface of the curved mesh reflector by approximating the mesh to be locally infinite at the point where the electromagnetic waves from the feed are incident on it. The currents on each point in the reflector surface can be estimated as (4.14) [61].

$$\vec{J} = \hat{n} \times (\vec{H}_i + \vec{H}_r - \vec{H}_t) \tag{4.14}$$

Where $\hat{n}$ denotes the local unit normal vector, $\vec{H}_i$, $\vec{H}_r$ and $\vec{H}_t$ denoted the incident, reflected and transmitted fields respectively. The transmitted and reflected fields can be related to the incident fields via the local transmission and reflection coefficients. The far field radiation pattern of the mesh reflector antenna can be subsequently found by the vector potential approach.

4.1.3 Comparison of full wave simulation with the Astrakhan formulation

With the advances in computational technology, full wave simulators are capable of simulating very complex problems. However, it is essential to first simulate some problems for which the solution is known a priori so that the simulation results can be verified. Since the simple wire-grid model already has a closed form solution available, the results of the full wave simulation can be compared to the analytical solution as a starting point. For this, we used HFSS, which is a finite element solver. The simulation setup is shown in Fig. 4.2. Periodic boundary conditions (master/slave boundaries) are used to simulate an infinite planar mesh. This structure is excited by floquet ports. Only the two fundamental floquet modes (which are TE_{00} and TM_{00}) are used to emulate plane waves incident on the mesh.

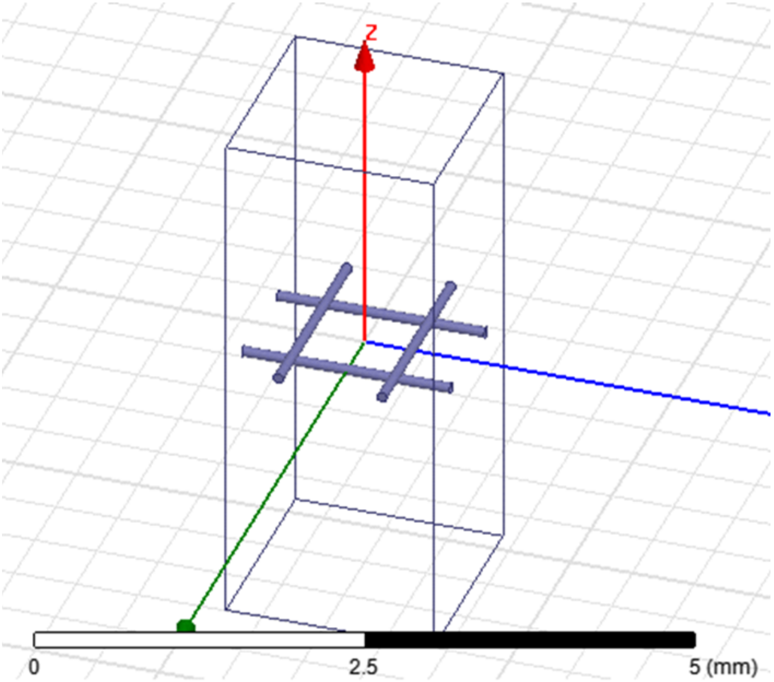

Figure 4.2: Simulation of periodic cell in HFSS. The walls of the bounding box that touches the mesh structure is assigned periodic boundaries and the face the is vertically above and below the mesh structure are assigned as floquet ports.

The angle of incidence can be controlled by varying the phase shift between the master and slave boundaries.

The results for the full wave simulations are compared with the Astrakhan formulations for the following cases:

1. Different OPI with same wire diameter and angle of incidence (Fig. 4.3).
2. Different wire diameters with same OPI and angle of incidence (Table 4.1).
3. Different values of θ_i for a constant ϕ_i with fixed OPI and wire diameter (Fig. 4.4a).
4. Different values of ϕ_i for a constant θ_i with fixed OPI and wire diameter. (Fig. 4.4b).

For each of these cases, the gain loss and the corresponding efficiency is compared, which are defined in (4.12) and (4.13). With NASA focusing on the frequency of 35.75 GHz for the deployment of future CubeSats for remote sensing applications, the same frequency is chosen for all simulations to follow. The wires are assumed to be PEC and the OPI is defined based on the distance between the centers of the two wires. Some key observations about these

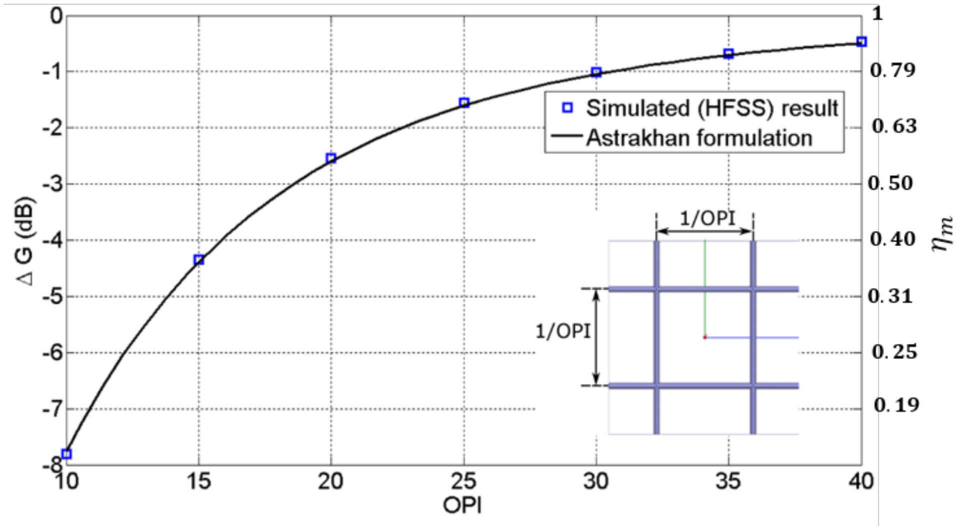

Figure 4.3: Comparison between HFSS and Astrakhan formulation for a wire diameter of 0.0008” for various OPI and normal incidence ($\theta_i = \phi_i = 0°$) at 35.75 GHz.

results are in order:

1. From Fig. 4.3, it can be seen that at Ka band, even a mesh of 40 OPI results in 0.5 dB of loss, which is significant. With lower frequencies, OPI as low as 10 can suffice, as was used in [63].

2. The diameter of the wires play a critical role. It can be seen from table 4.1 that doubling the diameter from 0.0008” to 0.0016” can reduce the loss by a factor of two. This observation is specially critical when analyzing with complex mesh surfaces, as will be discussed in the subsequent section.

3. The simulation results and Astrakhan’s formulation are in good agreement for the case oblique incidences too, as illustrated in Fig. 4.4a and Fig. 4.4b.

4.2 Hard and soft contact

An important consideration while analyzing the performance of mesh surfaces is the effect of contact at the junctions of the wires. The issue of contact in mesh structures has been

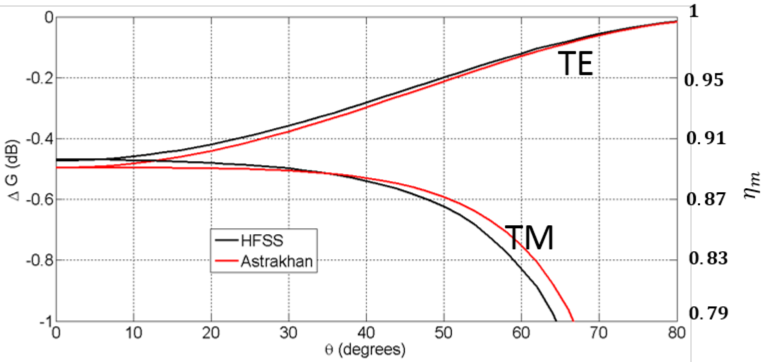

(a)

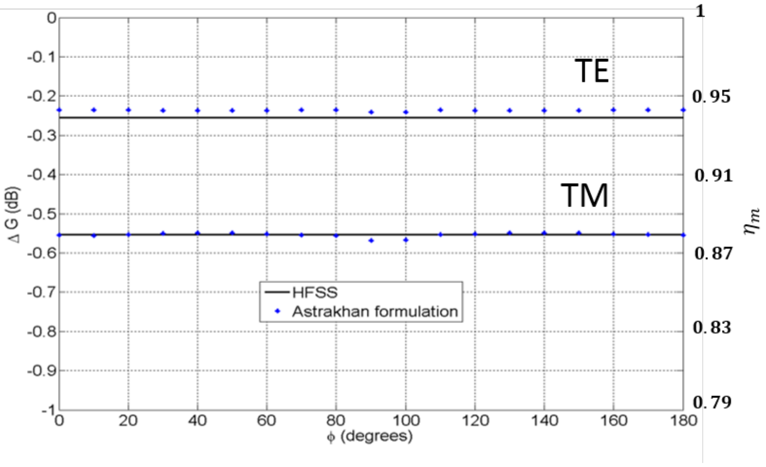

(b)

Figure 4.4: Comparison between Astrakhan's formulation and full wave simulations for a simple wire-grid model of 40 OPI and wire diameter of 0.0008" oblique incidence for (a)various values of θ_i when $\phi_i = 45°$ and (b) various values of ϕ_i when $\theta_i = 45°$.

studied comprehensively in the past. Reference [64] provides a brief summary of the effects of bonding the wires of the simple wire-grid model at the junction versus having no contact between wires. A rigorous analysis of bonded and unbonded junctions is done via floquet analysis in [65] and [66] respectively. A comprehensive review of the theory of wire grids developed till the year 1962 can be found in [67]. Reference [63] analyzed the affect of an imperfect contact at the junctions for a space reflector antenna to characterize the losses arising from imperfect contact at the junctions. However, these studies do not highlight a more subtle point: In a typical deployable reflector antenna system, the wires are held

Table 4.1: Comparison Between HFSS and Astrakhan Formulations for various diameters for normal incidence ($\theta_i = \phi_i = 0°$) and 40 OPI at 35.75 GHz.

Diameter	ΔG (dB)	
	HFSS	Astrakhan
0.0008”	-0.47	-0.49
0.0016”	-0.24	-0.25
0.002”	-0.17	-0.19
0.004”	-0.05	-0.05

together by the tension in the wires. Thus, the wires only touch each other at the junctions and are not soldered. This form of contact, where the wires only touch each other at the junction can be termed as ‘soft contact’, as opposed to a ‘hard contact’, where the wires are actually soldered at the junctions. The performance of hard and soft contacts are compared in Fig. 4.6. It is interesting to note that both forms of contact compare extremely well. One probable reason is that the diameter of the wires used to make the mesh is much smaller than the wavelength (0.0008” translates to $\lambda/800$ at 35.75GHz). From the canonical problem of scattering of plane waves from an infinite cylinder, it is known that the currents on the cylinder for such small diameter do not vary along the circumference of the wire, causing the currents on the top of the cylinder being almost identical to the current at the bottom. Thus, for both forms of contact, the junction still ‘sees’ the same current distribution, leading to an identical performance. The detailed derivation of scattering of a plane wave by a PEC cylinder is presented in Appendix C.

4.3 Complex mesh modeling and equivalent wire grid model

Based on the excellent agreement between Astrakhan’s results and full wave simulations, it is now possible to look into characterizing a representative knit model that is used to build the surface of mesh reflectors. The diagram of a tricot knit mesh is shown in Fig. 4.7a. This structure was analyzed in [63] using strip-wire equivalence in the frequency range of

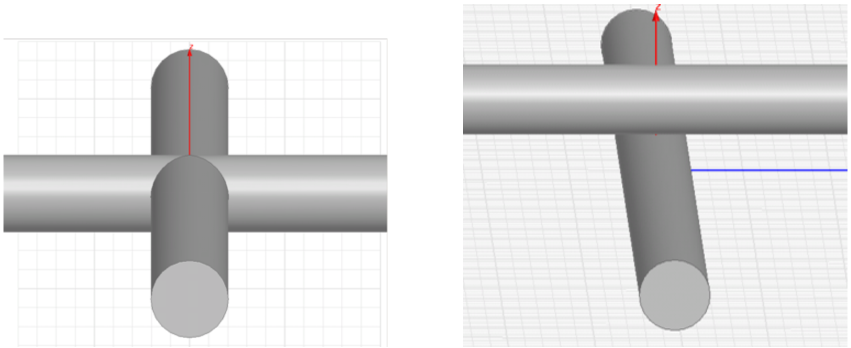

(a) **(b)**

Figure 4.5: Modeling of different Forms of contact. (a) Hard contact and (b) soft contact.

2-15 GHz. Here, we perform a full wave simulation of the structure using wires of diameter 0.0008" at 35.75 GHz. When presented with such a complex mesh surface, one can ask if there is a simpler equivalent model which can be used to estimate the performance of the mesh by using minimal computer resources in a reasonable time frame. The underlying principle behind building an equivalent model is the following: If can be seen from Fig. 4.7a that the mesh structure has a lot of intricate features. Since the spacing between the wires in such intricate zones would be much lesser than the wavelength (The unit cell by itself is of the order of $\lambda/13$ for 40 OPI), these regions can actually be estimated by a single strip. This process is shown in Fig. 4.7b. Finally, this strip model can be translated into the wire grid model using strip wire equivalence [68]. Table 4.2 compares the performance of this complex mesh with two wire grid models: one that has the same wire diameter as the ones used to make complex mesh and the other that has an equivalent diameter, which is estimated by the procedure previously described. Fig. 4.8 compares the performance of the complex mesh and the equivalent wire grid model for oblique incidence. It is very interesting to note the similarities in the performance of the equivalent wire grid model with the complex mesh surface. This procedure may thus be used to get a quick estimate of the performance of complex knit mesh surfaces.

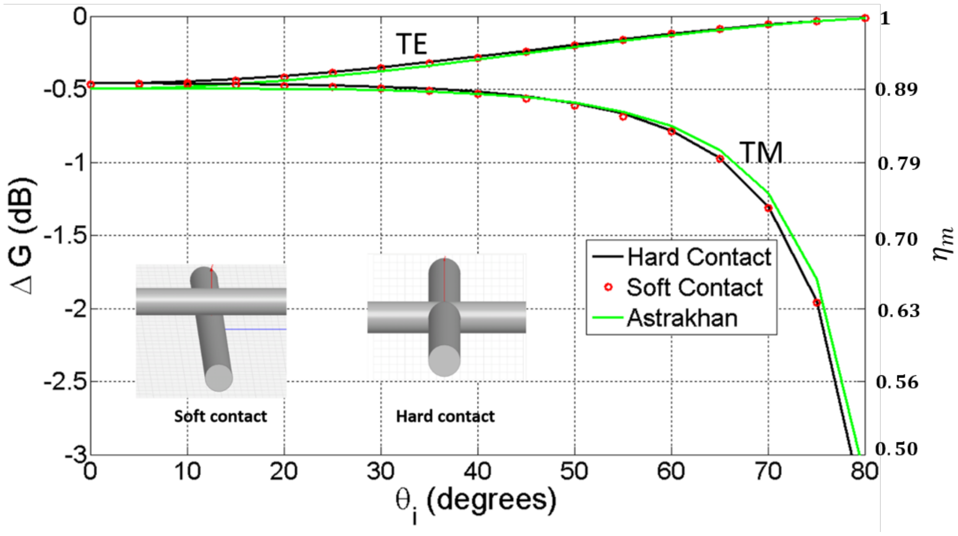

Figure 4.6: Comparison of the performances of hard and soft contact for $\theta_i = 45°$ for 40 OPI at 35.75 GHz.

Table 4.2: Comparison between tricot knit mesh and simple wire grid models for normal incidence ($\theta_i = \phi_i = 0°$) at 35.75 GHz. The Parameters D, W and OPI are as defined in Fig. 4.7.

OPI	ΔG (dB)		
	Tricot Knit Mesh	Wire Grid Model	
		D=0.0008”	D=W/2
20	-0.56	-2.53	-0.42
30	-0.19	-1.01	-0.19
40	-0.09	-0.47	-0.10

4.4 3D wire models

All the analysis until this section has always assumed that the surface of the mesh is planar i.e., the axis of all the wires that make up the mesh surface lie in the XY plane. However, in reality, these wires have to go ‘over’ each other at the junctions. This gives rise to the mesh surface being three dimensional. The 3D models can also have hard and soft contacts as can be seen from Fig. 4.9. The ‘height’ of the mesh surface is chosen to be 1/200” which translates to $\lambda/60$. It can be seen from table 4.3 that the performance of the 3D model

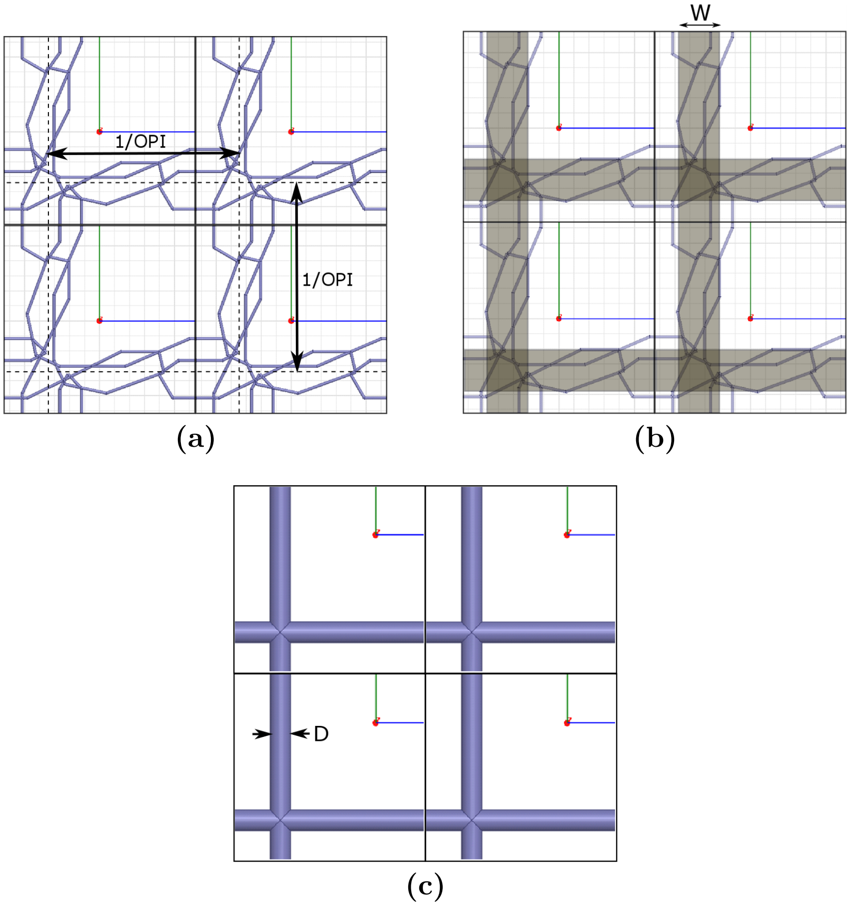

(a) **(b)**

(c)

Figure 4.7: A representative complex tricot knit pattern utilized to construct mesh reflectors [68]. (a) Mesh structure. (b) Equivalent strip model with strip width W, scaled according to the OPI. (c) Equivalent wire grid model of wire diameter D=W/2.

is not significantly different from that of the planar wire grid model for normal incidences. However, it can be seen from Fig. 4.10 that the performance for the 3D mesh deteriorates as the angle of incidence increases. This degradation can be attributed to the phase deviation on the aperture of the unit cell: for a planar mesh, when the waves come normal to the mesh, all points on the mesh see the same phase of the incident wave. However, the bumps cause greater phase deviation, whose affect is amplified as the angle of incidence increases.

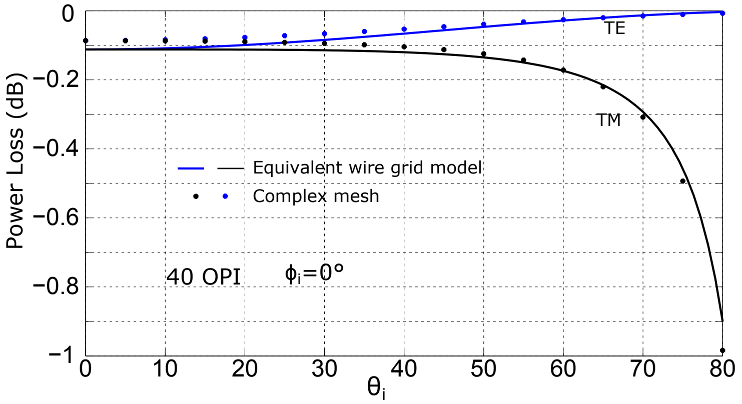

Figure 4.8: Comparison of the gain loss of the complex mesh with the equivalent wire grid model as a function of θ_i. The plane of incidence is $\phi_i = 0°$.

Table 4.3: Comparison of gain loss $\Delta G(dB)$ between the 3D wire model and simple wire grid model for normal incidence at 35.75 GHz.

OPI	3-D wire		Simple wire-grid model	
	Soft Contact	Hard contact	Soft contact	Hard contact
30	-1.08	-1.09	-1.01	-0.99
40	-0.55	-0.55	-0.47	-0.47

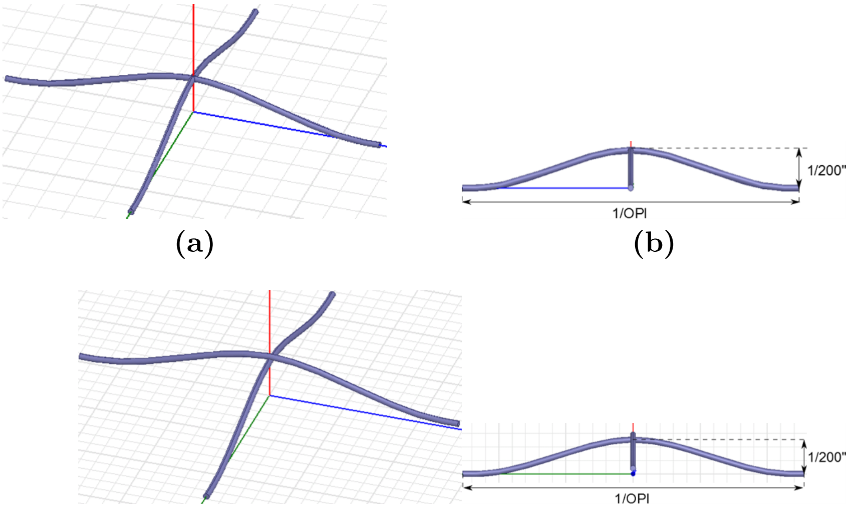

(a) **(b)**

(c) **(d)**

Figure 4.9: A representative 3D wire model. (a) Perspective view of hard contact. (b) Side view of hard contact. (c) Perspective view of soft contact. (d) Side view of soft contact contact.

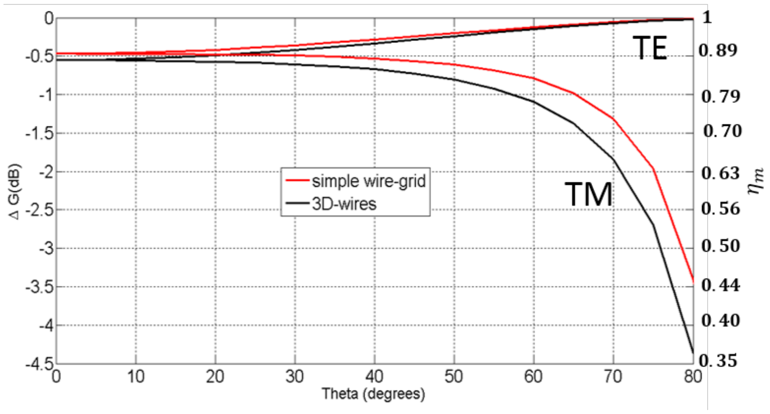

Figure 4.10: Comparison of the performances of 3D wire model and simple wire grid model with soft contact. Plane of incidence is $\phi_i = 45°$ for 40 OPI at 35.75 GHz.

CHAPTER 5

Selection of Reflector Antenna Configuration

Recent investigations for remote sensing at Ka band [52] have suggested an aperture near 1 meter, and therefore a 1m aperture diameter was targeted for the next evolution of high-gain CubeSat reflector antennas. Packaging the 1m reflector antenna into the 2.5U CubeSat chassis is a major engineering challenge. To address this, the first step is the selection of a reflector configuration that can provide the desired RF performance while maintaining reasonable mechanical complexity.

While designing reflector antennas, one is faced with a variety of options. Reflector systems can typically have just one reflecting surface or two reflecting surfaces (dual reflectors). Each one of them could be symmetric or offset, as illustrated in Fig. 5.1. Further, dual reflectors can be Cassegrain or Gregorian depending on the type of secondary reflecting surface. Selection of the appropriate configuration is critical from an electromagnetic as well as a mechanical standpoint. In this chapter, a brief overview of the tradeoffs between these configuration will be presented and some representative simulation results will be discussed.

5.1 Single reflector antennas

For single symmetric reflector antennas, the most appealing feature is the simplicity of design. The symmetricity in the current distribution results in zero cross polarization in the E and H planes, resulting in greater cross pol efficiency. Further, the single symmetric reflector antennas have typically small horn size requirements due to the large subtended angle. However, the blockage due to the feed can cause degradation of far field patterns.

Choosing an offset single reflector configuration alleviates some of these issues: the feed is totally clear of the main beam and thus, feed blockage is totally eliminated. This advantage comes at the cost of increased complexity of design and higher cross pol.

5.2 Dual reflector antennas

Dual reflector systems consists of two sets of reflecting surfaces. The rays from the feed horn first reflect off a secondary reflector, that forms the virtual feed for the main paraboloid reflector. Dual reflector antennas have a dominant advantage over their single counterpart in terms of the feeding structure. The feed horn can now be placed closer to the main reflector, folding the optics. Symmetric dual configurations suffer from feed blockage (similar to its single reflector counterpart) in addition to blockage from the subreflector. The blockage from the subreflector can be a major concern for dual reflector antennas since the subreflector surface directly lies in the direction of the boresight of the antenna. Reducing the size of the sub reflector can reduce the blockage to a certain extent. However, reducing the size of the subreflector requires the beamwidth of the horn feed to be narrower, thereby increasing its size. Offset dual configurations can mitigate the problem of blockage but result in increased cross polarization and mechanical complexity.

5.3 Performance comparisons of various reflector antenna configurations

In this section, a performance comparison of various reflector configuration that can meet the required gain and beamwidth specifications is presented. The starting point for this analysis was a paper published by JPL in collaboration with UCLA that conceptualized a 0.5m Cassegrain reflector antenna system for its potential use in CubeSats for deep space missions [47]. An antenna gain greater than 45 dB and beamwidth narrower than 0.7° at 35.75 GHz is required for advanced remote sensing missions. Thus, a reflector aperture size of

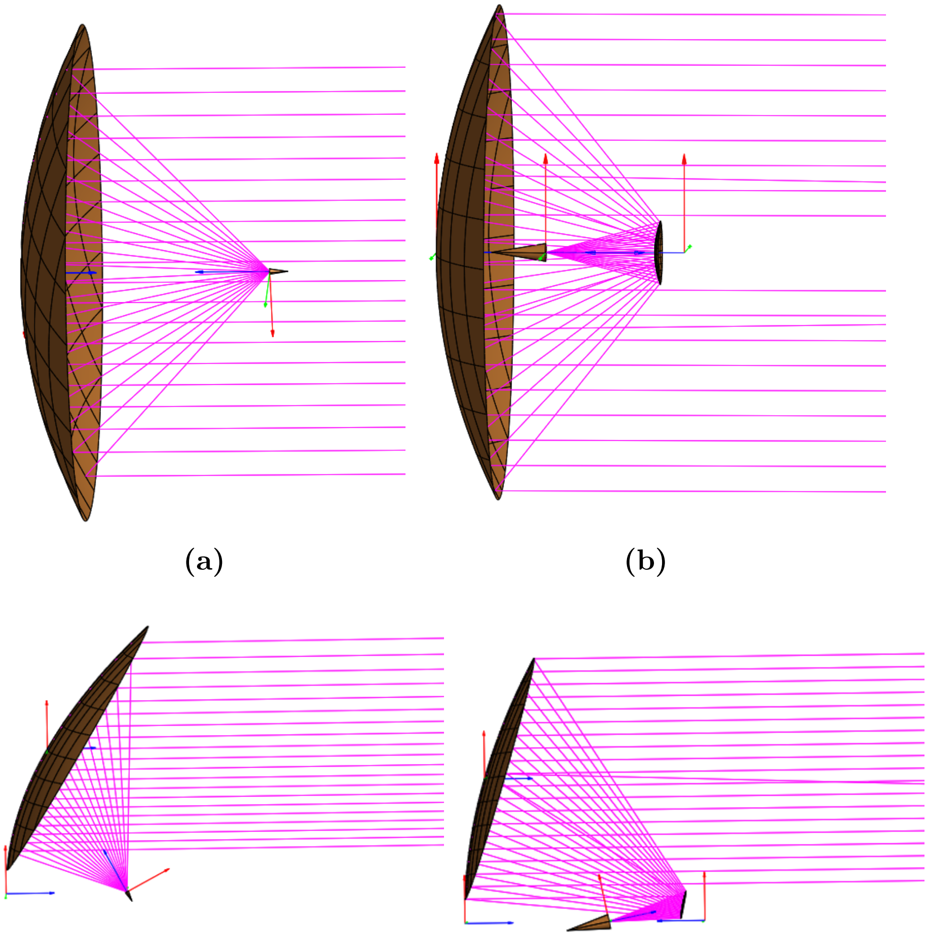

(a) **(b)**

(c) **(d)**

Figure 5.1: Representative diagrams of various reflector antenna configurations. (a) Single symmetric, (b) symmetric Cassegrain, (c) offset single and (d) offset Cassegrain. Note the size and position of feeds for various configurations. The dimensions for various configurations studied in this chapter are shown in Fig. 5.2 and Fig. 5.4.

1m was chosen, that can ideally provide a directivity of 51.45 dB with uniform illumination. Due to the aperture efficiency discussed in Chapter 2, the maximum possible gain is about 50.45 dB. Fig. 5.2 shows the geometries of the various configurations studied. The far field patterns for these cases are shown in Fig. 5.3. A comparison of directivities and beamwidths is presented in Table 5.1. In each case, a standard gaussian feed was used to provide a taper of 10 dB at the edges of the reflector. This taper determines the size of the horn feed due to the inverse proportionality between beamwidths and aperture area. Note that even without considering blockage, the boresight directivity of the dual reflector system is lesser than that of the single reflector system. A dominant reason for this is the finite size of the subreflector that leads to diffraction effects, leading to imperfect illumination of the main reflector. Other reasons include interference of backscattering from the subreflector and direct radiation from the feed with the fields radiated from the main reflector.

5.3.1 Symmetric reflector antennas

The symmetric reflector configurations that were investigated for the 1m reflector design are shown in Fig. 5.2. Fig. 5.2a represents a single symmetric reflector antenna with an aperture diameter of 1m and $F/D = 0.5$. Symmetric Cassegrain and Gregorian configurations are shown in Fig. 5.2b and 5.2c respectively. The F/D value is a critical aspect for packaging reflector antennas, since it dictates the curvature of the main reflector and the distance between the reflector and the feed. The Cassegrain reflector antenna that was developed in [47] for CubeSats at Ka-band for deep space missions was used as a reference for the initial designs. The far fields for these configurations are shown in Fig. 5.2. It can be seen that the dual reflector antennas have slightly higher sidelobes and shallower nulls due to interference from the feed and the back radiation from the subreflector. The Gregorian reflector antenna has a slightly greater cross-pol than the single and Cassegrain configurations. Table 5.1 compares the peak directivities, HPBW and efficiencies for the various configurations.

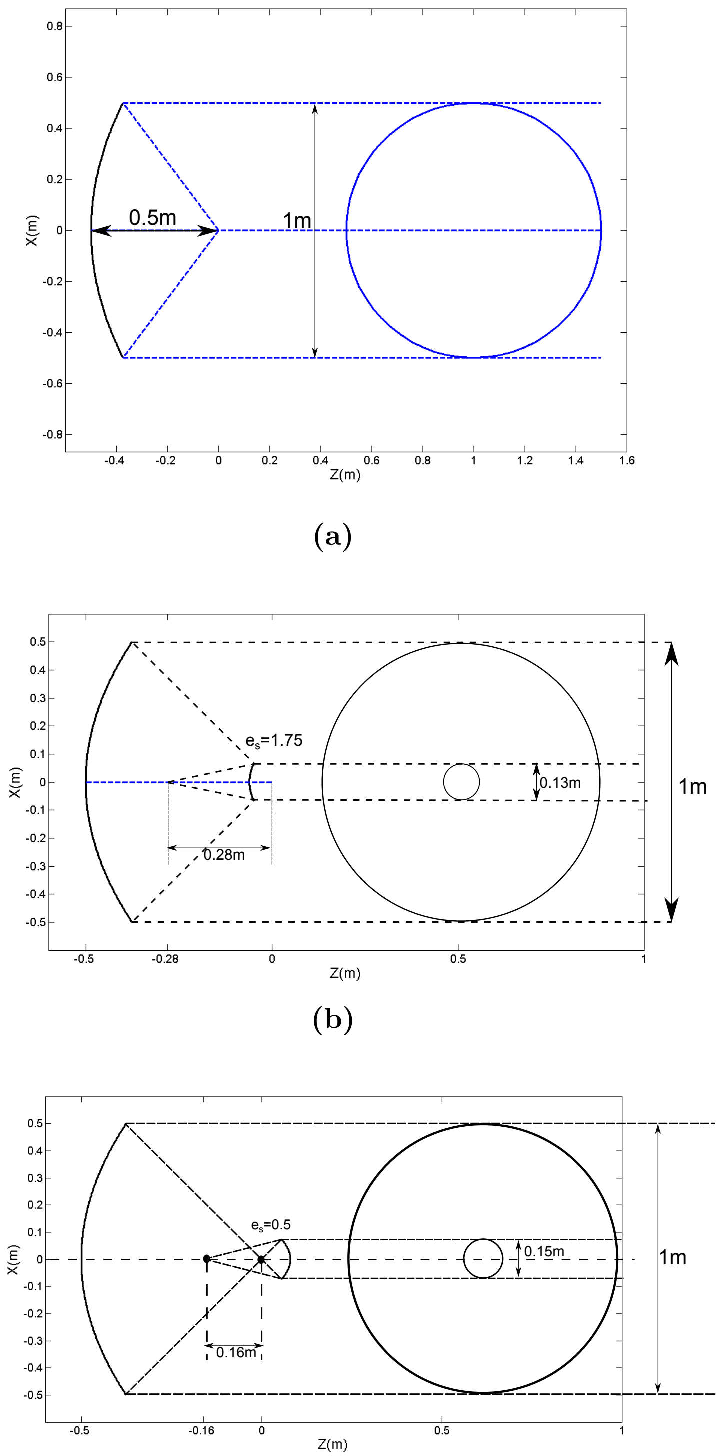

(a)

(b)

(c)

Figure 5.2: Symmetric reflector antenna configurations that were considered for the 1m reflector antenna design. All configurations have an $F/D = 0.5$ [47]. (a) Single reflector. (b) Cassegrain reflector. (c)Gregorian Reflector.

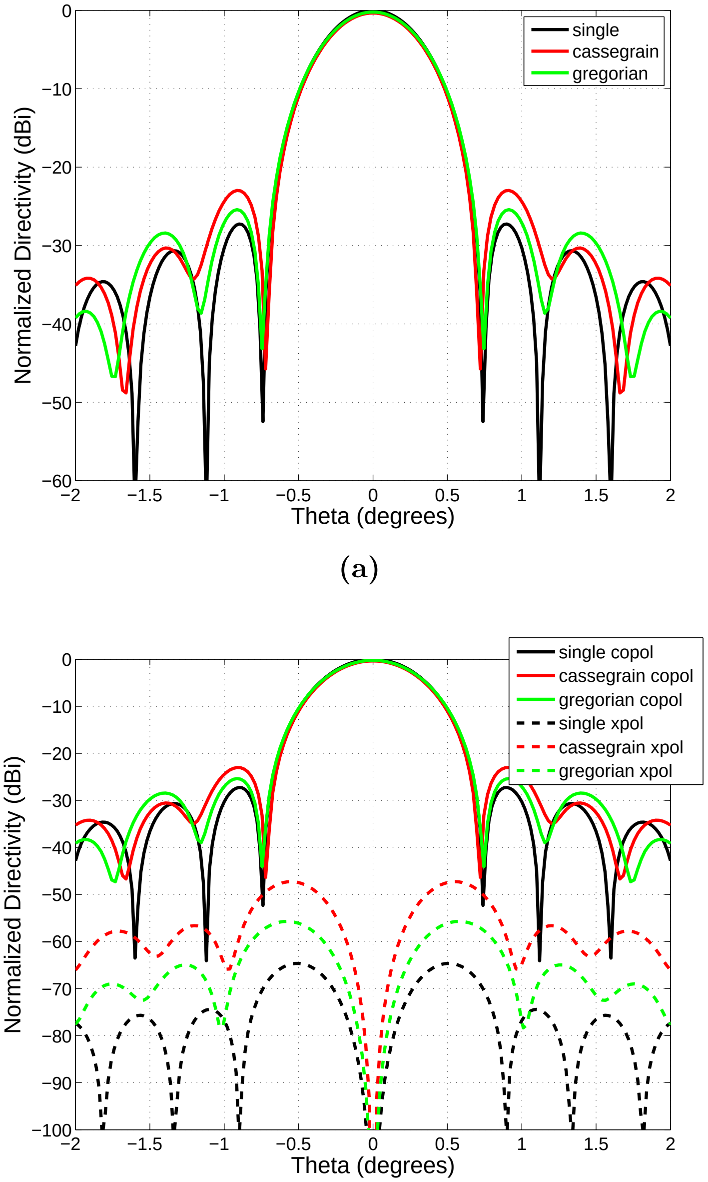

(a)

(b)

Figure 5.3: Radiation patterns for the symmetric configurations whose geometry was outlined in Fig. 5.2. Note that the subreflector blockage is not taken into account for these patterns. (a) E-plane pattern. (b) $\phi = 45°$ plane pattern.

Table 5.1: Directivity and beamwidth comparison for symmetric configurations studied for the 1m reflector design. The geometries are as shown in Fig. 5.2 and the patterns are shown in Fig. 5.3.

UNIFORM PHASE GAIN = 51.45 dB			
Configuration	Directivity (dBi)	HPBW	Efficiency (%)
Single	50.43	0.56	79.06
Cassegrain	50.08	0.56	72.94
Gregorian	50.20	0.56	74.98

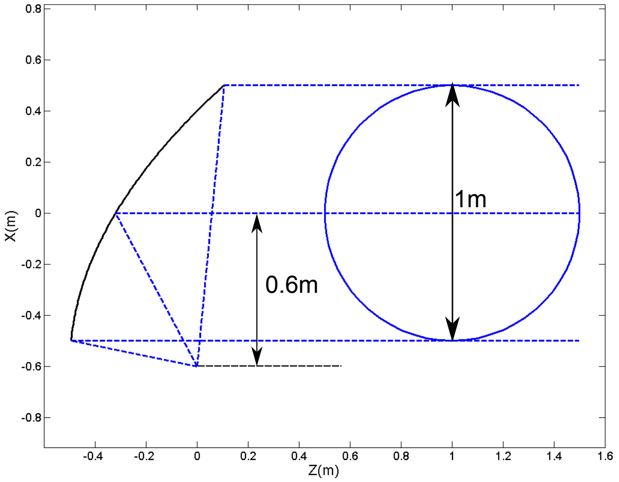

Figure 5.4: Potential single offset reflector antenna configuration investigated for the 1m antenna design.

5.3.2 Offset configurations

Apart from the symmetric configurations, the single offset reflector configuration could also be used for deployable antenna systems. One potential design that was tested is illustrated in Fig. 5.4. The far field patterns for this configuration is illustrated in Fig. 5.5.

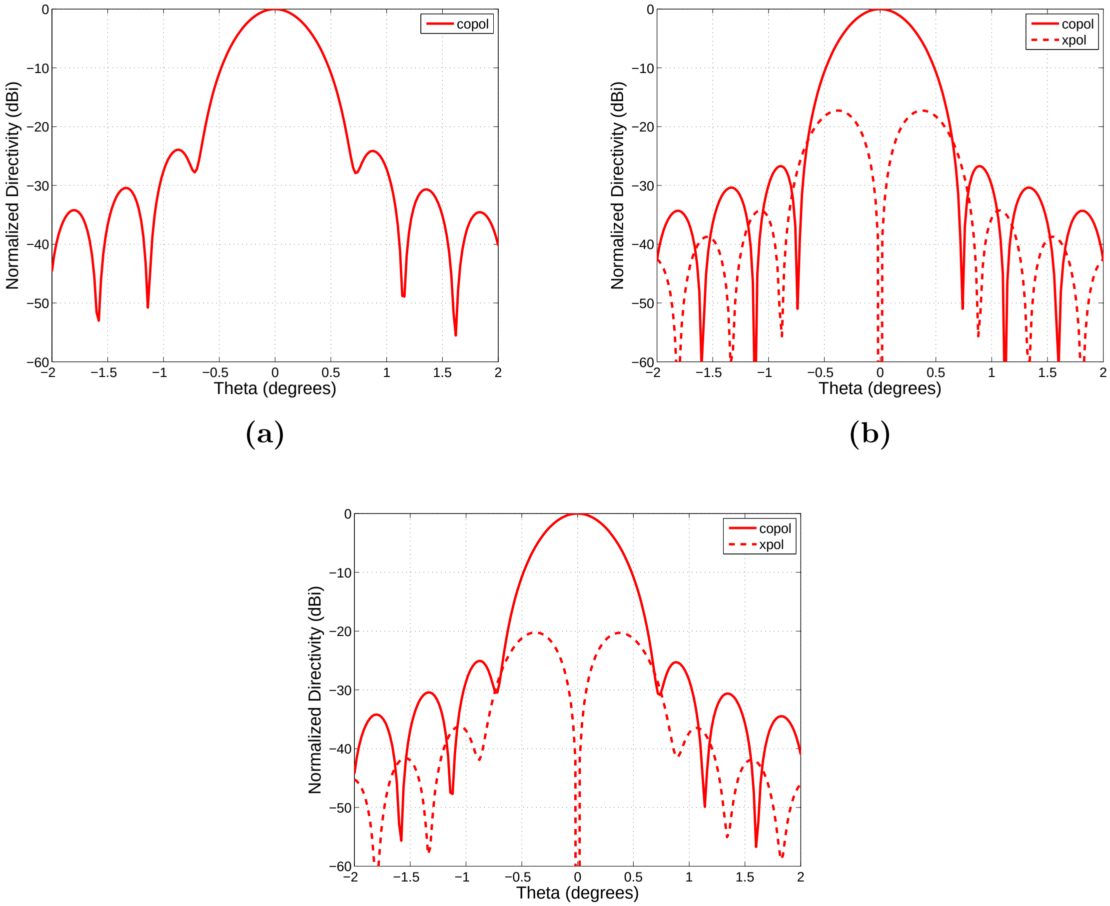

(a)

(b)

(c)

Figure 5.5: Radiation patterns for the offset reflector geometry outlined in Fig. 5.4. (a) E-plane pattern. (b) H-plane pattern. (c)$\phi = 45^0$ pattern.

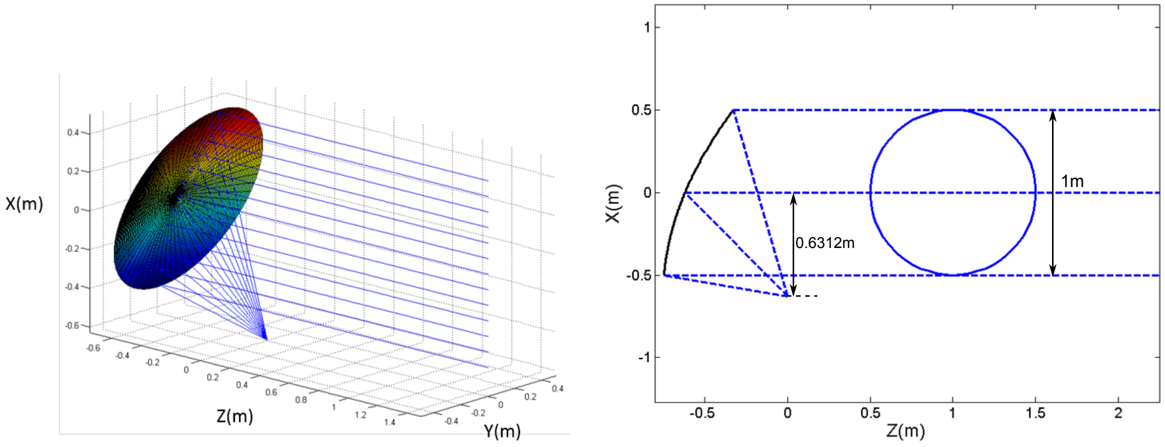

(a) **(b)**

Figure 5.6: The offset reflector antenna design chosen for Ka band remote sensing. The reflector is an aperture of diameter 1m and F/D of 0.75. (a) 3D representation. (b) 2D geometry.

5.4 Prospective configuration chosen for the 1m design

The study of the various pros and cons of each reflector configuration finally led to the selection of a single offset configuration. The offset design was found to be more feasible from a mechanical standpoint. The geometry is shown in Fig. 5.6. The far field patterns when a standard cosine-q feed is used to provide an edge taper of 10 dB is used is shown in Fig. 5.7. The subsequent chapter will focus on characterizing the feed for this design.

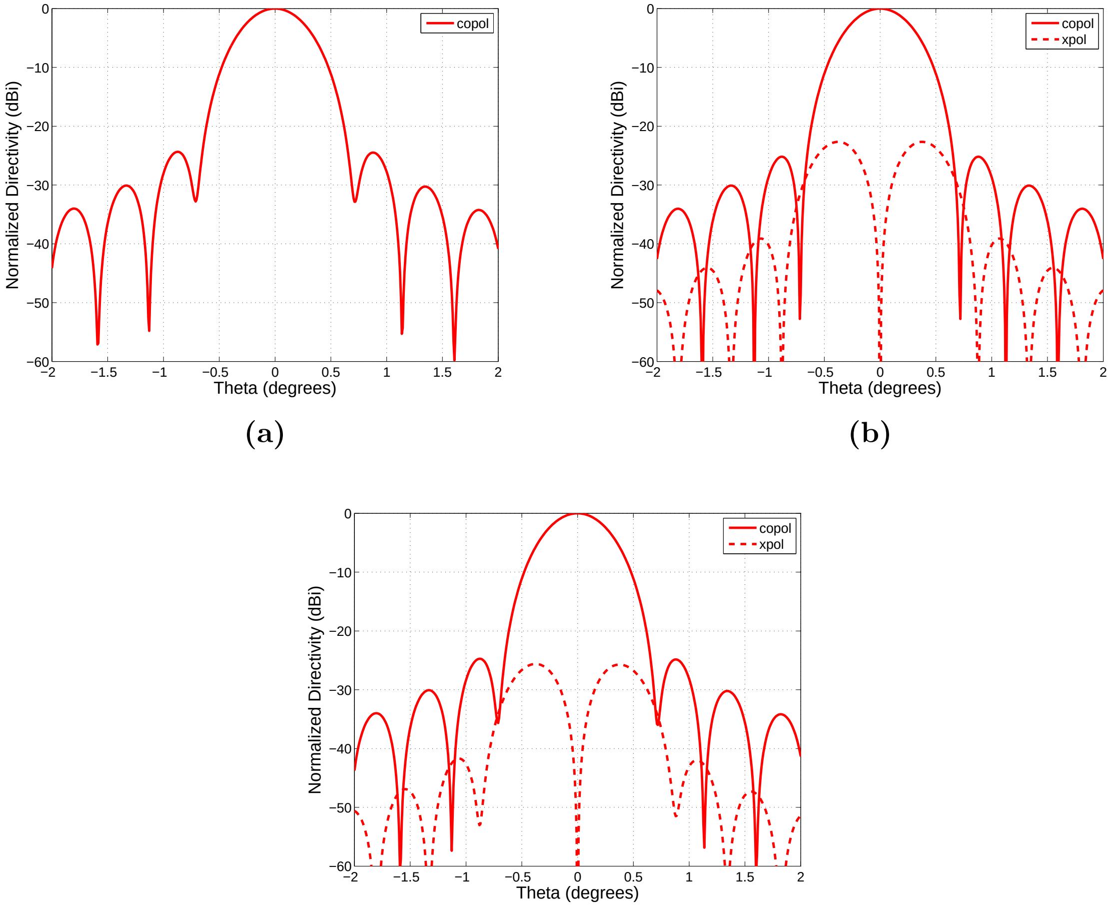

(a) **(b)**

(c)

Figure 5.7: Radiation patterns for the 1m offset reflector antenna shown in Fig. 5.6. The peak directivity is 50.50 dB. (a) E-plane pattern. (b) H-plane pattern. (c)$\phi = 45^0$ pattern.

CHAPTER 6

Feed Design and Reflector Antenna Simulations

The offset design that could potentially be used for Ka band remote sensing or communication applications was discussed in chapter 5. The geometry is repeated in Fig 6.1 for reference. This chapter will detail the steps taken towards designing an optimal horn feed for this reflector antenna design. In the analysis of reflector antennas, the cosine-q feed model is commonly used as a substitute for an actual horn for an initial estimation of the reflector performance. This feed model has no sidelobes, zero cross pol and zero backlobes and is thus termed as the 'idealized feed model'. A brief discussion on the cosine-q feed and its validity for reflector antenna analysis will be presented in this chapter. A comparative study between the reflector antenna performance when the horn feed is used vs. the cosine-q feed will also be elucidated.

6.1 Design specifications

To get the optimal aperture efficiency, the feed must illuminate the reflector such that the strength of illumination at the edge of the reflector is 10 dB below its value at the center. For the current design, the axis of the feed must be tilted at 45.65°. The feed pattern must reduce by 10 dB at and angular distance of 32.02° from its axis in the E-plane (XZ-plane) and 31.5° in the H-plane (YZ-plane) to get the optimal apperture efficiency of 80%.

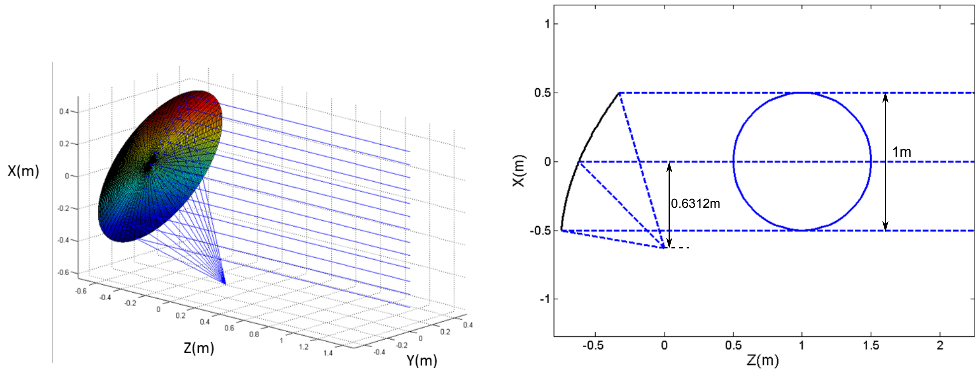

(a) **(b)**

Figure 6.1: The potential offset reflector design chosen for the 2.5U CubeSat for Ka band remote sensing. The reflector is an aperture of diameter 1m and F/D of 0.75. (a) 3D representation. (b) 2D geometry.

6.2 The ideal feed: cosine-q model

Cosine-q feed model is widely used in the field of reflector antennas to get a quick estimation of reflector performance. The mathematical equations that define the feed distribution for X and Y polarized feed is shown in (6.1)-(6.4) [53].

For X-polarized feed

$$E_\theta = E_0 \frac{e^{-jkr}}{r} \cos^{q_1}\theta \cos\phi \tag{6.1}$$

$$E_\phi = -E_0 \frac{e^{-jkr}}{r} \cos^{q_2}\theta \sin\phi \tag{6.2}$$

For Y-polarized feed

$$E_\theta = E_0 \frac{e^{-jkr}}{r} \cos^{q_1}\theta \sin\phi \tag{6.3}$$

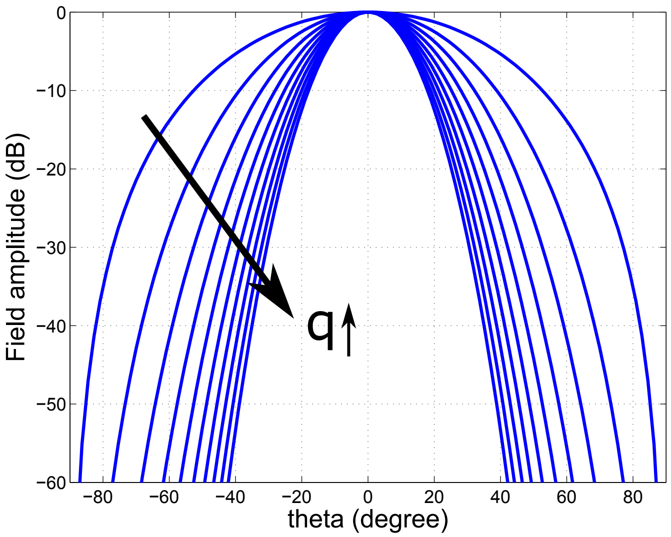

Figure 6.2: Plot of copol amplitude for various values of q_1 as a function of θ.

$$E_\phi = E_0 \frac{e^{-jkr}}{r} \cos^{q_2}\theta \cos\phi \tag{6.4}$$

where $-\frac{\pi}{2} \leq \theta \leq \frac{\pi}{2}$. For θ outside this range, the fields are assumed to be zero. A plot of the copol amplitude for various value of q_1 in the XZ plane is shown in Fig. 6.2.

Some observations about the cosine-q model can be made by looking at its equations:

1. The $\frac{e^{-jkr}}{r}$ term in the expressions signify that the radiation has a spherical wavefront. This is justified since for most practical single reflector antennas, the reflector is in the far field of the feed.

2. The distribution assumes all waves emanating from a point source at $r = 0$. This simplifies the analysis. For practical horns, however, the situation is more complex since a unique phase center cannot be defined for all observation directions. However, if the reference point for the far field phase of the horn results in a near constant phase in the region of interest (within the angular region over which the amplitude tapers by 10dB), the cosine-q model still emulates it well.

3. The factors q_1 and q_2 control the rate of decay of the distribution, as shown in Fig. 6.2. Thus, if a taper of ET (dB) is desired in the XZ plane at an angle of θ_0, the value of q_1 can be computed as:

$$20\log(\cos^{q_1}\theta_0) = -ET \tag{6.5}$$

which leads to

$$q_1 = \frac{-ET/20}{\log\cos\theta_0} \tag{6.6}$$

4. The cosine-q feed model has zero cross polarization as long as $q_1 = q_2$ The cross polarization is defined according to Ludwig's 3^{rd} definition [69] as shown in (6.7). This case often occurs for circular apertures. This is proven for an X-polarized feed by (6.7)-(6.8). A very similar derivation can be done for Y polarized feeds.

$$E_{cross} = \sin\phi E_\theta + \cos\phi E_\phi \tag{6.7}$$

substituting (6.1) and (6.2) with $q_1 = q_2 = q$, we have

$$E_{cross} = E_0 \frac{e^{-jkr}}{r} \cos^q\theta\,(\cos\phi sin\phi - \cos\phi\sin\phi) = 0 \tag{6.8}$$

A practical horn however has a non zero cross pol that is maximum in the plane oriented 45° to the polarization of the field. This cross polarization can be critical since it takes energy away from the co-polarized component, reducing gain. The cross polarization of the horn can be minimized by optimizing the horn or by using corrugated horns.

5. Since the cosine-q model is essentially a cosine function, whose amplitude depends on r and ϕ, the function does not have any sidelobes, as can also be seen in Fig. 6.2. This is the one of the most significant difference between this idealized feed model and an actual horn. Any practical aperture antenna will always have sidelobes, which can result in increased spillover. For certain applications, even the far-away sidelobes and the backlobes of the feed can be an important consideration, which the cosine-q feed does not model.

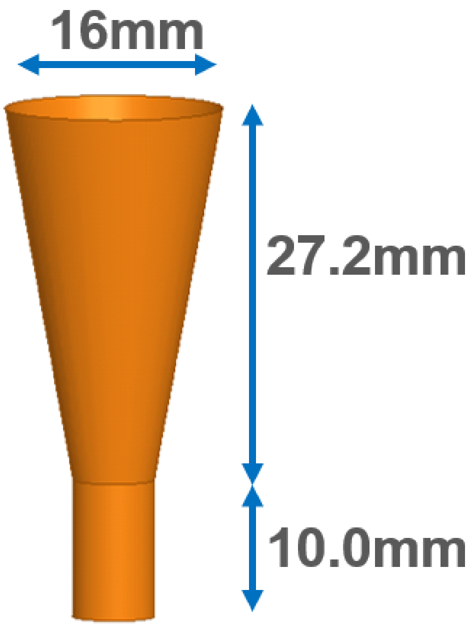

Figure 6.3: Initial horn geometry analyzed for the 1m offset reflector antenna configuration.

6.3 Initial horn design

An initial horn design that was analyzed to illuminate the 1m offset reflector antenna will be discussed in this section. The dimensions of the horn were chosen according to the standard design curves, to get minimal quadratic phase deviation at the aperture while maintaining minimum length and required 10dB beamwidths [70]. As a starting point, the directivity of the horn can be assumed to be similar to the cosine-q model, with the q chosen to provide the required 10dB taper at the reflector edges. The radius of the waveguide is chosen so that only the dominant TE_{11} mode propagates within the horn. The formula for calculating this minimum readius is given by (6.9).

$$\lambda_c = \frac{2\pi r}{1.841} \tag{6.9}$$

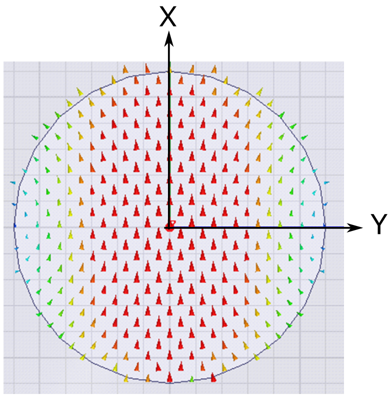

Figure 6.4: TE_{11} modal distribution at the input of the circular waveguide.

where r denotes the radius of the waveguide. For the current frequency of 35.75GHz, the value of radius can be evaluated as $0.25cm$. For practical considerations, the radius is chosen to be $0.3cm$. The modal distribution at the input of the waveguide is shown in Fig. 6.4.

6.3.1 Feed Patterns vs. cosine-q feed model

An important aspect of feed horn design is comparing the patterns of the horn to the ideal cosine-q model, since it directly gives an intuitive feel of the additional spillover and taper losses that can be expected when the horn feed illuminates the reflector. Comparison of the results from the horn and the idealized cosine-q patterns are presented in Fig. 6.5. The directivity of the cosine-q feed and the actual horn feed is 14.75dB and 15.05dB respectively. For a taper of 10dB at 32.02°, the value of of the q's can be computed as $q_1 = q_2 = 6.976$. Several observations are in order:

1. Unlike the cosine-q model where the beamwidths are independent of ϕ, the horn feed beamwidths depend on ϕ. This can be reasoned by observing the TE_{11} modal distribution shown in Fig. 6.4: The amplitude of the field remains almost constant in the E-plane and tapers off in the H-plane, causing the beam to be narrower in the E-plane and broader in the H-plane. Further, the amplitude distribution also results in the E-plane having greater sidelobe levels than the H-plane. This implies that this simple horn model cannot provide

a constant 10dB taper throughout the reflector aperture, causing an increased taper loss. Further, the sidelobes can increase spillover loss.
2. The horn has a non zero cross pol in the diagonal plane, which can result in power being lost to the cross pol, thereby reducing the gain of the reflector antenna.

6.4 Reflector antenna performance including horn feed

With the horn feed being thoroughly analyzed, the next step is integrating the feed with the reflector to assess the performance. The exact positioning of the horn antenna is an important question to address. For single reflector antennas, it is a safe assumption that the reflector is in the far field of the horn antenna. A uniform phase can be achieved at the aperture only if all rays from the feed emanate from the same point, i.e., all EM waves from the feed are purely spherical. In reality, the modal distributions within the horn do not allow a pure spherical wavefront to be radiated. In general, there is no unique point within the horn that can be assumed to be the originating point of the waves. Therefore, an approximate point has to be found which gives the minimum phase deviation in the far field. This point is called the phase center. If the phase center is not accurately determined, the reflector antenna performance can deteriorate, as will be discussed subsequently.

6.4.1 Phase center of the horn

Several studies have been conducted to determine the phase center of horns [71–73]. An approximate phase center can be found out by varying the origin for the far field coordinate system of the horn. The symmetry of the horn indicates that the phase center would be a point along the axis of the horn. Referring to Fig. 6.6 , it is desired to find Δz which provides the minimum phase deviation in the far field.

Through manual tuning, the phase center of for this horn was found out to be at $\Delta z =$

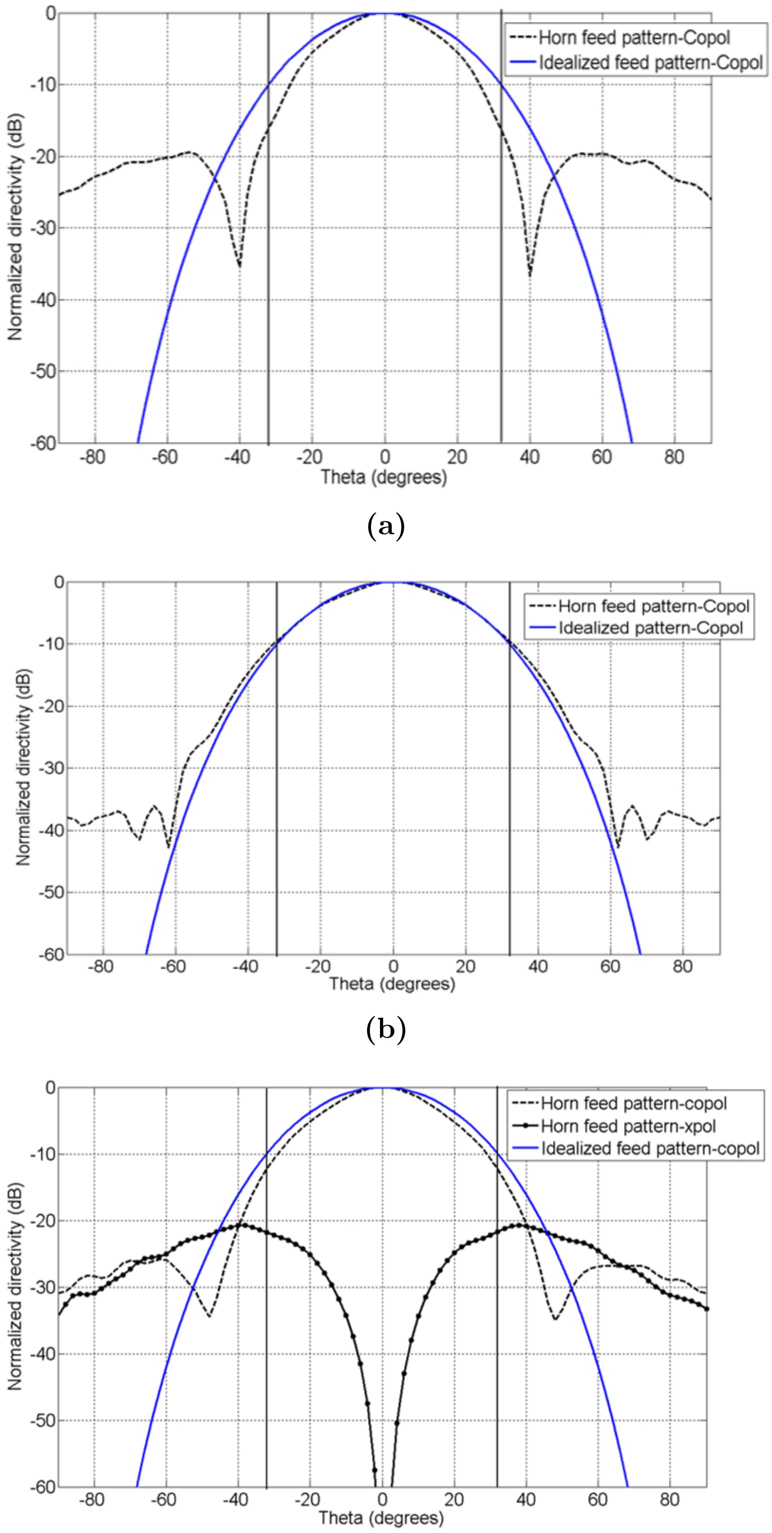

(a)

(b)

(c)

Figure 6.5: Comparison between the far field radiation patterns of the initial horn feed with the cosine-q feed model. (a) E-plane pattern. (b) D-plane pattern. (c) H-plane pattern.

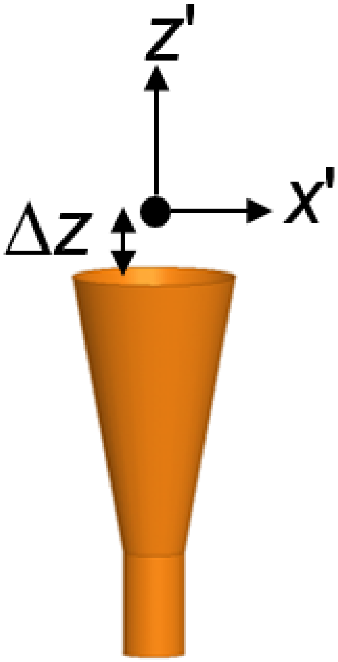

Figure 6.6: Determining the phase center of the horn. ΔZ is varied to determine the point which gives the minimum phase deviation in the far field. The dimensions of the horn are shown in Fig. 6.3.

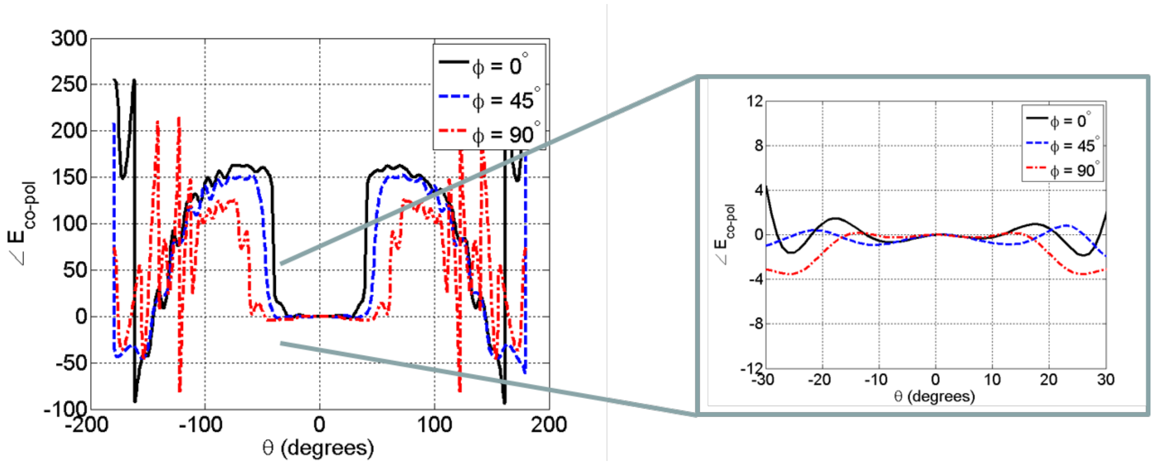

Figure 6.7: Far field copol phase of the horn when the origin of the far field coordinate system is kept at the phase center of the horn, which is at $\Delta z = -0.6mm$. The geometry of the horn is illustrated in Fig. 6.3.

$-0.6mm$, where Δz is defined according to Fig. 6.3. The far field phase distributions are illustrated in Fig. 6.7.

6.4.2 Reflector antenna simulation and analysis

The reflector antenna analysis is done using the PO solver of FEKO. The simulation setup is shown in Fig. 6.8. The feed patterns are imported into the simulation after simulating the horn by itself. Thus, the effects of the feed structure on the reflector performance is not taken into account. This is not a major concern due to the fact that the design is an offset reflector and inherently avoids feed blockage. Fig. 6.9 compares the reflector antenna performance when the horn feed is used vs. when the cosine-q feed is used. Several observations are in order:

1. The peak directivity of the reflector antenna using the cosine-q model is 50.50 dB, whereas the horn feed results in a directivity of 50.00 dB. This loss of 0.50 dB can be attribued to the sidelobes (that cause increased spillover) and cross polarization of the feed. The phase deviation of the feed also tends to reduce the directivity.

2. The sidelobe level in E-plane of the reflector antenna pattern is lower when the horn feed

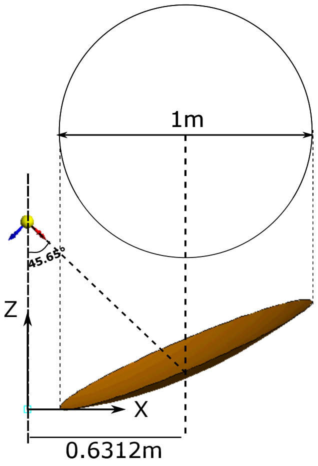

Figure 6.8: Simulation setup for PO reflector antenna analysis in FEKO.

is used compared to using the cosine-q feed. This is indicative of the fact that the horn feed provides a greater amplitude taper than the cosine-q feed in the E-plane, consistent with the comparisons between the cosine-q and the horn patterns in Fig. 6.5.

3. The H-plane reflector antenna patterns for both feeds models are in better agreement, which is indicative of the good match between the cosine-q feed model and the horn feed in the H-plane.

4. The reduction in peak directivity directly corresponds to beam broadening, A comparison of the HPBW is shown in Table 6.1.

5. The horn feed results in a greater cross pol level in the D-plane. This can be attributed the the additional cross pol of the horn field itself in the D-plane as was described in the previous section detailing the differences between the cosine-q and the horn patterns.

6. The increased sidelobe level in the E-plane of the horn contributes to greater spillover. This reduces the spillover efficiency of the system.

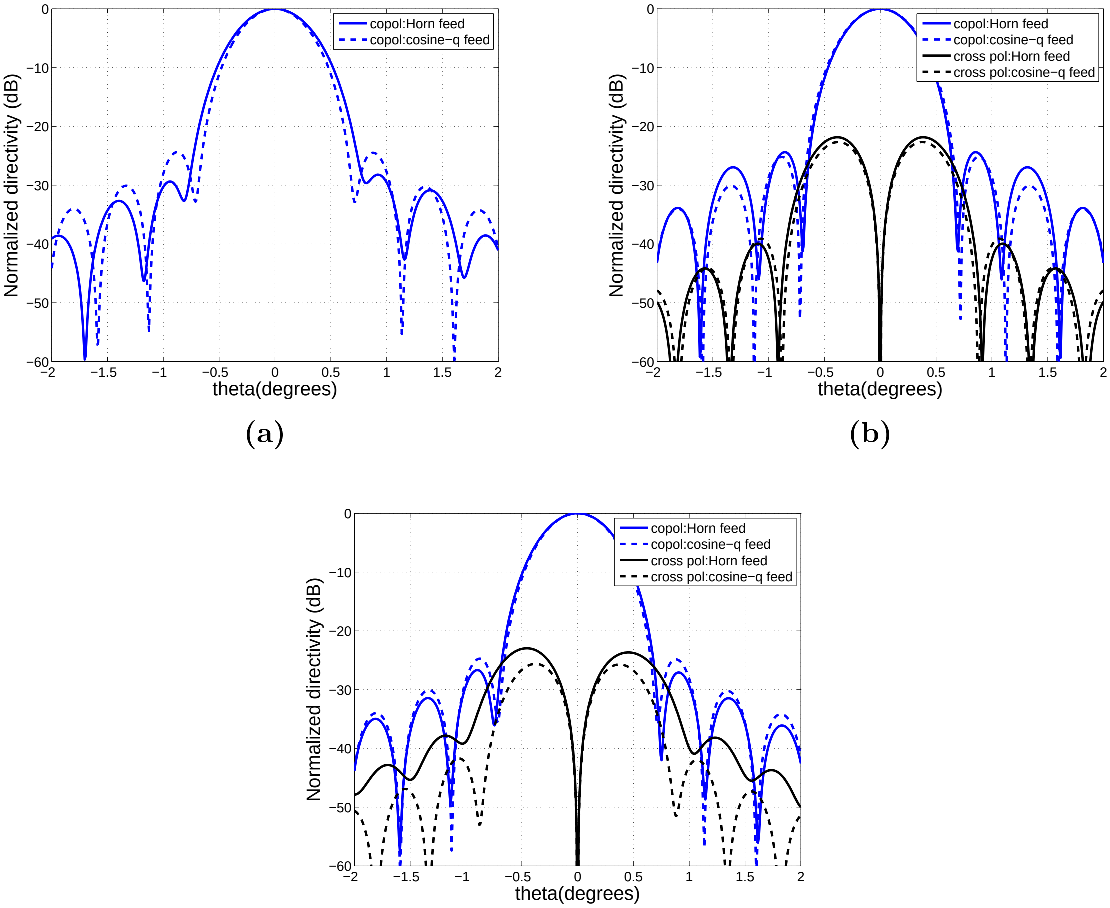

(a) **(b)**

(c)

Figure 6.9: Reflector far field patterns. (a) E-plane. (b) H-plane. (c) D-plane.

Table 6.1: Comparison of Half Power Beamwidths when the reflector is fed by cosine-q model and when fed by the horn.

	Horn feed	Cosine-Q feed
E-Plane	0.59°	0.569°
H-Plane	0.579°	0.569°
D-plane	0.549°	0.569°

6.5 Effects of feed patterns on reflector antenna performance

The last section described the radiation patterns of the reflector antenna when illuminated with the conceptualized horn. It was seen that the peak directivity of the reflector system was about 0.5dB lower when the horn feed used, as compared to using the cosine-q feed. This was primarily attributed to the following factors:

1. Increased edge taper from the horn in E-plane.
2. Increased sidelobes/backlobes causing excessive spillover.
3. Cross polarization generated from the feed.

In this section, a parametric study of the performance of the reflector system will be done to study which of the three plays a dominant role in reducing the directivity. To do this, the far field patterns of the feed are post processed to remove sidelobes (i.e., force zero fields beyond 10dB taper), or remove cross pol, and the reflector system is simulated to observe the effects of the feed pattern on the reflector pattern. Note that the horn itself is not modified in anyway.

6.5.1 Feed without cross-pol

The reflector antenna patterns when the cross pol in the feed is forced to zero is illustrated in Fig. 6.10. The peak directivity in this case is 50.16dB and the beamwidths in the E and H planes are 0.60° and 0.54° respectively. Note that the cross pol in the D and H planes are identical to the one got by the cosine-q feed. This reduction in the xpol results in 0.16dB improvement in the directivity.

6.5.2 No sidelobes with xpol

The far field reflector pattern when the radiation pattern of the feed is forced zero beyond the 10dB taper point is illustrated in Fig. 6.11. The peak directivity in this case is 50.46dB. The E and H planes have a HPBW of 0.61°, 0.55° respectively. It can be seen that though

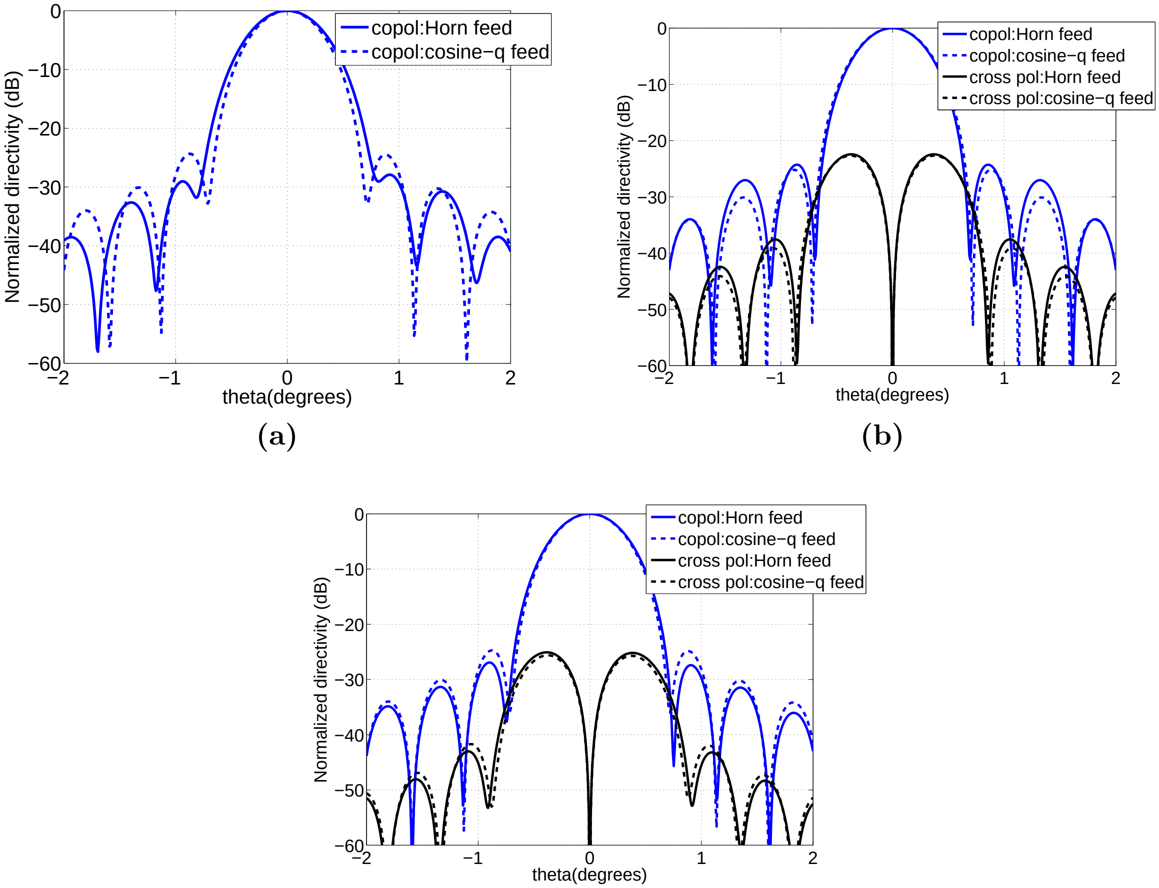

(a)

(b)

(c)

Figure 6.10: Reflector antenna far field patterns with the cross pol of the feed forced to zero. (a) E-plane. (b) H-plane. (c) D-plane.

the xpol in the D-plane increases, the reduced spillover causes the efficiency to be higher, increasing the directivity by 0.46dB. It should be noted here that the cosine-q feed model inherently has a spillover since the value of the field at the edges is only -10dB relative to the center.

6.5.3 No sidelobes without xpol

This case is similar to the previously described case, but with the cross pol forced to zero. The far field patterns are illustrated in Fig. 6.12. The peak directivity in this case is 50.49 dB and the beamwidths in the E and H plane is 0.60° and 0.54°. Note the slight improvement in comparison to the previous case of no sidelobes with cross pol.

6.5.4 No backlobes

For this case, the radiation of the feed 'behind' the horn aperture is set to zero. That is, $\vec{E}(\theta \geq 90^\circ) = 0$. The other sidelobes and cross pol are retained. The patterns are shown in Fig. 6.13. The directivity, E-plane HPBW and H-plane beamwidth are 50.08dB, 0.59° and 0.55° respectively.

6.6 Summary and conclusions

The cases described previously are summarized in Table 6.2. It can be seen that the dominant reason for the drop in efficiency is the spillover due to the sidelobes of the horn. The backlobes and cross polarization of the feed do not decrease the directivity drastically. The beamwidths do not change drastically for any of these cases, implying that the phase deviation at the exit aperture does not get affected as the feed far field pattern changes. Thus, to maximize the efficiency of the system, a horn with the minimum sidelobe level must be designed. However, the modal distribution within the horn will always give rise to sidelobes. This, along with the size, weight and beamwidth requirements make it imperative to use optimization techniques

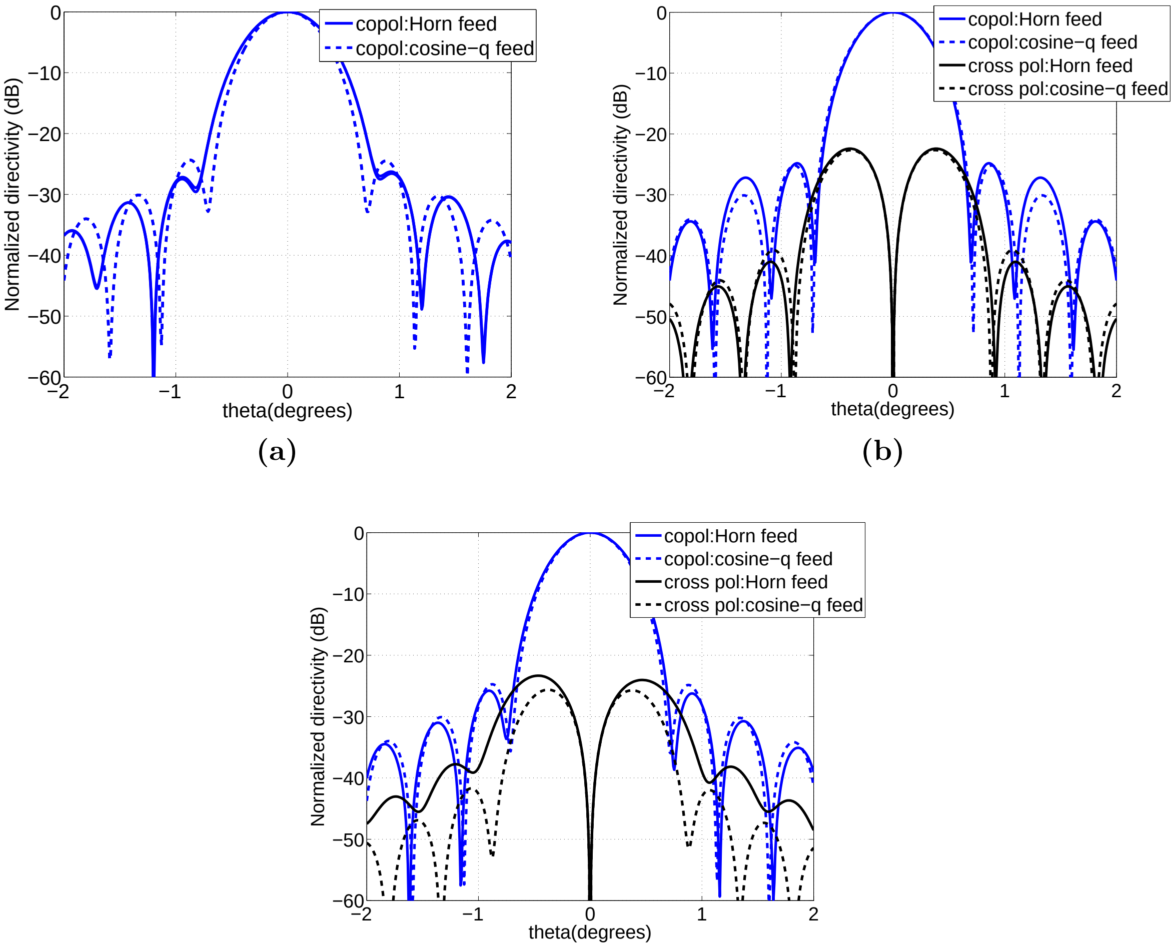

(a) **(b)**

(c)

Figure 6.11: Reflector antenna far field patterns with the sidelobes of the feed suppressed. The cross pol is unchanged. (a) E-plane. (b) H-plane. (c) D-plane.

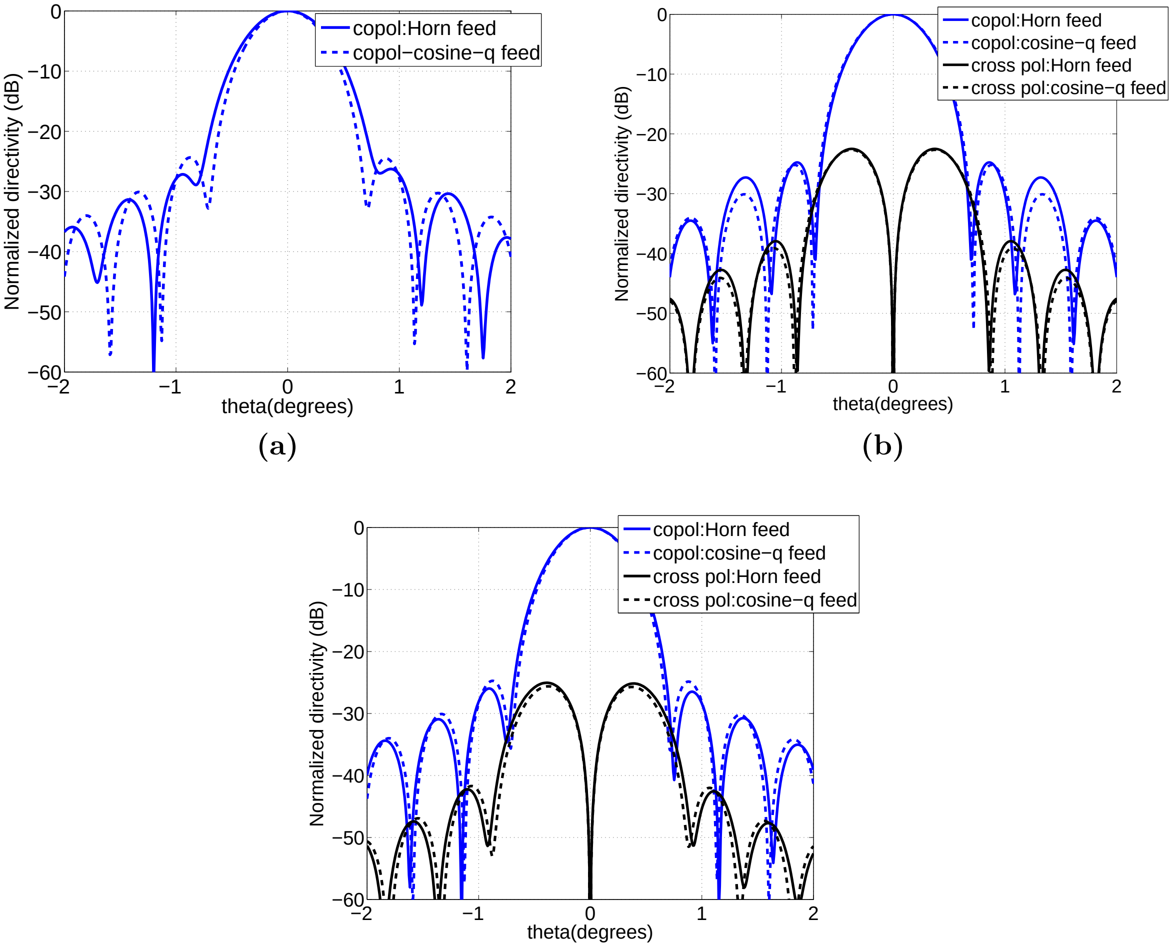

(a) **(b)**

(c)

Figure 6.12: Reflector antenna far field patterns with both the sidelobes and the cross polarization suppressed. (a) E-plane. (b) H-plane. (c) D-plane.

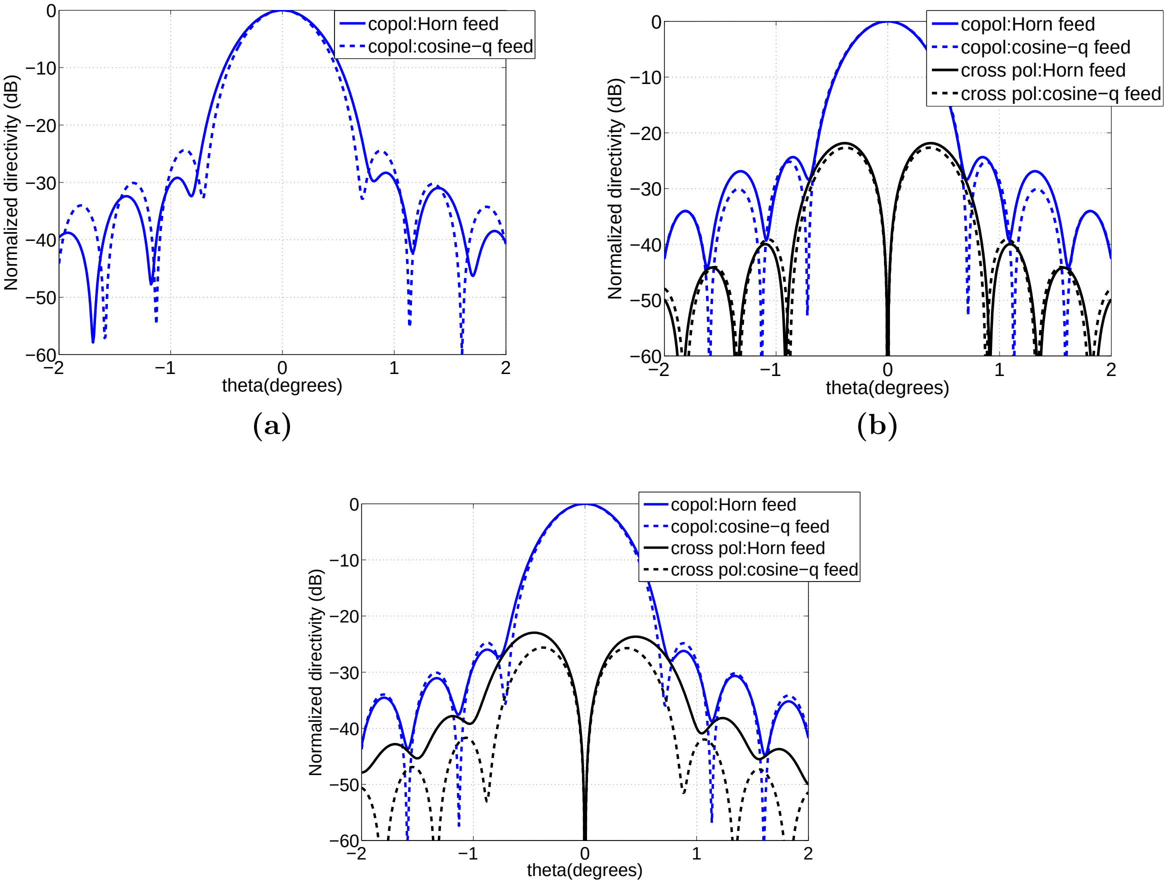

(a) **(b)**

(c)

Figure 6.13: Reflector antenna far field patterns with the cross pol of the feed forced to zero. (a) E-plane. (b) H-plane. (c) D-plane.

Table 6.2: Comparison of peak directivities (dB) between the cosine-q feed model and horn patterns for various cases as descibed in section 6.5.1-6.5.4.

Cosine-q feed		50.50
Horn feed	Original	50.00
	No cross pol	50.16
	No backlobes	50.08
	No sidelobes (with cross pol)	50.46
	No sidelobes (without xpol)	50.49

to develop an efficient feed design, which will be an area of future research.

CHAPTER 7

CAD Reflector Antenna Analysis

With seamless integration between electromagnetic simulation packages and CAD softwares, EM analysis of complex mechanical structures have become a reality. In this chapter, a CAD model of the prospective 1m offset single reflector design will be analyzed using PO. The work presented in this chapter is the result of our collaboration with mechanical engineers at *Tendeg LLC* who have been instrumental in designing the CAD model for the reflector antenna configuration.

7.1 Description of CAD file

One of the common CAD file formats is the Standard for the Exchange of Product (STEP) Data. Such CAD file formats typically contain information about the tetrahedrons that make up the three dimensional object. It is possible to treat every tetrahedron individually for EM analysis or unite all the tetrahedrons in the CAD software itself so that the EM software sees the geometry as a single unit. Typically, the latter is computationally less expensive and thus, this section analyses the latter format of the CAD file.

The imported CAD file is shown in Fig. 7.1. It can be observed that the reflector surface is now made of discrete planar triangles. Thus, the CAD model satisfies the equation of the paraboloid only at discrete points, which in this case is the nodes of the triangle. The deviation of the model from the true paraboloid is maximum at the center of each triangle. The projected aperture of the reflector is shown in Fig. 7.2. The table embedded in Fig. 7.2 shows the deviation of the CAD surface at the center of particular triangular patches in the

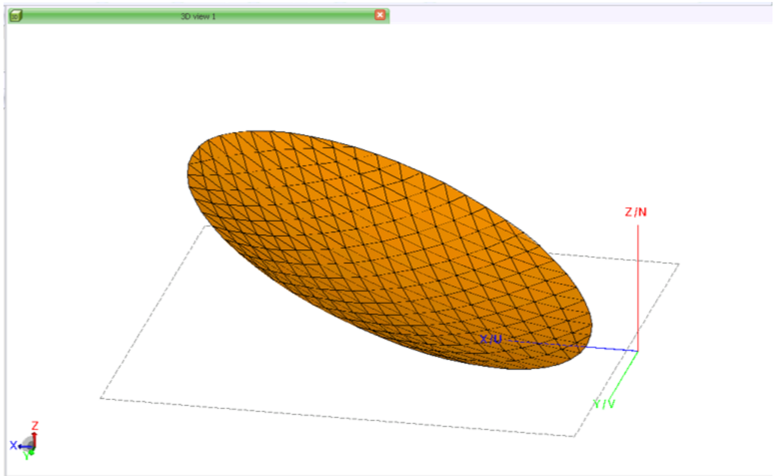

Figure 7.1: CAD model of reflector surface imported into FEKO.

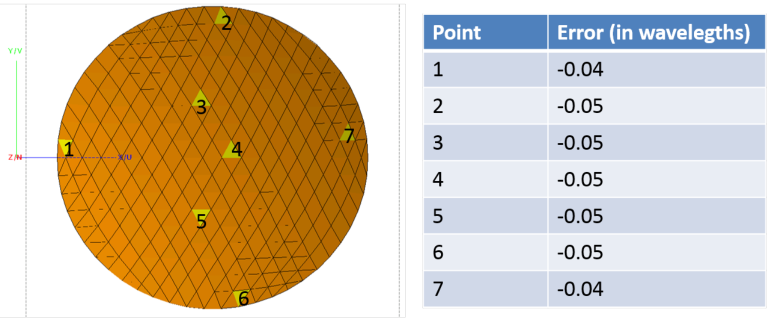

Point	Error (in wavelegths)
1	-0.04
2	-0.05
3	-0.05
4	-0.05
5	-0.05
6	-0.05
7	-0.04

Figure 7.2: Projected aperture of the CAD model. The surface deviation of the CAD model is measured at the centers of representative triangular patches. The origin of the cooedinate system is at the vertex of the paraboloid as shown in Fig. 7.1.

CAD model. For this particular model, the maximum deviation is of the order of $\lambda/20$ with the separation between two nodes being about 8λ. As will be discussed in the subsequent sections, these deviations cause periodic variations in the aperture distributions, resulting in a slight degradation of performance.

7.2 CAD model vs. Ideal reflector

This section compares the electromagnetic performance of the CAD model with the 'ideal reflector'. Ideal reflector, in this case, refers to a true paraboloid, which is not discretized into triangular patches. The cosine-q feed model is used to feed both the reflector models (CAD and ideal). The feed taper is chosen to be -10dB, resulting in $q_1 = q_2 = 6.976$. The aperture distributions as well as the far field patterns are discussed.

7.2.1 Aperture distributions

Amplitude and phase distributions at the exit aperture of the CAD reflector model and the ideal reflector model are compared in Fig. 7.3. The effect of discretization is immediately evident: The deviation of the triangular patches from the true surface of the paraboloid gets translated to ripples in the amplitude and phase patterns. This is more clearly seen in the line cuts presented in Fig. 7.4. These periodic amplitude and phase ripples could potentially cause grating lobes at wide angular regions in the far field and cause nulls to be filled in, causing some loss in directivity.

7.2.2 Far field comparison

It was discussed in the previous section that the deviation of the CAD model from a true paraboloid introduce periodic ripples, that could potentially introduce grating lobes in the far field. A rough estimate of the position of the grating lobe θ_g can be obtained through (7.1), where d represents the spacing between two adjacent elements. Since the nodes of the triangle are spaced about 8λ apart, the position of the grating lobe evaluates as 7.18°.

$$\sin\theta_g = \frac{\lambda}{d} \tag{7.1}$$

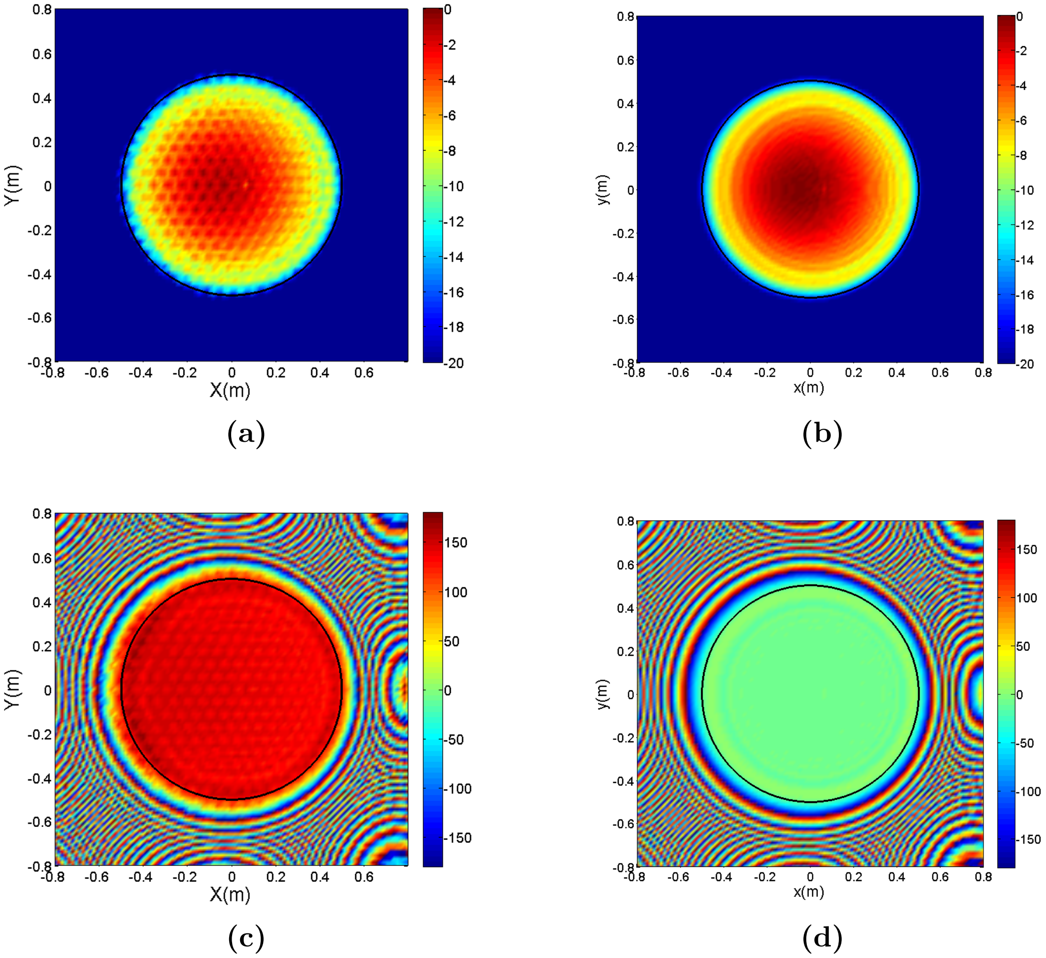

(a) **(b)**

(c) **(d)**

Figure 7.3: Comparisons between the amplitude and phase distributions at the exit aperture. (a) Normalized amplitude distribution in dB of CAD model. (b) Normalized amplitude in dB of ideal model. (c) Phase distribution of CAD model. (d) Phase distribution of ideal model.

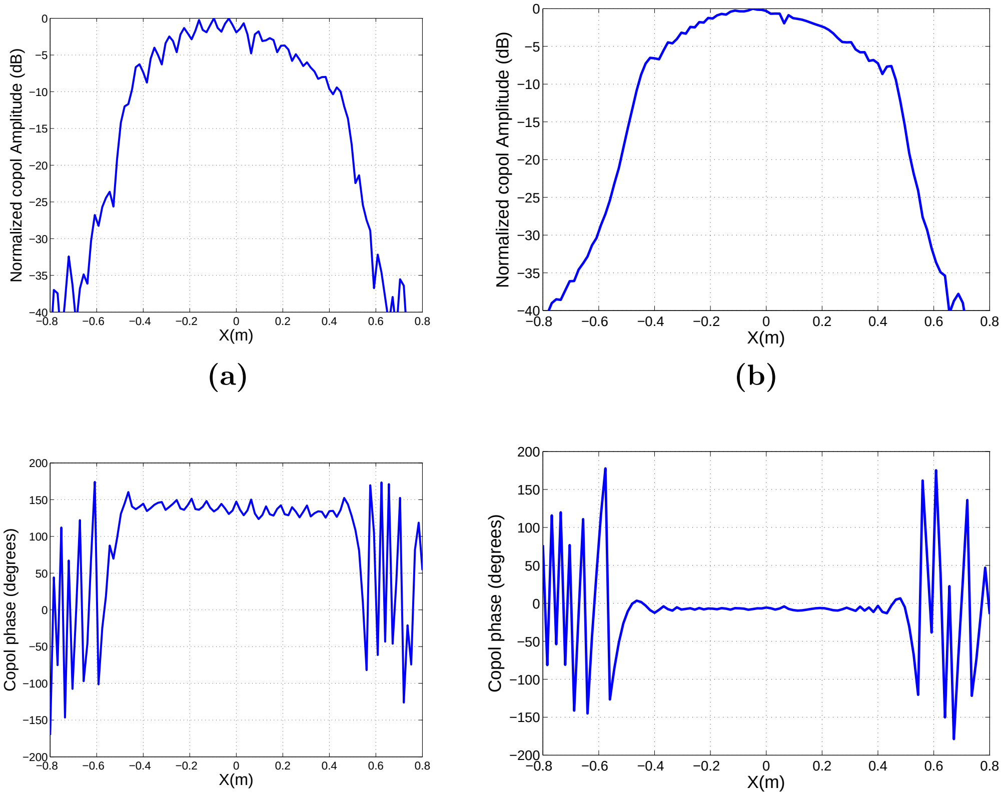

(a) **(b)**

(c) **(d)**

Figure 7.4: Line cuts of amplitude and phase distributions at the exit aperture. (a) Amplitude of CAD model. (b) Amplitude of ideal model. (c) Phase of CAD model (d) Phase of ideal model.

The far fields of the CAD and ideal reflector model is compared is Fig. 7.5. Grating lobes can be seen in both the E-plane and H-plane, though the level of the grating lobe is much higher in the H-plane. The location of the grating lobe agrees well with the prediction from (7.1). An interesting question here is the cause behind the grating lobe being more pronounced in the H-plane than the E-plane. A potential reason for this is the fact that the offset reflector has an elliptical rim, implying that the number of triangles along the E-plane is greater than the H-plane for the same projected aperture diameter. This in turn implies that the net deviation of the CAD model along the E-plane is lesser than along the H-plane, causing an increased grating lobe level. Fig. 7.6 shows a magnified version of the far field patterns o the CAD model and the ideal reflector surface. It is evident that the far field patterns for both are almost identical for observation angles near boresight. The loss in directivity 0.1dB. However, it must be noted that the aperture phase variations cause the maxima of the beam to occur at $\theta = 0.03°$ for the CAD model. This may be a concern for some advanced space applications where the position of the beam maxima is critical.

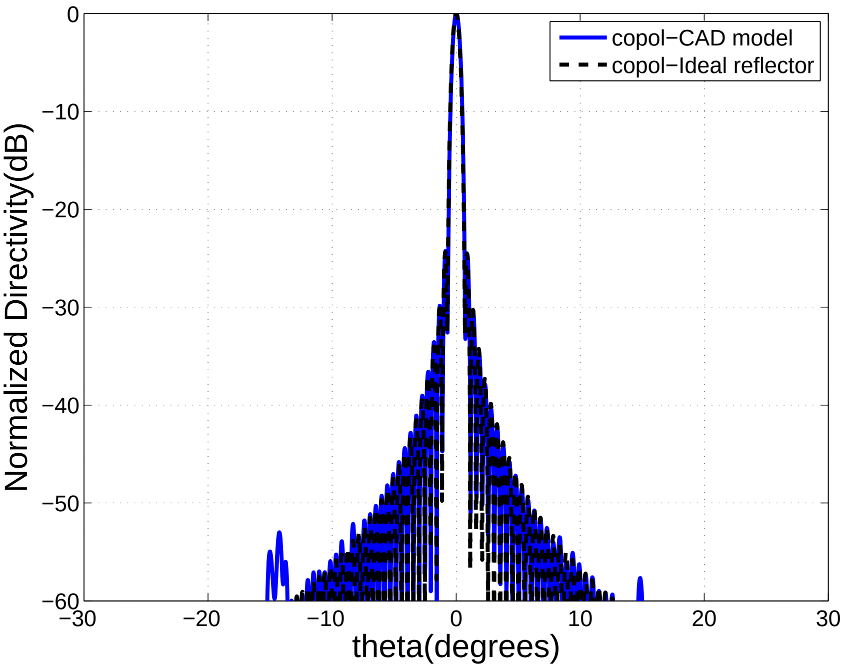

(a)

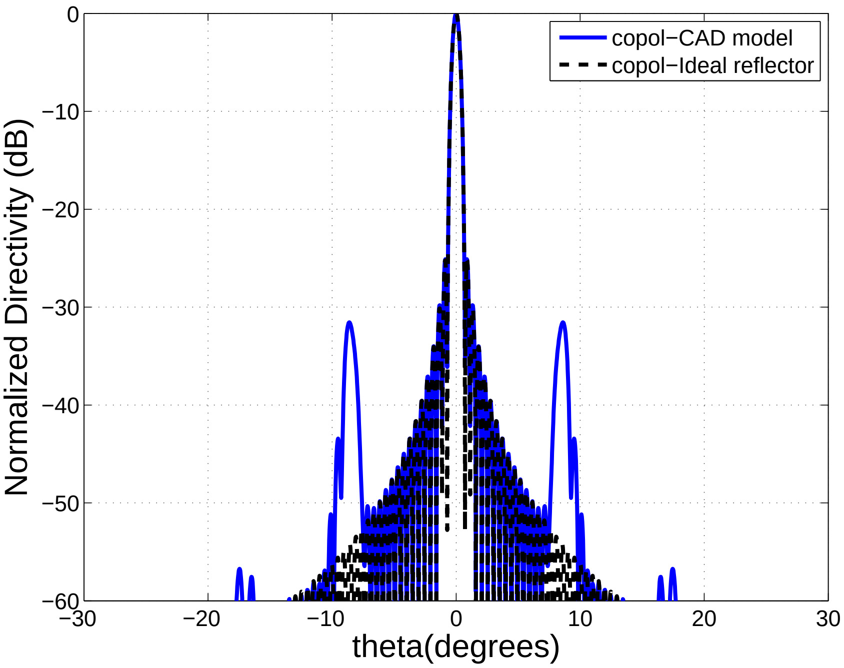

(b)

Figure 7.5: Comparisons between the far field patterns (copolarized component) of CAD model and the ideal reflector model (a) E-plane cut. (b) H-plane cut.

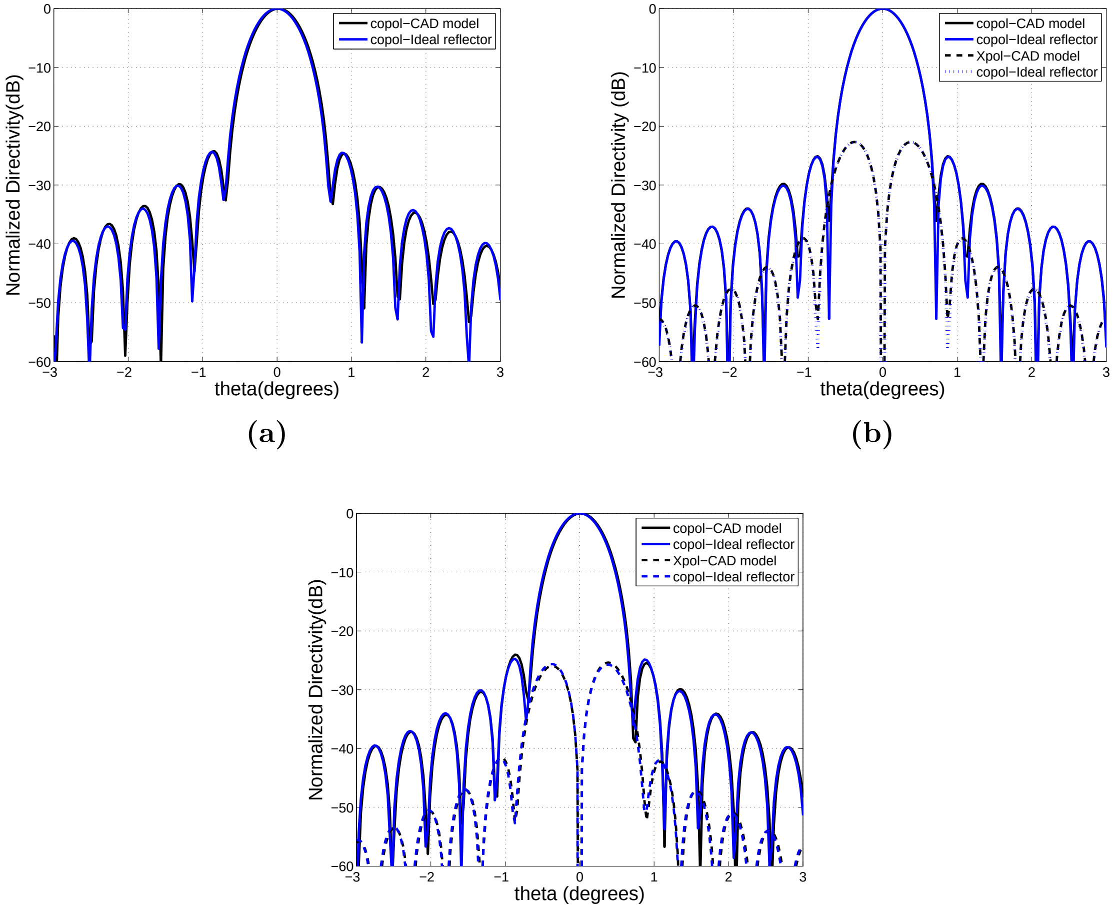

(a) **(b)**

(c)

Figure 7.6: Comparison Far field patterns near boresight between CAD model and the ideal reflector model. (a) E-plane cut. (b) H-plane cut. (c) D-plane cut.

CHAPTER 8

Conclusions and Future Work

As CubeSats show potential for advanced missions requiring higher data rates and fine resolution, developing antenna systems that can support these applications has become an emerging research area. The aim of this thesis was to investigate the potential of integrating a 1 meter offset mesh deployable reflector antenna with a 2.5U CubeSat chassis for Ka band remote sensing. The mechanical constraints of the CubeSat makes achieving the desired RF performance while satisfying packaging demands a major challenge. The focus of this work was to characterize efficiencies critical to deployable reflector to estimate the tradeoffs one encounters while balancing electromagnetic and the mechanical constraints. Chapter 3 analyzed umbrella reflectors in detail with the aim to characterize the gain loss due to the deviation of the umbrella reflector surface from an ideal paraboloid. Chapter 4 presented several design curves that relate the mesh geometry to the transmission loss that one can expect for mesh reflectors. The aperture efficiency was studied in detail in Chapter 6 to highlight aspects of the feed horn critical to the reflector performance. For each study, efficiency curves and numerical results were presented to aid the design of an optimal reflector antenna system.

While this work focused particularly on the reflector design, the feed design is an integral part of the system and it is critical that it optimally illuminates the reflector while occupying minimal space within the CubeSat. For pyramidal or conical horns, the length is limited by the quadratic phase error at its aperture. Special techniques must be used to achieve desired performance when horn length is a major constraint. Potter horns use a stepped profile to create a dual-mode distribution to provide low cross polarization at the cost of reduced bandwidth and complexity of prototyping. Corrugated horns are also capable of providing low sidelobes and cross polarization, but are expensive to fabricate and are typically heavier. Thus, optimization techniques must be used in order to develop a horn that strikes a balance between the ease of fabrication, desired radiation characteristics and overall volume. This feed design will be a major area of future work.

Advancements in computational technology have enabled seamless integration of mechanical CAD models with EM simulation tools to enable thorough RF analysis. In this work, an insight into CAD model analysis of reflectors was presented. The CAD model of the reflector surface was imported into the PO solver for RF characterization. These capabilities facilitate accurate simulation of geometries with intricate features (like complex mesh knits, CubeSat chassis, etc.), giving engineers more power to develop and test innovative designs.

The studies conducted in this thesis not only demonstrate the feasibility of the next high-gain antenna; they mark a major milestone (a 1m antenna size) for CubeSats, which is among the largest to be utilized for Ka band.

APPENDIX A

Derivation of F_{opt} and RMS Error via the Best Fit Approach

This appendix details the derivation of the optimal focal point and the corresponding RMS error for the best fit paraboloid approach outlined in Section 3.2.3. The steps were outlined in [55]. For completeness, the details are shown in this section.

The equation for the umbrella reflector can be expressed as:

$$z_g = \frac{x^2 + y^2}{4F_g} \tag{A.1}$$

where,

$$F_g = F_r \frac{\cos^2 \frac{\pi}{N_g}}{\cos^2(\frac{\phi_m + \phi_{m+1} - 2\phi}{2})} \tag{A.2}$$

where $\phi_m = \frac{2\pi m}{N_g}$ and $m = 0, 1, 2..N_g - 1$.

Due to symmetry, it suffices to compute the RMS error over just half of one gore surface. Since any gore can be chosen, we can make an arbitrary choice of $m = 0$ to get the equation of the first gore. Thus, the equation for one gore surface can be written as:

$$F_g = F_r \frac{\cos^2 \frac{\pi}{N_g}}{\cos^2(\frac{\pi}{N_g} - \phi)} \tag{A.3}$$

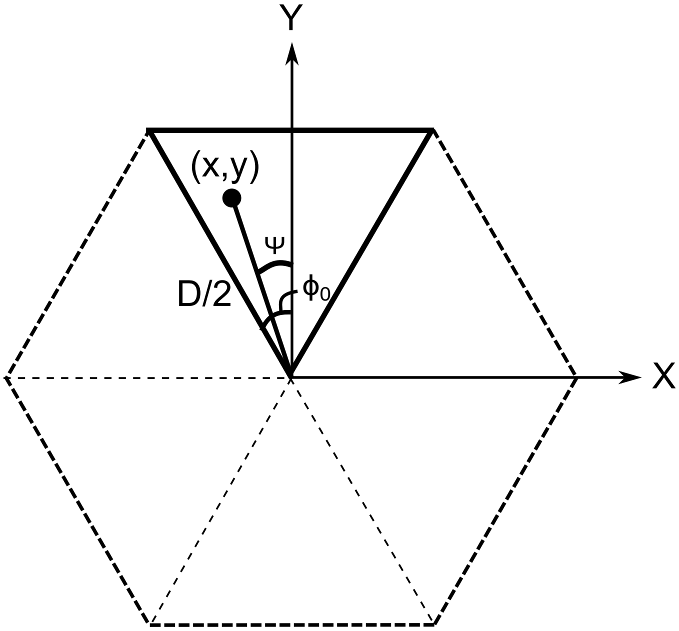

Figure A.1: Projection of the gore surface in XY plane showing the parameters ψ and $\phi_\circ$ as defined by (A.4) and (A.5).

For convenience, we introduce the following notations:

$$\psi = \frac{\pi}{N_g} - \phi \tag{A.4}$$

$$\phi_\circ = \pi/N_g \tag{A.5}$$

Thus,

$$F_g = F_r \frac{\cos^2 \frac{\pi}{N_g}}{\cos^2 \psi} \tag{A.6}$$

Now, the equivalent paraboloid of focal length F_{eq} can be expressed as:

$$z_{eq} = \frac{x^2 + y^2}{4F_{eq}} \tag{A.7}$$

The value of F_{eq} that minimizes the RMS error between z_g and z_{eq} would then be the optimal focal point for the umbrella reflector. The RMS error can be found using the equation:

$$\Delta z_{rms}^2 = \frac{1}{A_g} \iint (z_g - z_{eq})^2 dS \tag{A.8}$$

Where A_g is the area over which the RMS error is computed. By symmetry, the RMS error can be found by evaluating the error over just half a gore surface. Referring to Fig. A.1, the RMS between the gore surface and equivalent paraboloid can be expressed as:

$$\Delta z_{rms}^2 = \frac{1}{A_g} \int_0^{\frac{D}{2}\cos\phi_\circ} \int_0^{y\tan\phi_\circ} \left((x^2+y^2) \left[\frac{1}{F_{eq}} - \frac{1}{F_g} \right] \right)^2 dxdy \tag{A.9}$$

Substitution of (A.6) into (A.9) yields:

$$\Delta z_{rms}^2 = \frac{1}{A_g} \int_0^{\frac{D}{2}\cos\phi_\circ} \int_0^{y\tan\phi_\circ} \left((x^2+y^2) \left[\frac{1}{F_{eq}} - \frac{\cos^2\psi}{F_r\cos^2\phi_\circ} \right] \right)^2 dxdy \tag{A.10}$$

Where A_g is the area of half gore surface given by

$$A_g = \frac{1}{4} \left(\frac{D}{2} \right)^2 \sin(2\phi_\circ) \tag{A.11}$$

From Fig. A.1, it is evident that $\cos^2\psi = \frac{y^2}{x^2+y^2}$. With these subsitutions, (A.10) can be expressed as:

$$\Delta z_{rms}^2 = I_1 + I_2 + I_3 \qquad where \tag{A.12}$$

$$I_1 = \frac{1}{16A_g} \int_0^{\frac{D}{2}\cos\phi_\circ} \int_0^{y\tan\phi_\circ} \frac{(x^2+y^2)^2}{F_{eq}^2} dxdy \tag{A.13}$$

$$I_2 = \frac{1}{16A_g} \frac{2}{F_{eq}} \frac{1}{F_r\cos^2\phi_\circ} \int_0^{\frac{D}{2}\cos\phi_\circ} \int_0^{y\tan\phi_\circ} (x^2+y^2)^2 \frac{y^2}{y^2+x^2} dxdy \tag{A.14}$$

$$I_3 = \frac{1}{16A_g} \int_0^{\frac{D}{2}\cos\phi_\circ} \int_0^{y\tan\phi_\circ} \frac{(x^2+y^2)^2}{F_r^2\cos^2\phi_\circ} \frac{y^4}{(x^2+y^2)^2} dxdy \tag{A.15}$$

I_1, I_2 and I_3 can be readily solved by expanding the squares and integrating each term individually. The final results is shown below:

$$\Delta z_{rms}^2 = \frac{(D\cos\phi_\circ)^4}{768}\left[\frac{1}{F_{eq}^2}T_1 - \frac{1}{F_r\cos^2\phi_\circ}\frac{2}{F_{eq}}T_2 + \frac{1}{F_r^2}\frac{1}{\cos^4\phi_\circ}\right] \tag{A.16}$$

where,

$$T_1 = 1 + \frac{2}{3}\tan^2\phi_\circ + \frac{1}{5}\tan^4\phi_\circ \tag{A.17}$$

$$T_2 = 1 + \frac{1}{3}\tan^2\phi_\circ \tag{A.18}$$

Now, it is desired to find the optimal focal length, which is the value of F_{eq} that minimizes the RMS error given by (A.16). Thus,

$$\left.\frac{\partial\Delta z_{rms}^2}{\partial F_{eq}}\right|_{F_{eq}=F_{opt}} = 0 \tag{A.19}$$

This leads to

$$-\frac{2}{F_{opt}^3}T_1 + \frac{2}{F_rF_{opt}^2}\frac{1}{\cos^2\phi_\circ}T_2 = 0 \tag{A.20}$$

On substituting values of T_1 and T_2 from (A.17) and (A.18) respectively, we get the expression for the optimal focal length as:

$$\frac{F_{opt}}{F_r} = \cos^2\phi_\circ\frac{1 + \frac{2}{3}\tan^2\phi_\circ + \frac{1}{5}\tan^4\phi_\circ}{1 + \frac{1}{3}\tan^2\phi_\circ} \tag{A.21}$$

The corresponding RMS error can be got by substituting (A.21) in (A.16):

$$\Delta z_{rms}|_{F_{eq}=F_{opt}} = 0.010758\frac{D^2\cos^2\phi_\circ}{F_r}\frac{\tan^2\phi_\circ(1+\tan^2\phi_\circ)}{\sqrt{(1+\frac{2}{3}\tan^2\phi_\circ+\frac{1}{5}\tan^4\phi_\circ)}} \tag{A.22}$$

APPENDIX B

Weighted RMS Error for Aperture Antennas

In order to get an initial idea of the gain loss due to the deviation of a surface from an ideal paraboloid (which happens in the case of umbrella reflectors), it is convenient to define an RMS error that quantifies the difference between the two surfaces. This analysis was detailed in [57] and is repeated here for convenience. The gain loss is related to the RMS error through Ruze's formula given as [56]:

$$\Delta G(dB) = -685.811 \left(\frac{k \Delta z_{rms}}{\lambda} \right)^2 \tag{B.1}$$

where $k = (4F/D)\sqrt{\ln[1 + 1/(4F/D)^2]}$. Thus, if the RMS error is known, the gain loss due to the deviation can be easily predicted.

Often, the amplitude distribution at the aperture of a reflector antenna is tapered to provide the optimal aperture efficiency. The taper, intuitively, must reduce the RMS error since the deviation at the edges become less significant. Further, the effective area over which the RMS is calculated also reduces. This appendix outlines the derivation of this weighted RMS when the reflector aperture is given an amplitude taper.

In general, the gain of an aperture antenna at broadside ($\theta = 0°$) can be expressed as:

$$G = \frac{4\pi}{\lambda^2} \frac{|\iint E_a ds|^2}{\iint |E_a|^2 ds} \tag{B.2}$$

Where E_a denotes the aperture field distribution. If the aperture distribution is denoted as $E_a = f(\rho, \phi) e^{j\Delta}$, the gain can be expressed as:

$$G_0 = \frac{4\pi}{\lambda^2} \frac{|\iint f(\rho,\phi)e^{j\Delta}ds|^2}{\iint |f(\rho,\phi)e^{j\Delta}|^2 ds} \tag{B.3}$$

Note that (ρ, ϕ) denote the reflector aperture coordinates. For an ideal reflector, the aperture should ideally have constant phase. Thus, Δ can be assumed constant and can be pulled out of integration, leading to

$$G_0 = \frac{4\pi}{\lambda^2} \frac{|\iint f(\rho,\phi)ds|^2}{\iint |f(\rho,\phi)|^2 ds} \tag{B.4}$$

Now, for the case of an arbitrarily shaped surface, the phase at the aperture will not be a constant. It will, in fact, be a function of (ρ, ϕ). This phase deviation is denoted by $\xi(\rho, \phi)$. Assuming that the amplitude distribution remains approximately the same, the expression for broadside gain can for this surface can be written as:

$$G = \frac{4\pi}{\lambda^2} \frac{|\iint f(\rho,\phi)e^{j\xi}ds|^2}{\iint |f(\rho,\phi)|^2 ds} \tag{B.5}$$

From B.4 and B.5.

$$\frac{G}{G_0} = \frac{|\iint f(\rho,\phi)e^{j\xi}ds|^2}{|\iint f(\rho,\phi)ds|^2} \tag{B.6}$$

The phase term can now be expanded in taylor's series as:

$$e^{j\xi} \approx 1 + (j\xi) - \frac{\xi^2}{2} \tag{B.7}$$

Substituting in B.5,

$$\frac{G}{G_0} = \left| \frac{\iint f(\rho,\phi)\left[1 + (j\xi) - \frac{\xi^2}{2}\right] ds}{\iint f(\rho,\phi)ds} \right|^2 \tag{B.8}$$

$$\frac{G}{G_0} = \left| 1 + j\bar{\xi} - \frac{1}{2}\bar{\xi^2} \right|^2 \tag{B.9}$$

Where

$$\bar{\xi} = \frac{\iint \xi f(\rho,\phi)ds}{\iint f(\rho,\phi)ds} \tag{B.10}$$

$$\bar{\xi^2} = \frac{\iint \xi^2 f(\rho, \phi) ds}{\iint f(\rho, \phi) ds} \tag{B.11}$$

The expression for G/G_0 can further be simplified as:

$$\frac{G}{G_0} = \left(1 - \frac{1}{2}\bar{\xi^2}\right)^2 + \left(\bar{\xi}\right)^2 \tag{B.12}$$

Which simplifies to

$$\frac{G}{G_0} = 1 + \frac{\bar{\xi^2}^2}{4} - \bar{\xi^2} + (\bar{\xi})^2 \tag{B.13}$$

neglecting the $\bar{\xi^2}^2$, which is valid when the mean phase error is not significant, one arrives at

$$\frac{G}{G_0} = 1 - (\bar{\xi^2} - (\bar{\xi})^2) \tag{B.14}$$

The gain loss δ due to a phase deviation ξ is thus

$$\bar{\delta^2} = \bar{\xi^2} - (\bar{\xi})^2 \tag{B.15}$$

Now, for gore reflectors, the mean phase error can be approximated as:

$$\xi = \frac{4\pi}{\lambda}(z_g - z_{eq}) \tag{B.16}$$

Where, the $4\pi/\lambda$ factor accounts for the ray path. Note that for simplicity, only the error in the axial direction is considered. Thus, the gain loss due to gore surface can be expressed as:

$$\bar{\delta^2} = \left(\frac{4\pi}{\lambda}\right)^2 \frac{1}{\iint f(\rho, \phi) ds} \left[\iint (z_g - z_{eq})^2 f(\rho, \phi) ds\right] - \left[\frac{\iint (z_g - z_{eq}) f(\rho, \phi) ds}{\iint f(\rho, \phi) ds}\right]^2 \tag{B.17}$$

This function must be minimized in order to get the best fit paraboloid z_{eq}. The focal length that corresponds to the minimum RMS error is called the optimum focal point F_{opt}. It is intuitive that the best fit paraboloid would minimize the mean error between the equivalent paraboloid and the gored reflector. Further, the RMS error contains the square of the mean, which is an even smaller number. Thus, the second term can be neglected. Thus,

$$\bar{\delta}^2 = \left(\frac{4\pi}{\lambda}\right)^2 \frac{1}{\iint f(\rho,\phi)ds}\left[\iint (z_g - z_{opt})^2 f(\rho,\phi)ds\right] = \left(\frac{4\pi}{\lambda}\right)^2 \Delta z_{rms}^2 \tag{B.18}$$

It is straightforward to see that for the case of uniform illumination ($f(\rho,\phi) = 1$), the formula recovers the original definition of the RMS error between the two surfaces. Thus B.18 can then be used to give the required RMS error between the umbrella reflector and the gored reflector, to get estimates of the gain loss from Ruze's equation.

APPENDIX C

Scattering from PEC Cylinder

Studying the canonical problem of scattering of TEM plane wave from an infinite cylinder can give some insights to the behavior of complex mesh surfaces. The orientation of the electric field is assumed to be parallel to the wires (TM^z). The geometry is shown in Fig. C.1. The incident wave equations can be written as:

$$\vec{E_i} = E_0[\cos\theta_i\hat{x} + \sin\theta_i\hat{z}]e^{-j\beta(x\sin\theta_i - z\cos\theta_i)} \tag{C.1}$$

Using the relation

$$e^{-j\beta x\sin\theta_i} = \sum_{n=-\infty}^{\infty} J_n(\beta\rho\sin\theta_i)e^{jn\phi} \tag{C.2}$$

The incident electric field equation can be expressed in cylindrical coordinate system as:

$$E^i_\rho = E_0\cos\theta_i\cos\phi e^{j\beta z\cos\theta_i}\sum_{n=-\infty}^{\infty} J_n(\beta\rho\sin\theta_i)e^{jn\phi} \tag{C.3}$$

$$E^i_\phi = -E_0\cos\theta_i\sin\phi e^{j\beta z\cos\theta_i}\sum_{n=-\infty}^{\infty} J_n(\beta\rho\sin\theta_i)e^{jn\phi} \tag{C.4}$$

$$E^i_z = -E_0\sin\theta_i e^{j\beta z\cos\theta_i}\sum_{n=-\infty}^{\infty} J_n(\beta\rho\sin\theta_i)e^{jn\phi} \tag{C.5}$$

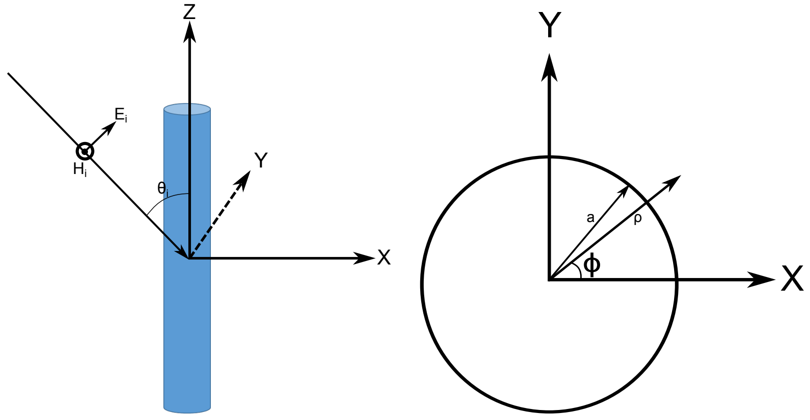

(a) **(b)**

Figure C.1: TM^z scattering from infinite cylinder. (a)Geometry in XZ plane and (b) geometry in XY plane.

Similarly, the equations for the magnetic field can be written as:

$$H_\rho^i = -\frac{E_0}{\eta} \sin\phi e^{j\beta z \cos\theta_i} \sum_{n=-\infty}^{\infty} J_n(\beta\rho\sin\theta_i) e^{jn\phi} \tag{C.6}$$

$$H_\phi^i = -\frac{E_0}{\eta} \cos\phi e^{j\beta z \cos\theta_i} \sum_{n=-\infty}^{\infty} J_n(\beta\rho\sin\theta_i) e^{jn\phi} \tag{C.7}$$

$$H_z^i = 0 \tag{C.8}$$

The scattered fields can be constructed as:

$$E_\rho^s = jE_0 cos\theta_i e^(j\beta z\cos\theta_i) \sum_{n=-\infty}^{\infty} j^{-n} a_n H_n^{(2)'}(\beta\rho\sin\theta_i) e^{jn\phi} \tag{C.9}$$

$$E_\phi^s = jE_0 \left(\frac{\cot\theta_i}{\beta\rho}\right) e^{j\beta z\cos\theta_i} \sum_{n=-\infty}^{\infty} n j^{-n+1} a_n H_n^{(2)}(\beta\rho\sin\theta_i) e^{jn\phi} \tag{C.10}$$

$$E_z^s = E_0 \sin\theta_i e^{j\beta z cos\theta_i} \sum_{n=-\infty}^{\infty} j^{-n} a_n H_n^{(2)}(\beta\rho\sin\theta_i) e^{jn\phi} \tag{C.11}$$

$$H_\rho^s = \frac{jE_0}{\omega\mu\rho\sin\theta_i} e^{j\beta z cos\theta_i} \sum_{n=-\infty}^{\infty} n j^{-n+1} a_n H_n^{(2)}(\beta\rho\sin\theta_i) e^{jn\phi} \tag{C.12}$$

$$H_\phi^s = -\frac{jE_0}{\eta} e^{(}j\beta z\cos\theta_i) \sum_{n=-\infty}^{\infty} j^{-n} a_n H_n^{(2)'}(\beta\rho\sin\theta_i) e^{jn\phi} \tag{C.13}$$

where

$$a_n = -\frac{J_n(\beta a\sin\theta_i)}{H_n^{(2)}(\beta a\sin\theta_i)} \tag{C.14}$$

The total current induced on the surface can be computed as $\vec{J} = \hat{n} \times (\vec{H}_i + \vec{H}_s)\Big|_{\rho=a}$ This results in

$$\vec{J} = -\frac{jE_0}{\eta} e^{j\beta z\cos\theta_i} \sum_{n=-\infty}^{\infty} \frac{j^{-n} J_n(\beta a\sin\theta_i)}{H_n^{(2)}} \left[\frac{\cos\phi}{j} H_n^{(2)}(\beta a sin\theta_i) - H_n^{(2)}(\beta\rho\sin\theta_i)\right] e^{jn\phi} \tag{C.15}$$

Now, for cases where ($a\sin\theta_i \ll \lambda$), only the $n = 0$ term dominates. Using the small argument values of the Hankel functions, the current can be approximated as:

$$H_0^{(2)'}(\beta a\sin theta_i) \approx -j\frac{2}{\pi\beta a\sin\theta_i} \tag{C.16}$$

$$H_0^{(2)}(\beta a\sin theta_i) \approx -j\frac{2}{\pi}\ln(0.8905\beta a\sin\theta_i) \tag{C.17}$$

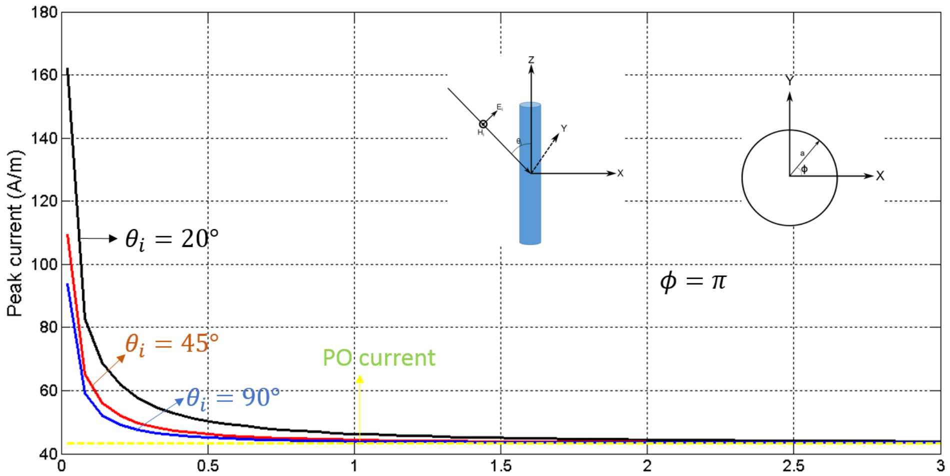

Figure C.2: Variation of peak current induced on the cylinder for various angles as function of a/λ. Note that the currents begin to get singular as $a \sin\theta \to 0$.

$$J \approx \frac{jE_0}{\eta} e^{j\beta z \cos\theta_i} \frac{1}{a\beta \sin\theta_i} \frac{1}{\ln(0.89 a\beta \sin\theta_i)} \tag{C.18}$$

The variation of peak currents as a function of radius can be seen is Fig. (C.2). A significant observation here is that the current density tends to become singular as $\beta a \sin\theta_i \to 0$. This can happen in two scenarios: The radius of the wires being much lesser than the wavelength or the angle of incidence $\theta_i \to 0$. The latter case presents an interesting phenomenon. It implies that as the angle of incidence θ_i increases, the effective radius of the wire decreases, causing greater induced currents.

For mesh surfaces, it is only intuitive to expect that the openings also get scaled by $\sin\theta_i$, and could be the reason for the reflection coefficients tending towards unity for very oblique incidences, as predicted by the Astrakhan's formulation.

APPENDIX D

Radiation from Uniformly Illuminated Elliptical Apertures

Assume that an elliptical aperture is illuminated by a plane wave polarized in X direction, with reference to Fig. D.1.

The incident wave equations can be written as:

$$\vec{E}_i = E_0 e^{j\beta z} \hat{x} \tag{D.1}$$

$$\vec{H}_i = \frac{E_0}{\eta} e^{j\beta z} \hat{y} \tag{D.2}$$

Assuming the aperture lies in $z = 0$ plane, the field on the disc can be written as:

$$\vec{E}_i = E_0 \hat{x} \tag{D.3}$$

$$\vec{H}_i = \frac{E_0}{\eta} \hat{y} \tag{D.4}$$

For reflector applications, the aperture dimensions are usually much greater than the wavelength, making Physical Optics a valid approximation.

$$\vec{J}_{po} = 2\hat{n} \times \vec{H}_i \tag{D.5}$$

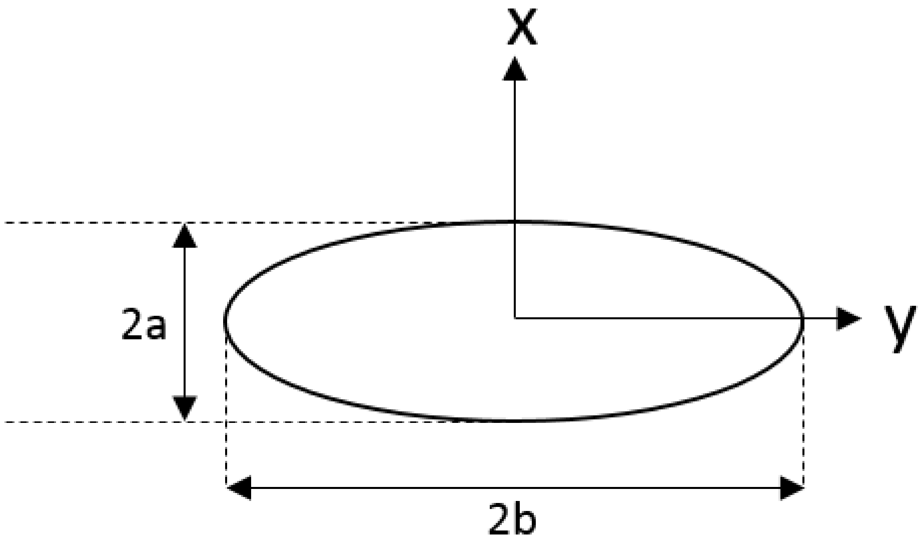

Figure D.1: An elliptical aperture illuminated by a plane wave normally incident, linearly polarized in X direction.

with $\hat{n} = \hat{z}$, (D.5) yields

$$\vec{J}_{po} = \frac{2E_0}{\eta}\hat{x} \tag{D.6}$$

Using, (D.6), the magnetic vector potential can be written as

$$\vec{A} = \frac{\mu}{4\pi}\frac{e^{-j\beta r}}{r}\iint_s \vec{J}_{po} e^{j\beta \vec{r'}.\hat{r}} ds \tag{D.7}$$

where r' denotes the coordinates of the radiating aperture and $\hat{r}$ denotes the far field observation direction.

$$\vec{r'}.\hat{r} = (a\rho' \cos\phi'\hat{x} + b\rho' \sin\phi'\hat{y}).(\sin\theta\cos\phi\hat{x} + sin\theta\sin\phi\hat{y}) \tag{D.8}$$

Which simplifies to

$$\vec{r'}.\hat{r} = a\rho' \cos\phi' \sin\theta \cos\phi + b\rho' \sin\phi' \sin\theta \sin\phi \tag{D.9}$$

The $x - directed$ current can be decomposed into its spherical components as:

$$J_\theta = J_x.\hat{\theta} = \frac{2E_0}{\eta} \cos\theta \cos\phi \tag{D.10}$$

$$J_\phi = J_x.\hat{\theta} = -\frac{2E_0}{\eta} \sin\phi \tag{D.11}$$

Substituting D.9, D.10 and D.11 in D.7 yields

$$A_\theta = \frac{\mu}{4\pi} \frac{e^{-j\beta r}}{r} N_\theta \tag{D.12}$$

$$A_\phi = \frac{\mu}{4\pi} \frac{e^{-j\beta r}}{r} N_\phi \tag{D.13}$$

Where,

$$N_\theta = \frac{4\pi E_0}{\eta} \cos\theta \cos\phi \frac{1}{\beta\sqrt{a^2 \sin^2\theta \cos^2\phi + b^2 \sin^2\theta \sin^2\phi}} J_1(\sqrt{a^2 \sin^2\theta \cos^2\phi + b^2 \sin^2\theta \sin^2\phi}) \tag{D.14}$$

$$N_\phi = -\frac{4\pi E_0}{\eta} \sin\phi \frac{1}{\beta\sqrt{a^2 \sin^2\theta \cos^2\phi + b^2 \sin^2\theta \sin^2\phi}} J_1(\sqrt{a^2 \sin^2\theta \cos^2\phi + b^2 \sin^2\theta \sin^2\phi}) \tag{D.15}$$

The far field electric fields can be constructed as:

$$E_\theta = -j\omega A_\theta \tag{D.16}$$

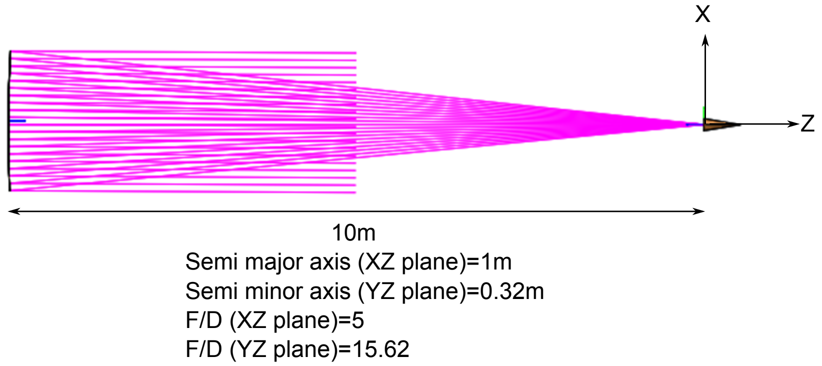

Figure D.2: A reflector antenna of large F/D to emulate plane wave normally incident on an elliptical aperture.

$$E_\phi = -j\omega A_\phi \tag{D.17}$$

With E_θ and E_ϕ known, the copol and crosspol components can be constructed from Ludwig's 3^{rd} definition [69] as:

$$E_{co} = \cos\phi E_\theta - \sin\phi E_\phi \tag{D.18}$$

$$E_{cross} = \sin\phi E_\theta + \cos\phi E_\phi \tag{D.19}$$

These expressions can be checked by simulating an elliptical aperture of a large F/D ratio. The geometry is shown in Fig. D.2. The comparison of the analytical results with the simulated results are shown in Fig. D.3.

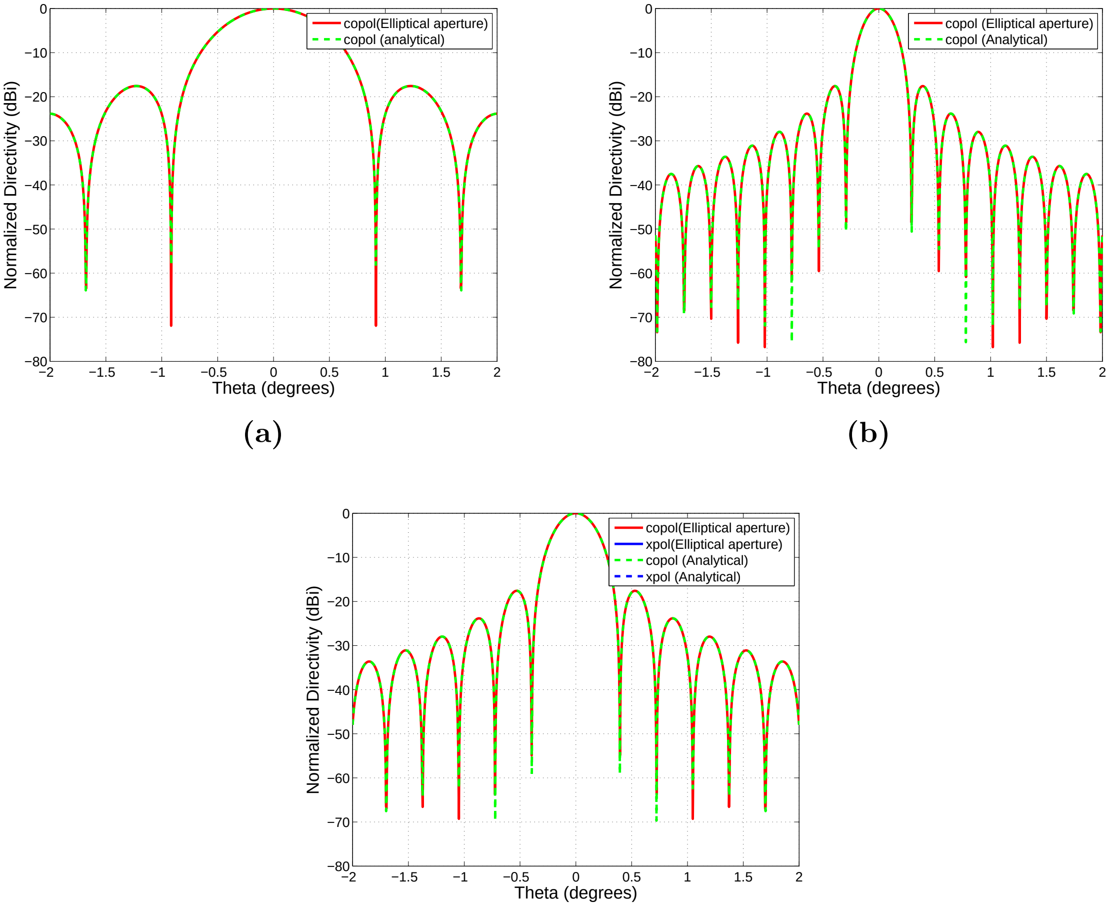

(a) **(b)**

(c)

Figure D.3: Comparison between the simulated results for a reflector antenna with an elliptical aperture of $F/D = 5$ in E-plane and $F/D = 15.62$ in H-plane with analytical formulation. (a)E-plane. (b) H-plane. (c)D-plane.

References

[1] M. A. Swartwout, "CubeSat Database." `https://sites.google.com/a/slu.edu/swartwout/home/cubesat-database`. Accessed April 10, 2016.

[2] S. Lee *et al.*, "CubeSat Design Specification," *The CubeSat Program*, vol. 8651, p. 22, 2009.

[3] ARC Mission Design Division Staff, "Small Spacecraft Technology State of the Art," Tech. Rep. NASA/TP–2014–216648/REV1, NASA Ames Research Center, Moffet Field, CA, 2014.

[4] M. Deshpande and J. Piepmeier, "Design and Development of VHF Antennas for Space Borne Signal of Opportunity Receivers for Cubesat Platforms," 2015.

[5] T. Sato, R. Mitsuhashi, and S. Satori, "Attitude Estimation of Nano-Satellite HIT-SAT Using Received Power Fluctuation by Radiation Pattern," in *IEEE International Symposium on Antennas and Propagation*, 2009.

[6] R. Lehmensiek, "Using the physical structure of a passive aerodynamic attitude-stabilization system as a multi-frequency antenna on nano-satellites," *IEEE Antennas and Propagation Magazine*, vol. 54, no. 3, pp. 39–49, 2012.

[7] T. J. Mizuno, J. D. Roque, B. T. Murakami, L. K. Yoneshige, G. S. Shiroma, R. Y. Miyamoto, and W. A. Shiroma, "Antennas for Distributed Nanosatellite Networks," in *IEEE/ACES International Conference on Wireless Communications and Applied Computational Electromagnetics*, pp. 606–609, 2005.

[8] E. S. Moghaddam, N. Aboutorabian, S. Amiri, S. Nikmehr, and P. Rezaei, "Design and Analysis of a Dualband Antenna for Small LEO Satellite Applications," in *International Conference on Computational Electromagnetics and Its Applications*, pp. 228–231, 2004.

[9] M. Nohmi, K. Oi, S. Takuma, and M. Ogawa, "Solar Paddle Antenna Mounted on Pico-Satellite" KUKAI" for Amateur Radio Communication," in *Second International Conference on Advances in Satellite and Space Communications*, pp. 31–36, 2010.

[10] J. Costantine, Y. Tawk, A. Ernest, and C. Christodoulou, "Deployable Antennas for CubeSat and Space communications," in *6th European Conference on Antennas and Propagation (EUCAP)*, pp. 837–840, 2012.

[11] P. Rezaei, "Design of Quadrifilar Helical Antenna for Use on Small Satellites," in *IEEE International Symposium on Antennas and Propagation*, vol. 3, pp. 2895–2898, 2004.

[12] P. Muri, O. Challa, and J. McNair, "Enhancing Small Satellite Communication Through Effective Antenna System Design," in *Military Communications Conference (MILCOM)*, pp. 347–352, 2010.

[13] G. Olson, S. Pellegrino, J. Costantine, and J. Banik, "Structural Architectures for a Deployable Wideband UHF antenna," in *Structural Dynamics and Materials Conference*, pp. 23–26, 2012.

[14] E. Pittella, S. Pisa, and A. Nascetti, "Design of an Antenna System for CubeSat Satellites," in *Proceedings of the 2nd IAA Conference on University Satellites Missions and CubeSat Winter Workshop*, 2013.

[15] M. T. Islam, M. Cho, M. Samsuzzaman, and S. Kibria, "Compact Antenna for Small Satellite Applications," *IEEE Antennas and Propagation Magazine*, vol. 57, no. 2, pp. 30–36, 2015.

[16] F. E. Tubbal, R. Raad, and K.-W. Chin, "A Survey and Study of Planar Antennas for Pico-Satellites," *IEEE Access*, vol. 3, pp. 2590–2612, 2015.

[17] R. Montaño, N. Neveu, S. Palacio, E. Martinez, D. R. Jackson, J. Chen, P. W. Fink, and R. S. Provence, "Development of low-profile antennas for cubesats," 2014.

[18] A. Budianu, A. Meijerink, M. J. Bentum, D. M. Smith, and A.-J. Boonstra, "Antenna Architecture of a Nano-Satellite for Radio Astronomy," in *IEEE Aerospace Conference*, pp. 1–10, 2014.

[19] G. F. Kurnia, B. S. Nugroho, and A. D. Prasetyo, "Planar Inverted-F Antenna (PIFA) Array With Circular Polarization for Nano Satellite Application," in *International Symposium on Antennas and Propagation (ISAP)*, pp. 431–432, 2014.

[20] G. Dassano and M. Orefice, "The PICPOT Satellite Antenna Systems," in *IEEE International Symposium on Antennas and Propagation*, pp. 3029–3032, 2007.

[21] J. Padilla, G. Rosati, A. Ivanov, F. Bongard, S. Vaccaro, and J. Mosig, "Multi-Functional Miniaturized Slot Antenna System for Small Satellites," in *European Conference on Antennas and Propagation*, pp. 2170–2174, 2011.

[22] J. Klein, J. Hawkins, and D. Thorsen, "Improving CubeSat Downlink Capacity with Active Phased Array Antennas," in *IEEE Aerospace Conference*, pp. 1–8, 2014.

[23] S. Tariq and R. Baktur, "Circularly Polarized UHF Up-and Downlink Antennas Integrated With CubeSat Solar Panels," in *IEEE International Symposium on Antennas and Propagation & USNC/URSI National Radio Science Meeting*, pp. 1424–1425, 2015.

[24] R. M. Rodriguez-Osorio and E. F. Ramirez, "A Hands-On Education Project: Antenna Design for Inter-CubeSat Communications," *IEEE Antennas and Propagation Magazine*, vol. 54, no. 5, pp. 211–224, 2012.

[25] L. M. Hilliard, J. Mead, R. Rincon, and P. H. Hildebrand, "Lightweight Linear Broadband Antennas Enabling Small UAV Wing Systems and Space Flight Nanosat Concept," in *IEEE International Geoscience and Remote Sensing Symposium*, vol. 5, pp. 3577–3580, 2004.

[26] E. Palantei, S. Syarif, B. Topalaguna, and Z. Ubaid, "Four Elements Array of Lungs Shape Patch Antenna for Nanosatellite Telemetry," in *IEEE International Symposium on Antennas and Propagation*, pp. 1808–1809, 2013.

[27] O. Ceylan, Y. Kurt, F. A. Tunc, H. B. Yagci, and A. R. Aslan, "Low Cost S Band Communication System Design for Nano Satellites," in *5th International Conference on Recent Advances in Space Technologies*, pp. 767–770, 2011.

[28] W. N. Saputra, B. Prasetya, and Y. Wahyu, "Design and Realization of two Array Triangle Patch of Microstrip Antenna with Gold Plate at Frequency 2400–2450 MHz for Hexagonal Nanosatellite," in *International Conference of Information and Communication Technology*, pp. 322–327, 2013.

[29] C. A. Bergsrud and S. Noghanian, "Microstrip Aperture-Coupled Antenna Design for In-Space Power Reception Experiment Using Nano-Sized Satellite," in *USNC-URSI Radio Science Meeting*, pp. 25–25, 2015.

[30] J. Fouany, M. Thévenot, E. Arnaud, F. Torres, T. Monediere, N. Adnet, R. Manrique, L. Duchesne, J. Baracco, and K. Elis, "Circurlaly Polarized Isoflux Compact X Band Antenna for Nano-satellites Applications," in *European Radar Conference*, pp. 381–384, 2015.

[31] M. P. Magalhaes, M. V. Heckler, J. Mota, A. S. Sombra, and E. C. Moreira, "Design and Analysis of Microstrip Antenna Arrays for Meteorological Nano-Satellites for UHF Uplink," in *International Telecommunications Symposium*, pp. 1–5, 2014.

[32] M. K. Watanabe, R. N. Pang, B. O. Takase, J. M. Akagi, G. S. Shiroma, and W. A. Shiroma, "A 2-D Phase-Detecting/Heterodyne-Scanning Retrodirective Array," *IEEE Transactions on Microwave Theory and Techniques*, vol. 55, no. 12, pp. 2856–2864, 2007.

[33] T. Sreeja, A. Arun, and J. Jaya Kumari, "An S-Band Micro-Strip Patch Array Antenna for Nano-Satellite Applications," in *International Conference on Green Technologies*, pp. 325–328, 2012.

[34] E. Arnieri, L. Boccia, G. Amendola, and G. Di Massa, "A Compact High Gain Antenna for Small Satellite Applications," *IEEE Transactions on Antennas and Propagation*, vol. 55, no. 2, pp. 277–282, 2007.

[35] B. T. Murakami, J. D. Roque, S. S. Sung, G. S. Shiroma, R. Y. Miyamoto, and W. A. Shiroma, “A Quadruple Subharmonic Phase-Conjugating Array for Secure Picosatellite Crosslinks,” in *IEEE MTT-S International Microwave Symposium Digest*, vol. 3, pp. 1687–1690, 2004.

[36] C. Hamrouni, A. Abraham, and A. Alimi, “Both Sides Linked Antenna Array for Ultra Small Satellite Communication Subsystem,” in *International Conference on Innovation Management and Technology Research*, pp. 230–235, 2012.

[37] J. R. Saberin and C. Furse, “Challenges With Optically Transparent Patch Antennas for Small Satellites,” in *IEEE International Symposium on Antennas and Propagation*, pp. 1–4, 2010.

[38] J. Li, S. Gao, and J. Xu, “Circularly Polarized High-gain Printed Antennas for Small Satellite Applications,” in *International Conference on Microwave Technology and Computational Electromagnetics*, pp. 76–79, 2009.

[39] K. F. Warnick, “High Efficiency Phased Array Feed Antennas for Large Radio Telescopes and Small Satellite Communications Terminals,” in *European Conference on Antennas and Propagation*, pp. 448–449, 2013.

[40] F. E. Tubbal, R. Raad, K.-W. Chin, and B. Butters, “S-band Shorted Patch antenna for Inter Pico Satellite Communications,” in *8th International Conference on Telecommunication Systems Services and Applications*, pp. 1–4, 2014.

[41] P. R. Akbar, H. Saito, M. Zang, J. Hirokawa, and M. Ando, “X-band Parallel-Plate Slot Array Antenna for SAR Sensor Onboard 100 kg Small Satellite,” in *IEEE International Symposium on Antennas and Propagation*, pp. 208–209, 2015.

[42] G. Codispoti, M. Lisi, and V. Santachiara, “X-band SAR Active Antenna Design for Small Satellite Applications,” in *IEEE International Symposium on Antennas and Propagation*, vol. 1, pp. 666–669, 1995.

[43] Y. Yao, S. Liao, J. Wang, K. Xue, E. A. Balfour, and Y. Luo, “A New Patch Antenna Designed for CubeSat: Dual feed, L/S dual-band stacked, and circularly polarized,” *IEEE Antennas and Propagation Magazine*, vol. 58, June 2016.

[44] S. Gunaseelan and M. Murugan, “High Gain Patch Antenna for CubeSat,” in *International Conference on Wireless Communications, Signal Processing and Networking (WiSPNET)*, pp. 52–54, March 2016.

[45] M. Aherne, T. Barrett, L. Hoag, E. Teegarden, and R. Ramadas, “Aeneas–Colony I Meets Three-Axis Pointing,” 2011.

[46] A. Babuscia, M. Van de Loo, Q. J. Wei, S. Pan, S. Mohan, and S. Seager, "Inflatable Antenna for CubeSat: Fabrication, Deployment and Results of Experimental Tests," in *IEEE Aerospace Conference*, pp. 1–12, 2014.

[47] N. Chahat, J. Sauder, M. Thomson, R. Hodges, and Y. Rahmat-Samii, "CubeSat Deployable Ka-Band Reflector Antenna for Deep Space missions," in *IEEE International Symposium on Antennas and Propagation & USNC/URSI National Radio Science Meeting*, pp. 2185–2186, 2015.

[48] V. Manohar and Y. Rahmat-Samii, "Characterization of Ka-Band Mesh Surfaces for CubeSat Reflector Antennas: From Simple Wire Grid Model to Complex Knits," in *URSI National Radio Science Meeting*, pp. 1–2, 2016.

[49] R. Barrett, R. Taylor, P. Keller, D. Codell, and L. Adams, "Deployable Reflectors for Small Satellites," in *Annual AIAA/USU Conference on Small Satellites*, 2007.

[50] L. Periasamy and A. J. Gasiewski, "Precision Design, Analysis and Manufacturing of Quasi-Optic Lens/Reflector Antenna Systems for CubeSat MMW/SMMW Radiometers," in *Radio Science Meeting (Joint with AP-S Symposium)*, pp. 265–265, 2015.

[51] M. Takikawa, Y. Inasawa, and Y. Konishi, "One-Dimensional Beam Scanning Reflector Antenna for Small Satellite Applications," in *IEEE-APS Topical Conference on Antennas and Propagation in Wireless Communications*, pp. 159–162, 2012.

[52] E. Peral *et al.*, "RaInCube: A Proposed Constellation of Precipitation Profiling Radars In Cubesat," in *IEEE Symposium on International Geoscience and Remote Sensing*, pp. 1261–1264, 2015.

[53] Y. Rahmat-Samii, "Reflector antennas," in *Antenna handbook* (Y. Lo and S. Lee, eds.), ch. 15, New York: Van nostrand reinhold, 1993.

[54] P. G. Ingerson and W. C. Wong, "The Analysis of Deployable Umbrella Parabolic Reflectors," *IEEE Transactions on Antennas and Propagation,*, vol. 20, no. 4, pp. 409–414, 1972.

[55] F. L. Hai, "The Principle Error and Optimal Feed Point of Umbrella-Like Parabolic Reflector," in *International Symposium on Antennas, Propagation and EM theory (ISAPE)*, pp. 697–700, 2000.

[56] J. Ruze, "Antenna Tolerance Theory - A Review," *Proceedings of the IEEE*, vol. 54, pp. 633–640, April 1966.

[57] Y. Rahmat-Samii, "Effects of Deterministic Surface Distortions on Reflector Antenna Performance," in *Annales des télécommunications*, vol. 40, pp. 350–360, Springer, 1985.

[58] K. Bahadori and Y. Rahmat-Samii, "Characterization of Effects of Periodic and Aperiodic Surface Distortions on Membrane Reflector Antennas," *IEEE Transactions on Antennas and Propagation*, vol. 53, pp. 2782–2791, Sept 2005.

[59] K. Pontoppidan, "Reflector Antennas - An Overview of Surface Distortion Effects," in *Proceedings JINA*, pp. 82–93, 1986.

[60] M. Astrakhan, "Reflecting and Screening Properties of Plane Wire Grids," *Telecommunications and Radio Engineering-USSR*, no. 1, p. 76, 1968.

[61] Y. Rahmat-Samii and S.-W. Lee, "Vector Diffraction Analysis of Reflector Antennas with Mesh Surfaces," *IEEE Transactions on Antennas and Propagation*, vol. 33, pp. 76 – 90, jan 1985.

[62] A. Miura and Y. Rahmat-Samii, "Spaceborne Mesh Reflector Antennas With Complex Weaves: Extended PO/Periodic-MoM Analysis," *IEEE Transactions on Antennas and Propagation*, vol. 55, pp. 1022 –1029, april 2007.

[63] W. A. Imbriale, V. Galindo-Israel, and Y. Rahmat-Samii, "On the Reflectivity of Complex Mesh Surfaces," *IEEE Transactions on Antennas and Propagation*, vol. 39, no. 9, pp. 1352–1365, 1991.

[64] D. Hill and J. Wait, "Analyses of Electromagnetic Scattering from Wire-Mesh Structures," *Electronics Letters*, vol. 12, no. 17, pp. 427–428, 1976.

[65] D. Hill and J. Wait, "Electromagnetic Scattering of an Arbitrary Plane Wave by a Wire Mesh with Bonded Junctions," *Canadian Journal of Physics*, vol. 54, no. 4, pp. 353–361, 1976.

[66] D. Hill and J. Wait, "Electromagnetic Scattering of an Arbitrary Plane Wave by Two Nonintersecting Perpendicular Wire Grids," *Canadian Journal of Physics*, vol. 52, no. 3, pp. 227–237, 1974.

[67] T. Larsen, "A Survey of the Theory of Wire Grids," *IRE Transactions on Microwave Theory and Techniques*, vol. 10, no. 3, pp. 191–201, 1962.

[68] H. Rajagopalan, A. Miura, and Y. Rahmat-Samii, "Equivalent Strip Width for Cylindrical Wire for Mesh Reflector Antennas: Experiments, Waveguide, and Plane-Wave Simulations," *IEEE Transactions on Antennas and Propagation*, vol. 54, no. 10, pp. 2845–2853, 2006.

[69] A. Ludwig, "The Definition of Cross Polarization," *IEEE Transactions on Antennas and Propagation*, vol. 21, pp. 116–119, Jan 1973.

[70] C. A. Balanis, "Antenna Theory: Analysis and Design," 2016.

[71] K. S. Rao and L. Shafai, “Phase Center Calculations of Reflector Antenna Feeds,” *IEEE transactions on antennas and propagation*, vol. 32, pp. 740–742, 1984.

[72] E. I. Muehldorf, “The Phase Center of Horn Antennas,” *IEEE Transactions on Antennas and Propagation*, vol. 18, no. 6, pp. 753–760, 1970.

[73] Y. Hu, “A Method of Determining Phase Centers and its Application to Electromagnetic Horns,” *Journal of the Franklin Institute*, vol. 271, no. 1, pp. 31–39, 1961.